TABLE OF CONTENTS

Page

LIST OF TABLES

Page

LIST OF FIGURES

Page

LIST OF ABREVIATIONS

ALE	Arbitrary Lagrangien-Eulerien
BB	Babuska-Brezzi condition
BDF	Backward Differentiation Formula
CFD	Computational Fluid Dynamics
CSF	Continuum Surface Force method
CFL	Courant-Freidrichs-Lewy number
Dof	Degrees of freedom
FEM	Finite Element Method
FSI	Fluid-Structure Interaction problems
GFEM	Generalized Finite Element Method
GLS	Galerkin/Least-Squares
LEFM	Linear Elastic Fracture Mechanics
LS	Level Set
MLPG	Meshless Local Petrov-Galerkin
QUAD	Quadrangle
RK	Runge-Kutta time integration
PDE	Partial Differential Equation
PUM	Partition of Unity property
SPH	Smoothed Particle Hydrodynamics
SSP	Strong-Stability Preserving
SUPG	Streamline/Upwind Petrov-Galerkin
TRI	Triangle
VMS	Variational Multiscale method
VOF	Volume-of-Fluid method
XFEM	eXtended Finite Element Method

LIST OF SYMBOLS

$\mathrm{abs}(\cdot)$	absolute value function
$A(\cdot)$	area of specified domain
α	interface thickness
β_h	stability coefficient
$\mathbf{C}$	convective matrix
$(\cdot)^{\mathrm{corr}}$	corrected value
δ^{ε}	Dirac delta function
δ_{ij}	Kronecker symbol
$(\cdot)_{\mathrm{D}}$	Direchlet boundary value
γ	surface tension coefficient
∇	continuous gradient operator
$\nabla \cdot$	continuous divergence operator
Γ_{D}	Dirichlet boundary
Γ_{N}	Neumann boundary
Γ_{int}	Interface
$\boldsymbol{\varepsilon}(\mathbf{u})$	rate of deformation tensor
κ	curvature
μ	dynamic viscosity
ν	kinematic viscosity
ρ	density
$\boldsymbol{\sigma}(\mathbf{u}, p)$	Cauchy stress tensor
τ_{L}	stabilization parameter of SUPG term of level set equation
ϕ	level set function
$\boldsymbol{\Omega}$	domain
$\partial\boldsymbol{\Omega}$	domain boundary
$\boldsymbol{\Omega}^{e}$	element domain
e	element
$\lVert \cdot \rVert$	Euclidean norm
$(\cdot)_{ex}$	exact value
Eo	Eötvös number
I	set of all nodes
I^{*}	set of enriched nodes
$(\cdot)^{0}$	initial value
f	right-hand-side vector
f	frequency
$\mathbf{f}_{\mathrm{ST}}$	surface tension force vector
g	magnitude of gravity force vector

$\mathbf{g}$	gravity force vector
H_α	Heaviside function
$\mathbf{G}$	gradient matrix
ψ	global enrichment function
h^e	characteristic element length
$H^1(\Omega)$	Sobolev space of square-integrable functions with square-integrable first derivatives
i	node
$(\cdot)_i$	nodal value
$\mathbf{I}$	identity tensor
$[\![\cdot]\!]$	jump operator
$(\cdot)_k$	identifier for fluid in two-phase flow
$\mathbf{K}$	viscous matrix
$(\cdot)_{\max}$	maximal value
$(\cdot)_{\min}$	minimal value
M	local enrichment function
$\mathbf{M}$	mass matrix
n	number of degrees of freedom
n	number of space dimensions
n^{el}	number of elements
n_s	number of sampling time steps
n_r	level of mesh refinement
$(\cdot)_{\mathrm{num}}$	numerical value
$\mathbf{n}$	outer unit normal vector on domain boundary
$\mathbf{n}_{\mathrm{int}}$	unit normal vector on interface
$n^x_{\mathrm{int}}, n^y_{\mathrm{int}}$	first and second components of the normal unit vector
N	shape function
$\mathbf{N}$	matrix containing shape functions
$\bar{\mathbf{N}}$	matrix containing shape and enrichment functions
$L_2(\Omega)$	Hilbert space of square-integrable functions
p	pressure
P	vector of pressure degrees of freedom
P_i	iso-zero level set position
q	pressure weighting function
r	radius
$(\cdot)_{\mathrm{ref}}$	reference value
$(\cdot)^*$	related to enrichment
Re	Reynolds number
$\mathrm{sign}(\cdot)$	sign function

S	slope
S_p	solution function space for pressure
$S_{\mathbf{u}}$	solution function space for velocity
S_ϕ	solution function space for level set
δ	smaller distance to interface
t	time
T	period
t_{end}	time period
Δt	time-step length
$\mathbf{t}_{\mathrm{int}}$	unit tangential vector on interface
$t_{\mathrm{int}}^x, t_{\mathrm{int}}^y$	first and second components of the tangential unit vector
∂_t	time derivative
$\mathbf{u}$	velocity vector
u	velocity vector along $x-$axis
u_n	normal component of the velocity at the interface
$\mathbf{U}$	vector of velocity degrees of freedom
υ	velocity vector along $y-$axis
$\boldsymbol{v}$	velocity weighting function
v_x	velocity weighting function (for u)
v_y	velocity weighting function (for υ)
$V(\cdot)$	volume of specified domain
V_p	weighting function space for pressure
$V_{\mathbf{u}}$	weighting function space for velocity
V_ϕ	weighting function space for level set
ω_j^i	weights of the $Q-$point Gauss quadrature
$\boldsymbol{w}$	level set weighting function
$\mathbf{x}_{\mathrm{G}}$	center of mass
$x_{\mathrm{G}}, y_{\mathrm{G}}$	first and second coordinate of center of mass
$\mathbf{x}$	coordinate vector
x, y	first (horizontal) and second (vertical) coordinate
$\mathbf{x}_j^i$	points of the $Q-$point Gauss quadrature

INTRODUCTION

Multi-phase flow simulation is an indispensable tool for controlling and predicting physical phenomena in a wide range of engineering and industrial systems, e.g., aerospace, chemical, biomedical, ship hydrodynamics, hydraulic design of dams, nuclear and naval engineering. The main numerical modeling difficulties are due to the jumps in fluid properties (density and viscosity) across the interface, the discontinuities of the flow variables across the interface, the surface tension force that introduces a jump in the pressure field, the changes in the topology of the interface as it evolves with time, and the time and space multi-scales that can exist in the physical phenomena.

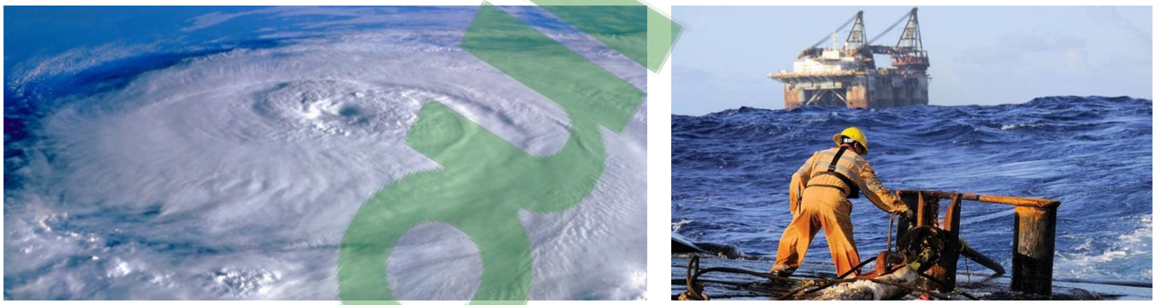

(a) Atmospheric flows (b) Marine engineering

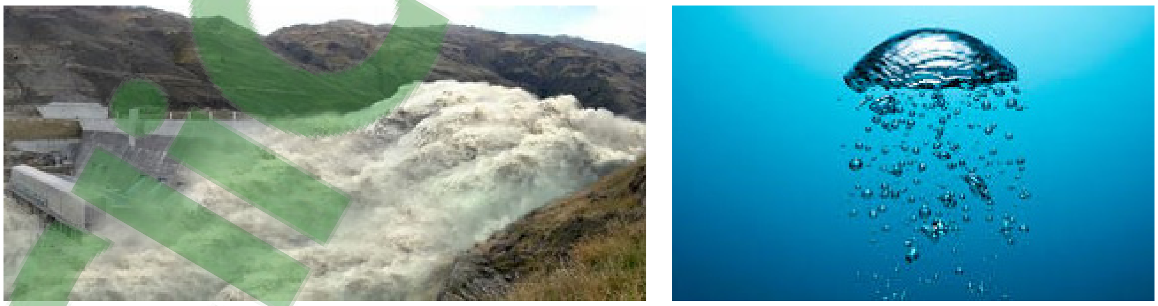

(d) Dam break (c) Rising bubbles

Figure 0.1 Examples of immiscible fluids in industrial and natural processes

In two-fluid flow simulations, it is known that unphysical currents or spurious velocities may occur in fluid regions adjacent to an interface (Ganesan, Matthies et al. 2007; Zahedi, Kronbichler et al. 2012). Their magnitude depends on various factors, such as, the approximation of the pressure jump across the interface, the approximation of the normal vectors to the interface and the curvature required for the calculation of the surface tension force. Spurious velocities may affect the prediction of flow field velocities, or, in more extreme circumstances, can cause the complete break-up of an interface. Therefore, the minimization of such unphysical currents is highly desirable.

Numerous methods have been developed for handling incompressible two-fluid flows. The main difference between them methods is how the interface is represented. All methods can be divided into two general groups:

- interface-tracking methods or moving mesh: front tracking methods (Unverdi and Tryggvason 1992), arbitrary Eulerian-Lagrangian methods (ALE) (Huerta and Liu 1988), boundary integral methods (Best 1993), and deforming space-time finite element formulations (Tezduyar, Behr et al. 1992; Tezduyar, Behr et al. 1992). These methods are accurate for rigid moving boundaries, but the re-meshing procedure can fail when the interface topology is significantly altered; and
- interface-capturing methods or fixed mesh: volume of fluid methods (VOF) (Hirt and Nichols 1981; Pilliod Jr and Puckett 2004), level set methods (Osher and Sethian 1988; Sussman, Smereka et al. 1994; Sethian 1999), and diffuse interface methods (Verschueren, Van De Vosse et al. 2001). These methods are more convenient when large deformations occur at the interface, but they require a higher mesh resolution.

Interface-tracking methods offer an accurate description of the interface and thereby conserve masses (volumes) quite well. In the case of topological changes, which are encountered in immiscible multi-phase flows, these methods are inconvenient and induce significant loss of accuracy, especially when frequent re-meshing is necessary. The challenge associated with the interface-tracking approaches is to address significant topological changes, such as stretching, tearing or merging of configurations. In contrast, the interface-capturing methods are naturally able to account for topological changes of the interface between fluids. This allows for a flexible interface description compared to the interface-tracking methods, but they are often less accurate, e.g., in terms of mass conservation. To increase the accuracy, a mesh refinement is often used close to the interface.

The level set method, introduced by Osher and Sethian (Osher and Sethian 1988), is a popular approach for describing the interface motion in two-phase fluid flows (Sussman, Smereka et al. 1994; Sussman, Fatemi et al. 1998) because it can efficiently handle rapid topological changes as well as the splitting and merging of fluids. Owing to the implicit capture of the interface, some elements may be cut by the interface, and discontinuities therefore occur inside them. Strong and weak discontinuities are encountered. Problems with strong discontinuities present a jump in the solution field, whereas for weak discontinuities, the solution field is continuous and shows a kink, and a jump appears in the derivative of the solution field.

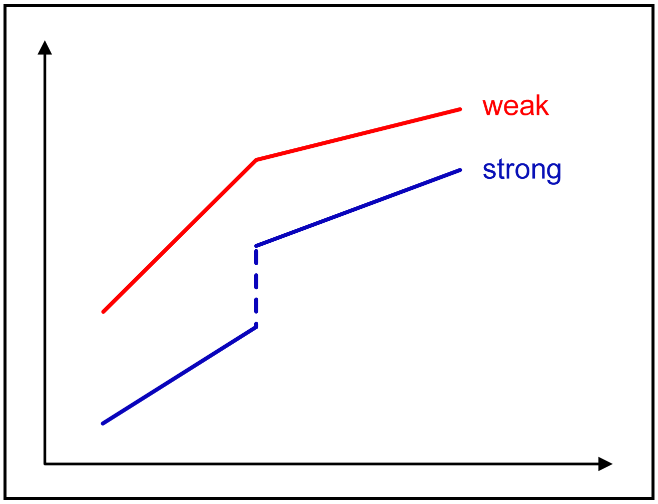

Figure 0.2 Kink and jump discontinuities

Using a standard finite element method (FEM), the jumps and kinks in the pressure and velocity fields across the interface cannot be represented explicitly (Gross and Reusken 2011). To overcome this problem, we can use the diffuse interface method. The viscosity and density can be regularized such that instead of jumping discontinuously, they go smoothly from ρ_1 to ρ_2 (μ_1 to μ_2) over several elements, see Figure 0.3.

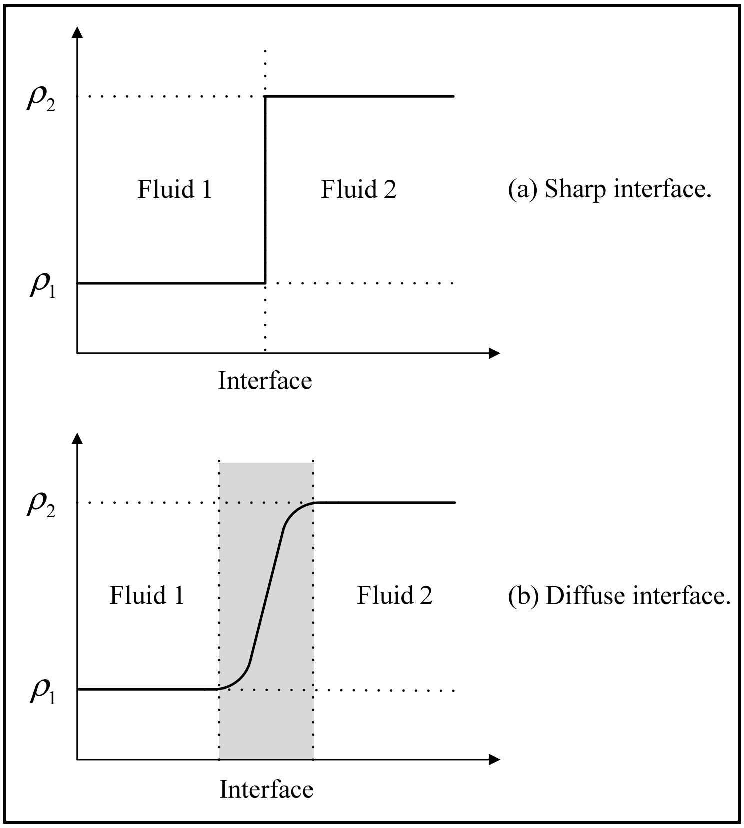

Figure 0.3 Schematic picture of a classical sharp interface and a diffuse interface

However, such approaches may introduce unphysical diffusive effects (Smolianski 2001). The extended finite element method (XFEM) originally developed for crack problems by Belytschko and Black (Belytschko and Black 1999) and redefined by Moës et al. (Moës, Dolbow et al. 1999) addresses these difficulties by enriching the approximation space to represent a known type of discontinuity in the element interiors. XFEM utilizes the partition of unity property (PUM) of the finite element shape functions (Melenk and Babuška 1996). The XFEM popularity is observed because a non-adapted mesh could be used, and the laborious re-meshing procedures are no longer necessary.

Owing to the PUM, strong discontinuities can be accurately reproduced by the sign of the level set function or the jump enrichment (Dolbow, Moës et al. 2000), and the optimal convergence rate can be obtained upon mesh refinement. A weak discontinuity can be incorporated by the absolute value of the level set function (abs-enrichment or kink enrichment); one alternative proposed by Moës et al. (Moës, Cloirec et al. 2003) is the modified abs-enrichment. These enrichments were initially applied to solid mechanics problems.

In two-phase fluid flows, various enrichment schemes for the velocity and/or pressure can be imagined. Chessa and Belytschko (Chessa and Belytschko 2003; Chessa and Belytschko 2003) applied the standard abs-enrichment to account for kinks in the velocity field but did not enrich the pressure field for problems with and without surface tension effects. In addition to the kink enrichment of the velocity field, Minev et al. (Minev, Chen et al. 2003) employed a jump enrichment of the pressure field due to the presence of surface tension effects. In contrast, Groß and Reusken (Groß and Reusken 2007) used Heaviside enrichment to enrich the pressure field for 3D two-phase flows with surface tension effects, but they did not enrich the velocity field. Zlotnik and Díez (Zlotnik and Díez 2009) generalized the modified abs-enrichment (Moës, Cloirec et al. 2003) for $n-$phase flow ($n > 2$), in which different interfaces intersect an element. They enriched the velocity and pressure fields in the case of quasi-static Stokes flow problems. Fries (Fries 2009) used the intrinsic XFEM and performed the enrichment of both the velocity and pressure fields for two-phase flow problems with surface tension effects. Cheng and Fries (Cheng and Fries 2012) developed the h-version of XFEM and used sign enrichment to account for the jump and/or kink in the pressure field in 2D and 3D two-phase incompressible flows. Sauerland and Fries (Sauerland and Fries 2011; Sauerland 2013) suggested the use of sign enrichment to enrich the pressure as a means to represent weak and strong pressure discontinuities, but not for the velocity; they reported that enriching the velocity does not significantly improve the results, and in some cases of unsteady flows, the convergence problems were so severe that no convergence was achieved (Liao and Zhuang 2012). Recently, several XFEM enrichments, following a similar approach to reproduce the internal discontinuities of two-phase flows, were proposed, e.g., by Ausas et al. (Ausas, Buscaglia et al. 2012) and Wu and Li (Wu and Li 2015).

The issue of the discretization of the incompressible Navier-Stokes equations is an important aspect of one-phase and two-phase flow modelling. The approximation spaces of velocity and pressure must satisfy the inf-sup stability condition (LBB) to avoid spurious pressure modes in the numerical solution. There are two strategies for dealing with the LBB condition: (i) satisfying it by choosing an appropriate velocity-pressure element pair, where interpolants of one order lower than those of the velocity are used for the pressure interpolation and (ii) avoiding it by stabilizing the discretized weak formulation. The stabilization enables the use of equal-order interpolation for the pressure and velocity fields. Using numerical experiments, Legrain et al. (Legrain, Moës et al. 2008) analysed the stability of incompressible formulations in elasticity problems enriched with XFEM. They concentrated on the application of XFEM to mixed formulations for problems with fixed interfaces such as the treatment of material inclusions, holes and cracks. In two-phase flows, Groß and Reusken (Groß and Reusken 2007) refine the mesh close to the interface and modify the Taylor-Hood element ($P2/P1$) by enriching the pressure with discontinuous approximations ($P1/P0$ enrichment). They proved the optimal error bounds for the $P1/P0$ approximation, but the inf-sup stability and the order of convergence issue was not investigated numerically or theoretically; it remains an open problem (Esser, Grande et al. 2010). Sauerland and Fries (Sauerland and Fries 2011; Sauerland 2013) numerically investigated different enrichment strategies for two-phase and free-surface flows, utilizing a stabilized Galerkin-Least-Squares (GLS) formulation because the basic interpolations for the velocity and the pressure are of equal order ($Q1/Q1$). However, the stability of these strategies was not shown.

The modeling of the surface tension force presents another difficult task in two-phase flows and remains a challenge for two reasons. The first is that it requires the computation of the normal and surface curvatures of the interface, i.e., first and second derivatives of the level set function. The second difficulty is that the surface tension is applied on the interface, which is not straightforward to realize in the case of an implicit interface representation, i.e., in the context of the level set function, on a surface embedded in the mesh. Yet, one possibility is to convert the surface tension force into a volume force employing the continuum surface force method (CSF) (Brackbill, Kothe et al. 1992). Thereby, the pressure jump is smoothed across a certain distance ε instead of being treated accurately (see Figure 0.4). The focus of this work lies on a sharp interface representation and on the XFEM to capture the discontinuities within elements by enriching the approximation space.

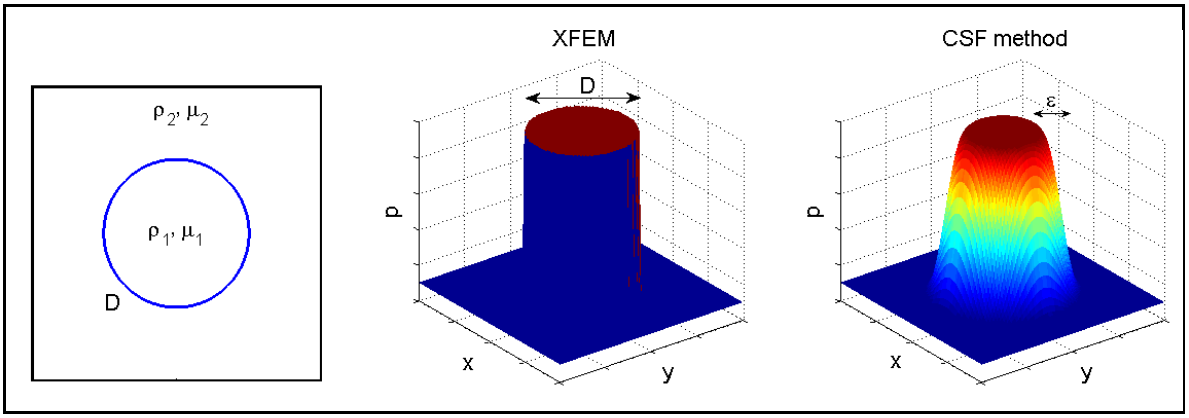

Figure 0.4 Jump in the pressure field

The present research has two objectives. First, we analyze different enrichment schemes of velocity and/or pressure fields, and their accuracy and stability are numerically investigated for test cases involving weak and/or strong discontinuities. We advocate the use of Taylor-Hood mixed interpolations (P2/P1 or Q2/Q1) as the basic element; they have been proven to be robust and more stable even at large Reynolds numbers (Arnold, Brezzi et al. 1984). Second, we present a novel approach for computing the vectors normal to the interface, which are indispensable for the calculation of the curvature and surface tension force. In this approach, a multi-level mesh refinement is first realized inside cut elements, and the points on the interface with a zero level set in each sub-element are then computed; those points are connected with straight segments S_i that are stored. Finally, the vectors normal to the piecewise linear interface are constructed. Thereby, the normal vectors are perfectly perpendicular to the interpolated interface. We analyze the accuracy of the approach, first on a geometric case and then on the complex simulation of the bubble rise problem.

The thesis is divided into six chapters. In the first one, we give an introduction to two-fluid flow modelling together with the motivation for the present study. Chapter 1 introduces the governing Navier-Stokes and the level set transport equations. The equations are accompanied by initial, boundary, and interfacial conditions for the two-fluid interface. Chapter 2 presents the extended finite element method (XFEM) for the spatial discretization. Different enrichment schemes for two-phase flows are discussed. Chapter 3 considers the following aspects: (a) derivation of the weak formulation of the incompressible Navier-Stokes equations and the level-set transport equation, (b) time discretization of the Navier-Stokes equations, (c) strategies for numerical integration, (d) level set updating and reinitialization, and (e) the inf-sup stability issue with XFEM. The following chapter deals with the modelling of surface tension. This is followed by a discussion on the construction of the vectors normal to the interface. Chapter 5 describes in detail the coupling between the Navier-Stokes equations and level set equation with accompanying flowchart. Furthermore, we highlight the time-step size limit. Numerical results for several test cases are presented in Chapter 6. Finally, the thesis is summarized, and the main conclusions and suggestions for future research are presented.

Publications related to this thesis

The results presented in this thesis have led to the following publications in international journals:

Fahsi, A. and A. Soulaimani (Submitted 2016). "Numerical investigations of the XFEM for solving two-phase incompressible flows." International Journal for Numerical Methods in Fluids FLD-16-0243.

Touré, M. K., A. Fahsi, et al. (2016). "Stabilised finite-element methods for solving the level set equation with mass conservation." International Journal of Computational Fluid Dynamics 30(1): 38-55.

Further published material includes contributions to conferences proceedings.

Fahsi, A. and A. Soulaïmani (2011). The extended finite element method for moving interface problems. AÉRO 11, 58th Aeronautics Conference and AGM. Sustainable Aerospace: The Canadian Contribution, Montréal, QC, Canada, Apr. 26-28.

Fahsi, A. and A. Soulaïmani (2013). Velocity-Pressure enrichments for the Taylor-Hood elements for solving moving interface two-phase flows. Annual Meeting of the Canadian Applied and Industrial Mathematics Society CAIMS 2013, Quebec City, QC, Canada, June 16-20.

Soulaïmani, A., A. Fahsi, et al. (2013). A computational approach in XFEM for two-phase incompressible flows. Advances in Computational Mechanics (ACM 2013) - A Conference Celebrating the 70th Birthday of Thomas J.R. Hughes, San Diego, CA, USA, Feb. 24-27.

Soulaïmani, A., A. Fahsi, et al. (2014). Extended velocity-pressure for solving moving interface two-phase flows. 11th World Congres on Computational Mechanics, WCCM XI, Barcelona, Spain, July 20-25.

CHAPTER 1

GOUVERNING EQUATIONS OF TWO-FLUID FLOWS

The governing incompressible Navier-Stokes and the level set transport equations are detailed in this chapter. Those equations are accompanied by initial, boundary, and interfacial conditions. The chapter also describe the possible discontinuities across the interface of the flow variables.

1.1 Incompressible Navier-Stokes equations

The domains occupied by two or more immiscible fluids are denoted by Ω_k, with $\Omega = \cup \Omega_k$ the computational domain and Γ its boundary (cf. Figure 1.1). The interface separating the phases is denoted by Γ_{int}, with the normal vector $\mathbf{n}_{\text{int}}$.

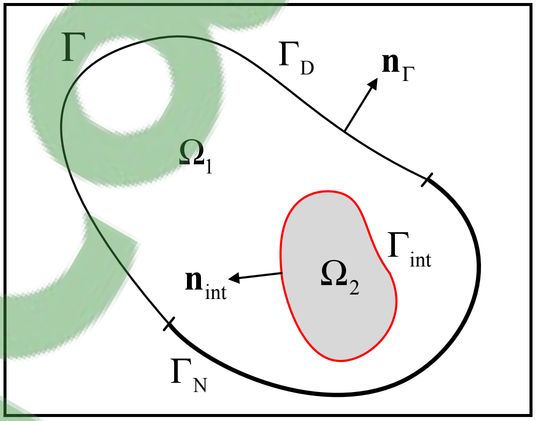

Figure 1.1 Two immiscible fluids Ω_1 and Ω_2 separated by the interface Γ_{int}

The fluid density ρ and viscosity μ are functions of position and time, so that

$$\rho = \rho(\mathbf{x}, t) = \begin{cases} \rho_1 & \text{if } \mathbf{x} \in \Omega_1(t) \\ \rho_2 & \text{if } \mathbf{x} \in \Omega_2(t) \end{cases} \tag{1.1}$$

$$\mu = \mu(\mathbf{x},t) = \begin{cases} \mu_1 & \text{if } \mathbf{x} \in \Omega_1(t) \\ \mu_2 & \text{if } \mathbf{x} \in \Omega_2(t) \end{cases} \tag{1.2}$$

We only consider two-dimensional spatial domains in this thesis. For each phase k, the Navier-Stokes equations governing the incompressible Newtonian flows are written as

$$\rho_k \left(\frac{\partial \mathbf{u}}{\partial t} + \mathbf{u} \cdot \nabla \mathbf{u} \right) = -\nabla p + \nabla \cdot \left(2\mu_k \, \boldsymbol{\varepsilon}(\mathbf{u}) \right) + \rho_k \, \mathbf{g} + \delta(\mathbf{x}, \Gamma_{\text{int}}) \mathbf{f}_{\text{ST}}, \tag{1.3}$$

$$\nabla \cdot \mathbf{u} = 0. \tag{1.4}$$

or in component notation

$$\rho_k \left(\frac{\partial u}{\partial t} + u \frac{\partial u}{\partial x} + \upsilon \frac{\partial u}{\partial y} \right) = -\frac{\partial p}{\partial x} + \frac{\partial}{\partial x}\left[2\mu_k \frac{\partial u}{\partial x} \right] + \frac{\partial}{\partial y}\left[\mu_k \left(\frac{\partial u}{\partial y} + \frac{\partial \upsilon}{\partial x} \right) \right] + \rho_k g_x + \delta(\mathbf{x}, \Gamma_{\text{int}}) f_{x\,\text{ST}}$$

$$\rho_k \left(\frac{\partial \upsilon}{\partial t} + u \frac{\partial \upsilon}{\partial x} + \upsilon \frac{\partial \upsilon}{\partial y} \right) = -\frac{\partial p}{\partial y} + \frac{\partial}{\partial x}\left[\mu_k \left(\frac{\partial u}{\partial y} + \frac{\partial \upsilon}{\partial x} \right) \right] + \frac{\partial}{\partial y}\left[2\mu_k \frac{\partial \upsilon}{\partial y} \right] + \rho_k g_y + \delta(\mathbf{x}, \Gamma_{\text{int}}) f_{y\,\text{ST}}$$

$$\frac{\partial u}{\partial x} + \frac{\partial \upsilon}{\partial y} = 0$$

where (1.3) denotes the momentum equations and (1.4) the continuity equation (incompressibility constraint), $\mathbf{u} = (u, \upsilon)^{\text{T}}$ the fluid velocity vector, t the time, p the dynamic pressure, $\mathbf{g}$ the gravitational acceleration, $\boldsymbol{\varepsilon}(\mathbf{u})$ the rate of deformation tensor

$$\boldsymbol{\varepsilon}(\mathbf{u}) = \tfrac{1}{2}(\nabla \mathbf{u} + (\nabla \mathbf{u})^{\text{T}}) \tag{1.5}$$

and $\mathbf{f}_{\text{ST}}$ the surface tension force which is defined as

$$\mathbf{f}_{\mathrm{ST}}(\mathbf{x}) = \gamma \kappa \mathbf{n}_{\mathrm{int}} \tag{1.6}$$

where γ is the surface tension coefficient in the normal direction, κ is the interfacial curvature, $\delta(\mathbf{x}, \Gamma_{\mathrm{int}})$ is the Dirac delta function, and Γ_{int} is the interface line (surface in 3D).

1.1.1 Boundary, interface and initial conditions

In order to obtain a well-posed problem, boundary conditions have to be imposed on the external boundary Γ and on the interface. The Dirichlet and Neumann boundary conditions are prescribed as

$$\mathbf{u} = \mathbf{u}_{\mathrm{D}}, \quad \forall \mathbf{x} \in \Gamma_{\mathrm{D}} \tag{1.7}$$

$$\boldsymbol{\sigma} \cdot \mathbf{n}_{\Gamma} = \mathbf{h}, \quad \forall \mathbf{x} \in \Gamma_{\mathrm{N}} \tag{1.8}$$

where Γ_{D} denotes the Dirichlet boundary, Γ_{N} the Neumann boundary, $\mathbf{u}_{\mathrm{D}}$ and $\mathbf{h}$ the specified velocity and stress, respectively, $\boldsymbol{\sigma}(\mathbf{u}, p) = -p\,\mathbf{I} + 2\mu_k\, \boldsymbol{\varepsilon}(\mathbf{u})$ the Cauchy stress tensor, $\mathbf{n}_{\Gamma}$ the outward pointing normal vector on the boundary Γ, and $\mathbf{I}$ the identity tensor.

The interfacial equilibrium conditions, which couple the stress and velocity between the two phases at the interface, are given by

$$[\![\mathbf{u}]\!] = \mathbf{u}\big|_{\Omega_1} - \mathbf{u}\big|_{\Omega_2} = 0, \quad \forall \mathbf{x} \in \Gamma_{\mathrm{int}}, t \in [0, t_{\mathrm{end}}] \tag{1.9}$$

$$[\![\boldsymbol{\sigma} \cdot \mathbf{n}_{\mathrm{int}}]\!] = \gamma \kappa \mathbf{n}_{\mathrm{int}}, \quad \forall \mathbf{x} \in \Gamma_{\mathrm{int}}, t \in [0, t_{\mathrm{end}}] \tag{1.10}$$

where the operator $\llbracket \bullet \rrbracket$ represents the jump across the interface Γ_{int}. It can be seen from the equilibrium condition of the interfacial force (1.10) that the total stress generated by two-phase flow is balanced with the surface tension.

Initial conditions complement the problem as indicated:

$$\mathbf{u}(\mathbf{x},0)=\mathbf{u}^{0}(\mathbf{x}),\quad \forall\mathbf{x}\in\Omega \text{ at } t=0 \tag{1.11}$$

Inserting the definitions for stress and strain tensors into the interface condition for the normal stress (1.10) results in

$$\left\llbracket -p\mathbf{I}+\mu\left(\nabla\mathbf{u}+(\nabla\mathbf{u})^{\mathrm{T}}\right)\right\rrbracket\cdot\mathbf{n}_{\text{int}}=\gamma\kappa\mathbf{n}_{\text{int}},\quad \forall\mathbf{x}\in\Gamma_{\text{int}},t\in\left[0,t_{\text{end}}\right] \tag{1.12}$$

It is clear that the presence of the viscosity jump or/and the surface tension at the interface leads to a jump in the pressure field and a jump in the velocity gradient across the interface. In the hydrostatic case ($\mathbf{u}=\mathbf{0}$) and without surface tension ($\gamma=0$), the momentum equation in (1.3) reduces to

$$\nabla p=\rho_{k}\,\mathbf{g}\,,\quad \forall\mathbf{x}\in\Omega_{k},t\in\left[0,t_{\text{end}}\right] \tag{1.13}$$

Along the interface, Eq. (1.13) can be written as

$$\llbracket\nabla p\rrbracket=\llbracket\rho\rrbracket\mathbf{g},\quad \forall\mathbf{x}\in\Gamma_{\text{int}},t\in\left[0,t_{\text{end}}\right] \tag{1.14}$$

We note that the gravitational forces in combination with a jump in the density lead to a jump in the pressure gradient.

In the numerical simulation of incompressible immiscible two-phase flows, we need to account for

- a jump in the gradient velocity (or kink in the velocity) across the interface where viscosity jumps exist (cf. Figure 1.2a);
- a jump in the pressure where viscosity jumps or/and surface tension exist (cf. Figure 1.2a and Figure 1.2c); and
- a jump in the gradient pressure (or kink in the pressure) where density jumps exist (cf. Figure 1.2b).

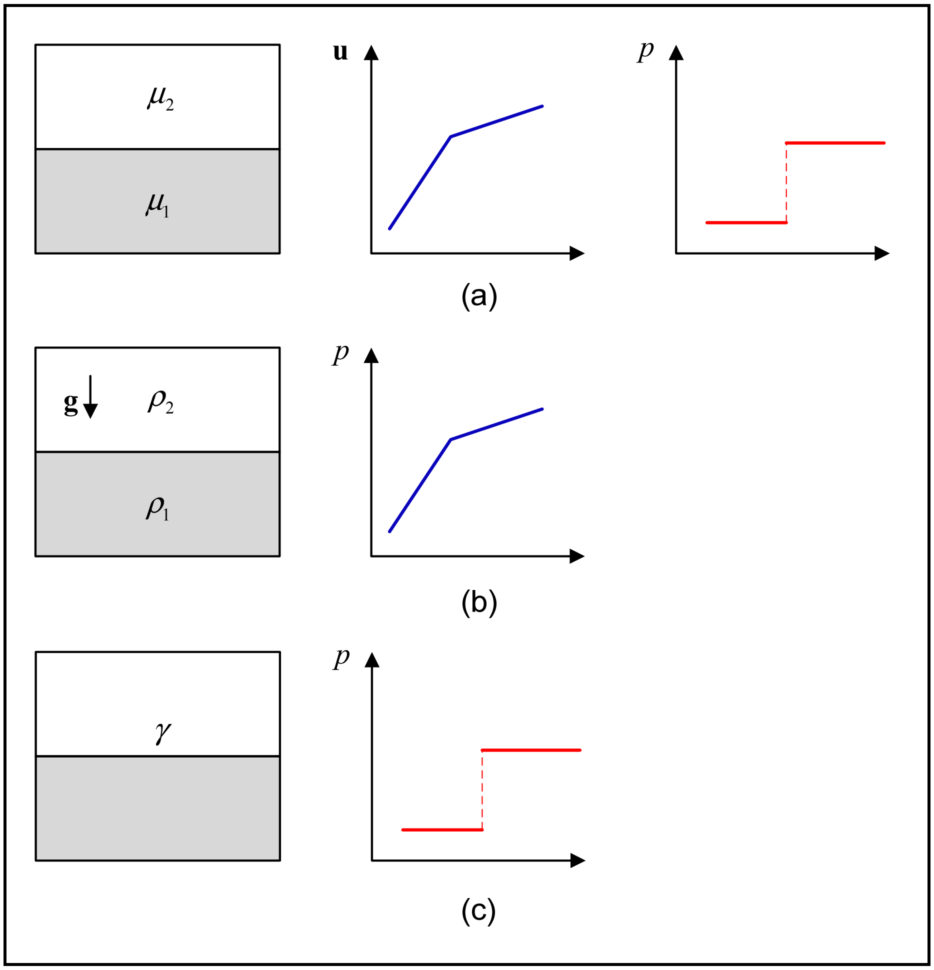

Figure 1.2 Two-phase flow discontinuities: (a) viscosity jump, (b) density jump, and (c) surface tension

1.2 Interface description for two-phase fluid flows

In this section, we introduce the level set method as a method for the implicit representation of interfaces. The level set method (Osher and Sethian 1988) is a numerical technique originally developed to analyze and follow the motions and deformations of an interface under an arbitrary velocity field. This velocity can depend: on the position of the interface, on time, on a related underlying physical problem, on a geometrical property of the interface or on any other parameters. Osher and Sethian proposed to introduce a smooth scalar function $\phi(\mathbf{x})$ defined on all $\mathbf{x} \in \mathbb{R}^{n}$ which, at all times, should represent an interface Γ_{int} of dimension $\text{n}-1$ as the set where $\phi(\mathbf{x})=0$.

Up to now, this method has been successfully applied to numerous physical problems: multi-phase fluid flows (Sussman, Smereka et al. 1994), crack propagation (Strouboulis, Babuška et al. 2000), computer vision and shape recognition (Kass, Witkin et al. 1988), fire propagation simulation (Karypis and Kumar 1998), image processing (Karihaloo and Xiao 2003) and even in movie special effect. Moreover, as we will see later, the level set description/method fits naturally with the extended finite element method (XFEM) (see section 3.4).

1.2.1 Description of the level set

A level set function ϕ is defined on the overall domain Ω to indicate the interface Γ_{int}. It is initialized for every point $\mathbf{x}$ as a signed distance to the given interface at the initial time:

$$\phi(\mathbf{x}, t=0)=\phi^{0}(\mathbf{x})=\min_{\mathbf{x}^{*}\in\Gamma_{\text{int}}}\left(-\text{sign}\left((\mathbf{x}-\mathbf{x}^{*})\cdot\mathbf{n}_{\text{int}}\right)\left\|\mathbf{x}-\mathbf{x}^{*}\right\|\right), \quad \forall\mathbf{x}\in\Omega \tag{1.15}$$

With this definition, the level set function verifies the Eikonal property

$$\left\|\nabla\phi^{0}(\mathbf{x})\right\|=1 \tag{1.16}$$

Each phase subdomain is then identified according to the sign of the level set function:

$$\phi(\mathbf{x},t)\begin{cases} <0, & \forall\,\mathbf{x}\in\Omega_1, \\ =0, & \forall\,\mathbf{x}\in\Gamma_{\text{int}}, \\ >0, & \forall\,\mathbf{x}\in\Omega_2. \end{cases} \tag{1.17}$$

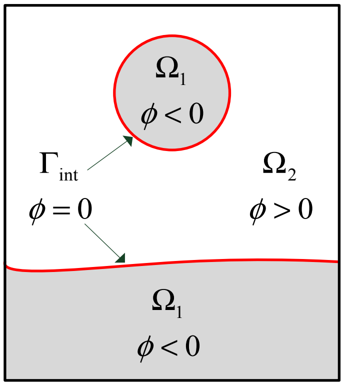

Figure 1.3 Definition of level set function

As an example, we define Γ_{int} as a circle centered at the origin with radius $r=0.50$. We define $\phi(\mathbf{x})$ to be the signed distance function, with a positive sign inside the circle. We have

$$\phi(\mathbf{x})=r-\sqrt{x^2+y^2} \tag{1.18}$$

This $\phi(\mathbf{x})$ is shown in Figure 1.4.

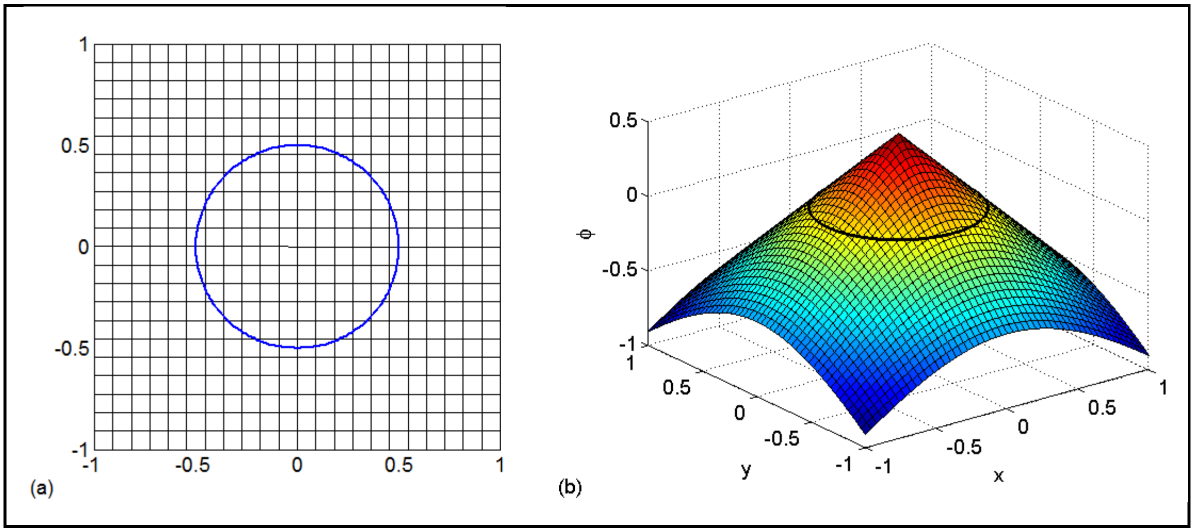

Figure 1.4 (a) A circular interface in 2D (b) represented by the signed distance function ϕ.

Because the interface Γ_{int} is moving during the simulation, $\phi(\mathbf{x}, t)$ is governed by the pure transport equation

$$\begin{aligned} &\frac{\partial \phi}{\partial t} + \mathbf{u} \cdot \nabla \phi = 0 && \forall \mathbf{x} \in \Omega, t \in [0, t_{\text{end}}] \\ &\phi(\mathbf{x}, 0) = \phi^0 && \forall \mathbf{x} \in \Omega \text{ at } t = 0 \end{aligned} \tag{1.19}$$

where $\mathbf{u}(\mathbf{x}, t)$ is the convective fluid velocity, which is the solution of the Navier-Stokes Eq. (1.3) and (1.4).

If the level set is smooth enough, the normal and curvature fields can be computed as

$$\mathbf{n}_{\text{int}}(\mathbf{x}, t) = \frac{\nabla \phi(\mathbf{x}, t)}{\| \nabla \phi(\mathbf{x}, t) \|}, \quad \mathbf{x} \in \Gamma_{\text{int}} \tag{1.20}$$

and

$$\kappa(\mathbf{x},t) = -\nabla\cdot\mathbf{n}_{\text{int}}(\mathbf{x},t) = -\frac{\phi_y^2\phi_{xx}+\phi_x^2\phi_{yy}-2\phi_x\phi_y\phi_{xy}}{(\phi_x^2+\phi_y^2+\varepsilon)^{3/2}}, \qquad \mathbf{x}\in\Gamma_{\text{int}} \tag{1.21}$$

here, e.g. ϕ_x denotes the first derivative of ϕ in x-direction and $\varepsilon = 10^{-7}$. Note that the unit normal vector $\mathbf{n}_{\text{int}}$ always points to the domain where $\phi > 0$.

An accurate approximation of both the normal and the curvature is a crucial ingredient for the precise modeling of the surface tension force. However, the level set function evolution may develop discontinuities in its derivatives near regions of strong topological changes, making the curvature discretization difficult. To improve the results, one can resort to higher-order space approximations (Cheng and Fries 2012). Conversely, if an explicit time integration method is used, the surface tension term induces a strong stability constraint on the time step.

1.3 Closure

In this chapter, we have presented the governing equations essential to solve two-phase incompressible flow. The Navier-Stokes equations, the main physical phenomena that occur at the interface between fluids, the boundary and initial conditions, and the interfacial conditions are first given in Section 1.1. The interfacial conditions reveal that:

- the jumps of fluid viscosity and density need to be accurately taken into account in order to satisfy the interfacial equilibrium; and
- the surface tension force plays an important role in the two-phase flows. This force needs to be accurately computed.

The description of the interface is realized implicitly by the level set function. In order to account for the interface motion a standard advection equation is solved using the fluid velocity.

CHAPTER 2

THE EXTENDED FINITE ELEMENT METHOD (XFEM)

The extended finite element method (XFEM) is a numerical technique for solving arbitrary discontinuities in finite element method (FEM), based on the generalized finite element method (GFEM) and the partition of unity method (PUM). It extends the classical FEM approach by enriching the solution space with discontinuous functions. This is accomplished in local regions of the computational domain which contain discontinuities. In this chapter, an introduction and a brief literature review of the XFEM are first given. This is then followed by a description of the XFEM approximation with enrichments for both weak and strong discontinuities.

2.1 A literature review of the XFEM

In the previous chapter, it has been shown that the presence of surface tension force and/or a jump in viscosity at the interface leads to a jump in the gradient of the velocity and a jump in the pressure at the interface. A kink in the pressure also occurs owing to the jump in density. The question remains how these discontinuities across the interface can be incorporated into the discretization.

The standard FEM is unable to model discontinuities in the solution on element interiors because the shape functions are generally at least C^1 on the element and C^0 between elements. To accurately resolve this class of problems, the discontinuity position has to coincide with the FEM mesh (i.e. interface tracking). If the problem involves evolving discontinuities, this approach can become arduous and re-meshing process may become necessary. This can also introduce errors, since all the existing nodes must be mapped onto a new and different set of nodes.

Therefore, much attention has been devoted to the development of the so-called Mesh Free methods that overcome the difficulties related to the mesh. Mesh Free methods are a response to the limitations of FEM, these methods use a set of nodes scattered within the problem domain as well as sets of nodes scattered on the boundaries of the domain to represent (not discretize) the problem domain and its boundaries. One of the earliest Mesh Free methods is smoothed particle hydrodynamics (SPH), introduced by Gingold and Monaghan in an astrophysical context (Gingold and Monaghan 1977). Later, the SPH method has been extended to deal with free surface incompressible flows; applications include the splashing of breaking waves and the dam breaking problem (Monaghan 1994). SPH method has many advantages in computation, e.g. simple in concept, easy to implement, suitable for large deformations of the interface, meshfree, etc. However, SPH method has sevral main technical drawbacks, e.g. difficulty in enforcing essential boundary conditions and the numerical algorithm suffers from strong instability. Over the ensuing decades, various new Mesh Free methods have been developed, aimed at improving the performance and eliminating pathologies in numerical computations, we can mention the Element Free Galerkin (EFG) proposed by Belytschko et al (Belytschko, Lu et al. 1994) and meshless local petrov-Galerkin (MLPG) (Atluri and Shen 2002). While Mesh Free methods have been applied successfully to a wide range of applications, they suffer from some difficulties:

- they are often unstable and less accurate, especially for problems governed by PDEs (Partial Differential Problems) with derivative boundary conditions;
- the computational cost is higher than FEM;
- the shape functions are not polynomial and require high-order integration schemes.

In 1996, Melenk and Babuška (Melenk and Babuška 1996) developed the mathematical background of the partition of unity method (PUM), namely that the sum of the shape functions must be unity. They showed that the classical FE basis can be extended to represent a specific given function on the computational domain and that some advantages found in the Mesh Free methods can be realized using PUM. The basic idea of PUM is to enrich or to extend the finite element approximation by adding special shape functions, typically non-polynomial, to capture desired features in the solution. This notion of enriching the finite element approximation is not new (Benzley 1974; Schönheinz 1975). In (Melenk and Babuška 1996; Babuška and Melenk 1997), the additional functions are added globally to the finite element approximation. This method did not get a lot of success due to the fact that the enrichment is global, the resulting stiffness matrix is symmetric and banded, and its sparsity is not significantly compromised.

Another instance of the PUM is the generalized finite element method (GFEM), Strouboulis et al. (Strouboulis, Copps et al. 2001) use GFEM for solving different elliptic problems by enriching the entire domain. The enrichment technique improves the solution by introducing additional shape functions but the second advantage of this method is that discontinuous shape functions can be added allowing to represent non-smooth behavior independently of the mesh. Later, as the jumps, kinks, and singularities in the solution are generally local phenomena, they adopted the local or minimal enrichment by restricting the enrichment only to a subset of the domain.

Belytschko and Black (Belytschko and Black 1999) adopted the PUM to model crack growth, by locally enriching the conventional finite element (FE) approximation with the exact near tip crack fields. A main feature of this work was the adding of discontinuous enrichment functions, and the use of a mapping technique to model arbitrary discontinuities. Unfortunately, the mapping procedure is difficult for long discontinuities. As a result, some level of re-meshing technique is implemented as the crack propagates.

Later Dolbow et al. (Dolbow and Belytschko 1999; Dolbow, Moës et al. 2000) and Moes et al. (Moës, Dolbow et al. 1999) improved the method and called it the extended finite element method (XFEM) by adding a magnificent procedure called enrichment that contains a Heaviside function and the asymptotic near tip field. One of the differences with GFEM method was that, any kind of generic function can be incorporated in XFEM to construct the enriched basis function, however the current form of GFEM has no such differences with XFEM: «*The XFEM and GFEM are basically identical methods: the name generalized finite element method was adopted by the Texas school in 1995–1996 and the name extended finite element method was coined by the Northwestern school in 1999.*» (Belytschko, Gracie et al.

2009). Following these pioneering works, the X-FEM approach has rapidly attracted a lot of interest and has been the topic of intensive researches and applications.

2.1.1 Coupling XFEM with the level set

A significant advancement of the XFEM was given by its coupling with the level set method. The level set method complements the XFEM extremely well as it provides the information on where and how to enrich. Stolarska et al. (Stolarska, Chopp et al. 2001) presented the first implementation of level set method for modeling of crack propagation within the XFEM framework where the interface evolution was successfully performed by the level set method. Later, Moës et al. (Moës, Gravouil et al. 2002) and Gravouil et al. (Gravouil, Moës et al. 2002) performed a combined XFEM and the level set method to construct arbitrary discontinuities in 3D analysis of crack problems. Beside providing a theoretical method to update the position of the interface, the use of the level set method offered complementary capabilities such as simplifying the selection of the nodes to be enriched and defining the discontinuous enrichment functions.

2.1.2 Applications

Over the years, the XFEM-community continually grew and the method developed quickly. It has been incorporated into the general purpose codes such as ABAQUS and LS-DYNA. By now, advances in the XFEM have led to applications in various fields of computational mechanics and physics.

- linear elastic fracture mechanics (LEFM);
- cohesive fracture mechanics;
- composite materials and material inhomogeneities;
- plasticity, damage, and fatigue problems;
- two-phase flows;
- fluid–structure interaction;
- fluid flow in fractured porous media;

- solidification problems;
- thermal and thermo-mechanical problems;
- contact problems;
- topology optimization;
- piezoelectric and magneto-electroelastic problems.

2.2 The XFEM formulation

In the XFEM, the standard finite element method is extended by incorporating an enrichment function $\psi(\mathbf{x},t)$, chosen judiciously, to reproduce the desired discontinuity inside the cut element. This is achieved via a partition of the unity (PUM) property (Melenk and Babuška 1996). Applied to the velocity field, an enriched velocity approximation can be defined as

$$\begin{aligned}\mathbf{u}(\mathbf{x},t) &= \sum_{i\in I} N_i^{\mathbf{u}}(\mathbf{x})\mathbf{u}_i + \sum_{i\in I^*} M_i^{\mathbf{u}}(\mathbf{x},t)\mathbf{u}_i^* \\ &= \underbrace{\sum_{i\in I} N_i^{\mathbf{u}}(\mathbf{x})\mathbf{u}_i}_{\mathbf{u}^{\mathrm{FE}}} + \underbrace{\sum_{i\in I^*} N_i^{\mathbf{u}*}(\mathbf{x})\cdot\left[\,\psi^{\mathbf{u}}(\mathbf{x},t)-\psi^{\mathbf{u}}(\mathbf{x}_i,t)\,\right]\mathbf{u}_i^*}_{\mathbf{u}^{\mathrm{Enr}}}\end{aligned} \tag{2.1}$$

where $N_i^{\mathbf{u}}(\mathbf{x})$ is the standard FEM shape function for node i, $M_i^{\mathbf{u}}(\mathbf{x},t)$ is the local enrichment function, $\mathbf{u}_i$ are the nodal variable values, $\mathbf{u}_i^*$ are the additional XFEM unknowns, I is the set of all nodes in the domain Ω, I^* is the set of enriched nodes (the nodes of elements cut by the interface), $N_i^{\mathbf{u}*}(\mathbf{x})$ is the partition of unity function for node i, and $\psi(\mathbf{x},t)$ is the global enrichment function.

An enriched approximation for the pressure field is defined as

$$p(\mathbf{x},t) = \sum_{i\in I} N_i^{p}(\mathbf{x})p_i + \sum_{i\in I^*} N_i^{p*}(\mathbf{x})\cdot\left[\,\psi^{p}(\mathbf{x},t)-\psi^{p}(\mathbf{x}_i,t)\,\right]p_i^* \tag{2.2}$$

The first term in (2.1) is the standard finite element approximation while the second term is called the enrichment. It is obvious that the property $N_i(\mathbf{x}_i) = \delta_{ij}$ ($\delta_{ij} = 1$ if $i = j$) does not necessarily guarantee that $\mathbf{u}(\mathbf{x}_i) = \mathbf{u}_i$. Specifically, if the enrichment term does not vanish at the enriched node $i \in I^*$ it follows that $\mathbf{u}(\mathbf{x}_i) \neq \mathbf{u}_i$.

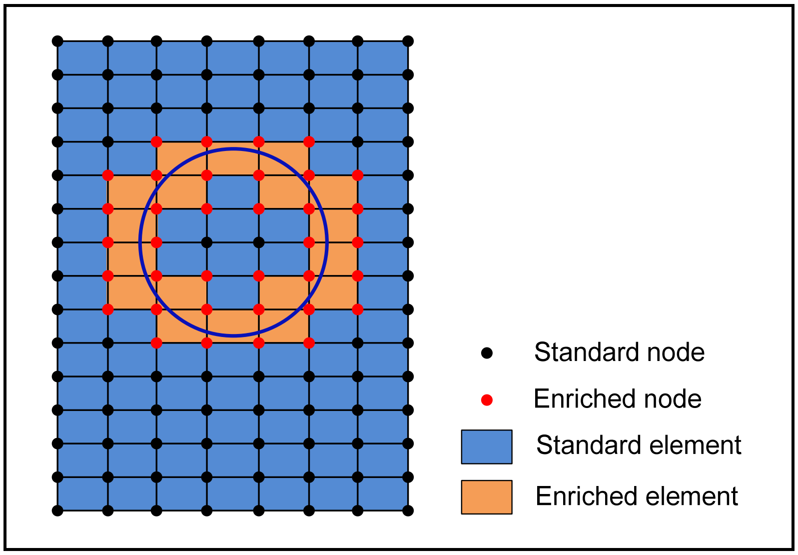

Figure 2.1 Domain with a circular interface illustrating
the set of enriched nodes and the enriched elements

A necessary condition to ensure the convergence is that the functions $N_i(\mathbf{x})$ and $N_i^*(\mathbf{x})$ build a partition of unity over the domain, i.e.,

$$\begin{aligned} &\sum_{i\in I} N_i(\mathbf{x}) = 1; \\ &\sum_{i\in I^*} N_i^*(\mathbf{x}) = 1. \end{aligned} \tag{2.3}$$

In the context of XFEM, the functions $N_i(\mathbf{x})$ and $N_i^*(\mathbf{x})$ are chosen to be the classical shape functions. However, the functions $N_i^{\mathbf{u}*}(\mathbf{x})$ can be linear or quadratic shape functions. The order is sometimes chosen differently for $N_i^{\mathbf{u}}(\mathbf{x})$ and $N_i^{\mathbf{u}*}(\mathbf{x})$. The functions $N_i^{p*}(\mathbf{x})$ are linear.

Figure 2.1 illustrates which nodes are enriched for a circular interface in a discretized domain. It is observed that all nodes are enriched which belong to elements intersected by the interface.

2.2.1 Modeling strong discontinuities

As we have mentioned in the previous paragraph, any generic function representing the behavior of the approximating field across the interface can be easily incorporated into the approximation space. Strong discontinuity shows a jump in the field (cf. Figure 0.2), hence in such cases enriching the approximation space with a sign-enrichment function or a Heaviside-enrichment function are reasonable choices.

$$\psi_{\text{sign}}(\mathbf{x},t) = \operatorname{sign}\left(\phi(\mathbf{x},t)\right) = \begin{cases} -1 & \text{if } \phi(\mathbf{x},t) < 0 \\ 0 & \text{if } \phi(\mathbf{x},t) = 0 \\ +1 & \text{if } \phi(\mathbf{x},t) > 0 \end{cases} \tag{2.4}$$

$$\psi_{\text{H}}(\mathbf{x},t) = \text{H}\left(\phi(\mathbf{x},t)\right) = \begin{cases} 0 & \text{if } \phi(\mathbf{x},t) \le 0 \\ 1 & \text{if } \phi(\mathbf{x},t) > 0 \end{cases} \tag{2.5}$$

The resulting enriched basis functions formed by multiplication of the partition of unity shape functions and the enrichment functions contain a jump at the interface and thus gives a better approximation to the field variable.

Let us consider a body with domain Ω. The domain is discretized into 3 elements Ω_1, Ω_2 and Ω_3. Let there be a discontinuity in element 2, such that it incorporates a strong discontinuity at $\mathbf{x} = \mathbf{x}^*$ in the field variable (cf. Figure 2.2).

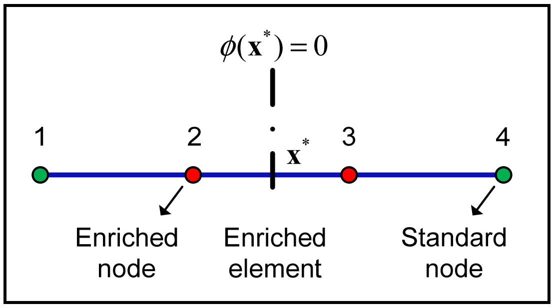

Figure 2.2 Problem statement

Let $N_2(\mathbf{x})$ and $N_3(\mathbf{x})$ are the classical linear finite element shape functions associated with nodes 2 and 3 respectively, which also satisfy the PUM.

The XFEM approximation to the field variable u, reads as

$$\begin{aligned} u(\mathbf{x}) &= \sum_{i\in I} N_i(\mathbf{x})u_i + \sum_{i\in I^*} N_i^*(\mathbf{x})\cdot\left[\psi_{\text{sign}}(\mathbf{x})-\psi_{\text{sign}}(\mathbf{x}_i)\right]u_i^* \\ &= \sum_{i\in I} N_i(\mathbf{x})u_i + \sum_{i\in I^*} N_i(\mathbf{x})\cdot\left[\psi_{\text{sign}}(\mathbf{x})-\psi_{\text{sign}}(\mathbf{x}_i)\right]u_i^* \end{aligned} \tag{2.6}$$

where $N^*(\mathbf{x})=N(\mathbf{x})$. It can be noticed from the Figure 2.3, that the enriched basis function thus formed by the multiplication of the shape functions and the enrichment function, contains a jump at $\mathbf{x}=\mathbf{x}^*$ required to approximate the behavior of u.

The jump at the interface can be written as

$$
\begin{aligned}
\llbracket u \rrbracket = \;& u^{+} - u^{-} \\
= \;& \sum_{i \in I} N_i(\mathbf{x}^{*+}) u_i + \sum_{i \in I^*} N_i(\mathbf{x}^{*+}) \cdot \left[\psi_{\text{sign}}(\mathbf{x}^{*+}) - \psi_{\text{sign}}(\mathbf{x}_i) \right] u_i^* \\
& - \sum_{i \in I} N_i(\mathbf{x}^{*-}) u_i - \sum_{i \in I^*} N_i(\mathbf{x}^{*-}) \cdot \left[\psi_{\text{sign}}(\mathbf{x}^{*-}) - \psi_{\text{sign}}(\mathbf{x}_i) \right] u_i^* \\
= \;& \sum_{i \in I^*} N_i(\mathbf{x}^{*+}) \cdot \left[\psi_{\text{sign}}(\mathbf{x}^{*+}) - \psi_{\text{sign}}(\mathbf{x}_i) \right] u_i^* - \sum_{i \in I^*} N_i(\mathbf{x}^{*-}) \cdot \left[\psi_{\text{sign}}(\mathbf{x}^{*-}) - \psi_{\text{sign}}(\mathbf{x}_i) \right] u_i^* \\
= \;& 2N_2(\mathbf{x}^{*+}) u_2^* + 2N_3(\mathbf{x}^{*-}) u_3^* \\
= \;& 2 \sum_{i \in I^*} N_i(\mathbf{x}^*) u_i^*
\end{aligned}
$$

where u^{+} and $u-$ are the values of the variable u just at the left and just at the right of the interface Γ_{int}.

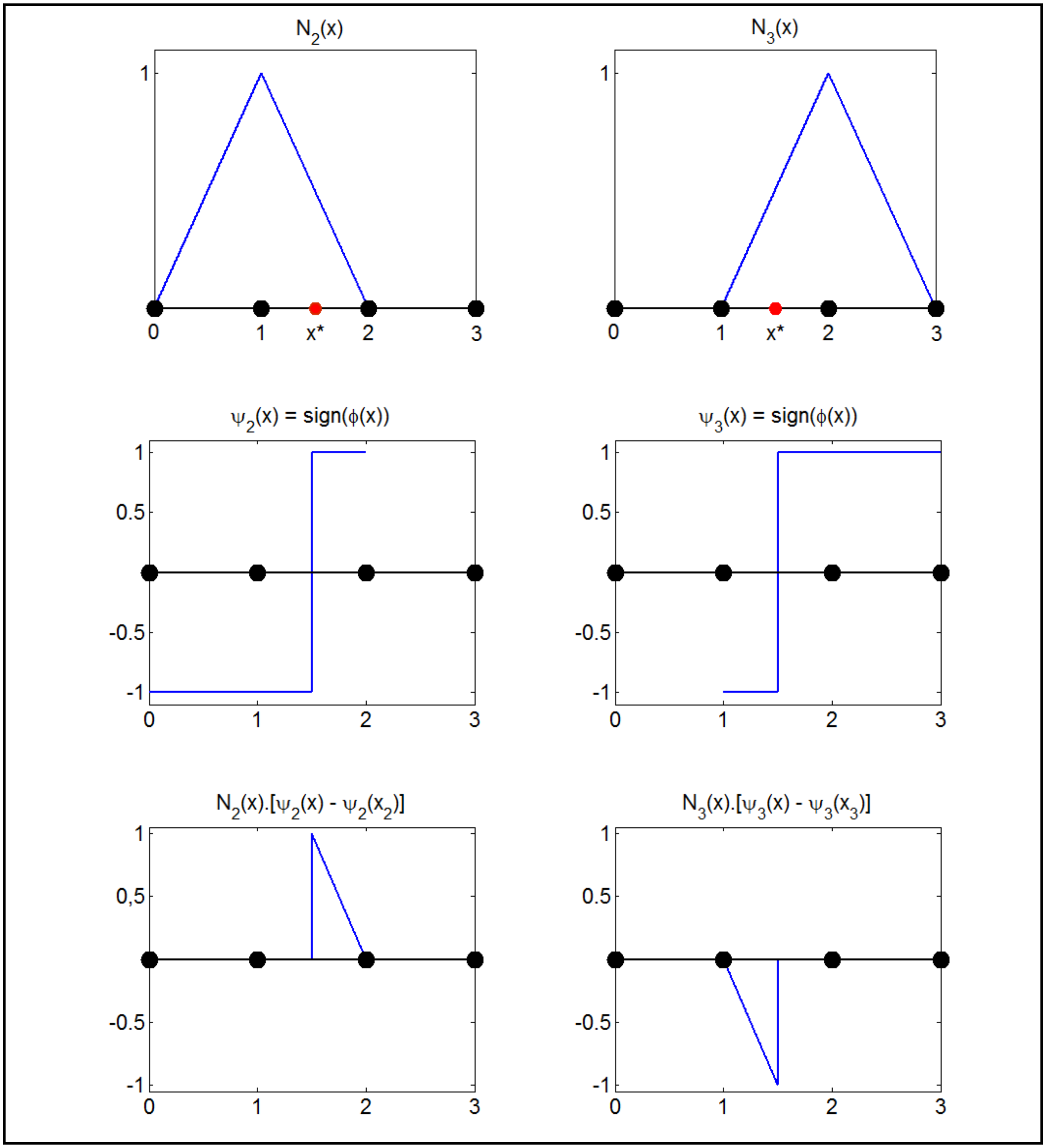

Figure 2.3 Enriched basis function for a strong discontinuity in 1D

2.2.2 Modeling weak discontinuities

A weak discontinuity shows a kink at the interface and has discontinuous derivative. For modeling fields having discontinuous derivatives usually an abs-enrichment is used.

$$\psi_{\text{abs}}(\mathbf{x},t)=\text{abs}\left(\phi(\mathbf{x},t)\right)=\left|\,\phi(\mathbf{x},t)\right| \tag{2.7}$$

It can be observed from the Figure 2.4, that the enriched basis function thus formed by the multiplication of the shape functions and the enrichment function, contains a kink at $\mathbf{x}=\mathbf{x}^*$.

In our 1D we can define $\psi_{\text{abs}}(\mathbf{x})$ as:

$$\psi_{\text{abs}}(\mathbf{x})=\left|\mathbf{x}-\mathbf{x}^*\right| \tag{2.8}$$

Illustrated in Figure 2.4. The XFEM approximation then reads:

$$u(\mathbf{x})=\sum_{i\in I}N_i(\mathbf{x})u_i+\sum_{i\in I^*}N_i(\mathbf{x})\cdot\left[\psi_{\text{abs}}(\mathbf{x})-\psi_{\text{abs}}(\mathbf{x}_i)\,\right]u_i^* \tag{2.9}$$

$$\begin{aligned}\nabla u(\mathbf{x})&=\sum_{i\in I}\nabla N_i(\mathbf{x})u_i\\&\quad+\sum_{i\in I^*}\Big(\nabla N_i(\mathbf{x})\cdot\left[\psi_{\text{abs}}(\mathbf{x})-\psi_{\text{abs}}(\mathbf{x}_i)\,\right]+N_i(\mathbf{x})\cdot\psi_{\text{sign}}(\mathbf{x})\Big)u_i^*\end{aligned} \tag{2.10}$$

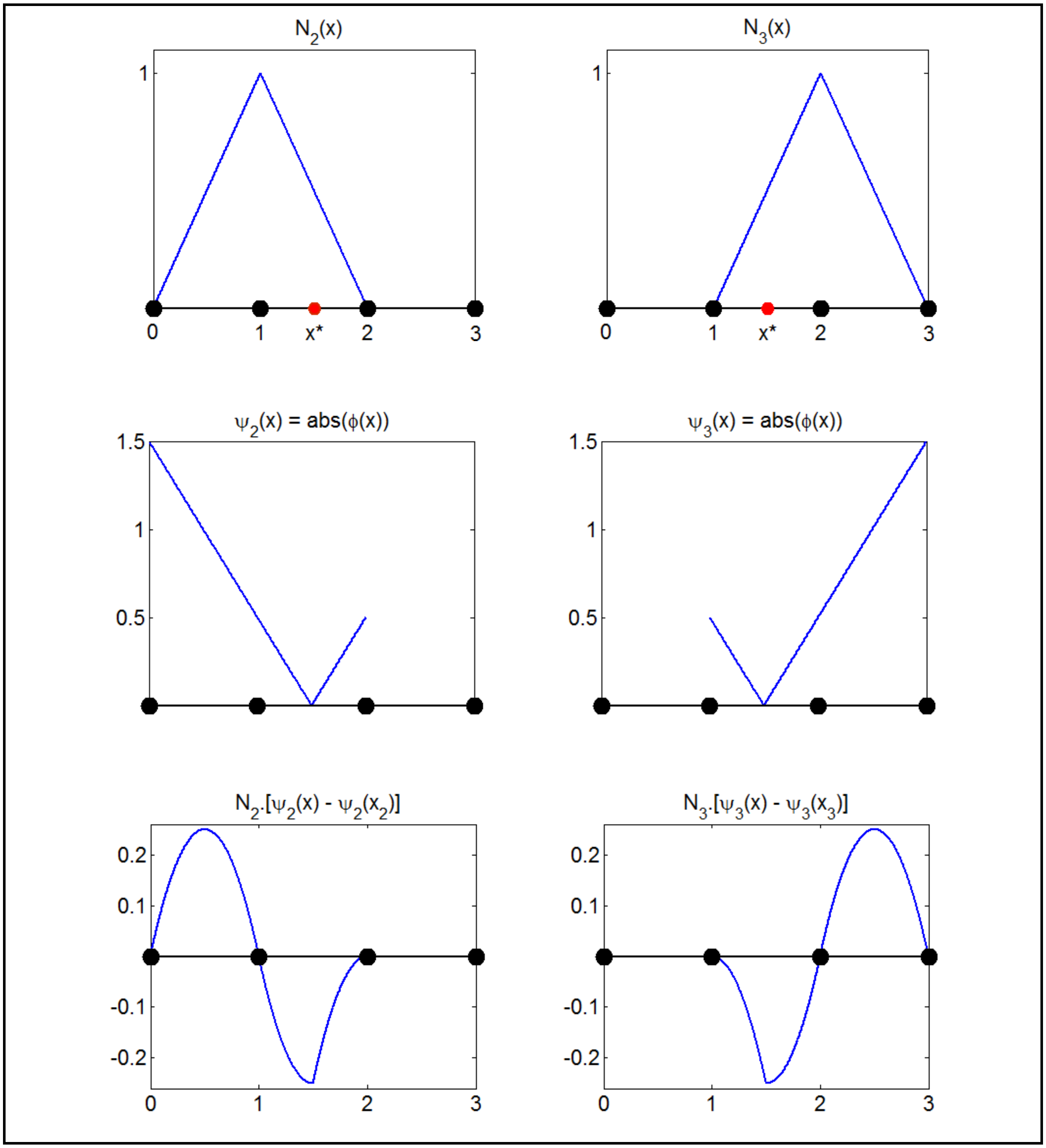

Figure 2.4 Enriched basis function for a weak discontinuity in 1D

However, the abs-enrichment is not zero in partially-enriched elements (cf. Figure 2.4). The functions $N_i^*(\mathbf{x})$ do not build a global partition of unity in Ω, so convergence and instability problems may result. Therefore, the modified abs-enrichment as proposed by Moës et al.

(Moës, Cloirec et al. 2003) (also known as the Ridge function) is also considered in our study, since it is zero in the blending elements. This enrichment function is given by:

$$\psi_{\mathrm{R}}(\mathbf{x},t)=\sum_{i\in I}\left|\phi(\mathbf{x}_i,t)\right|N_i(\mathbf{x})-\left|\sum_{i\in I}\phi(\mathbf{x}_i,t)\,N_i(\mathbf{x})\right| \tag{2.11}$$

Remark

It is important to note that the enrichment term in the XFEM approximation and thereby the approximation itself is time dependant.

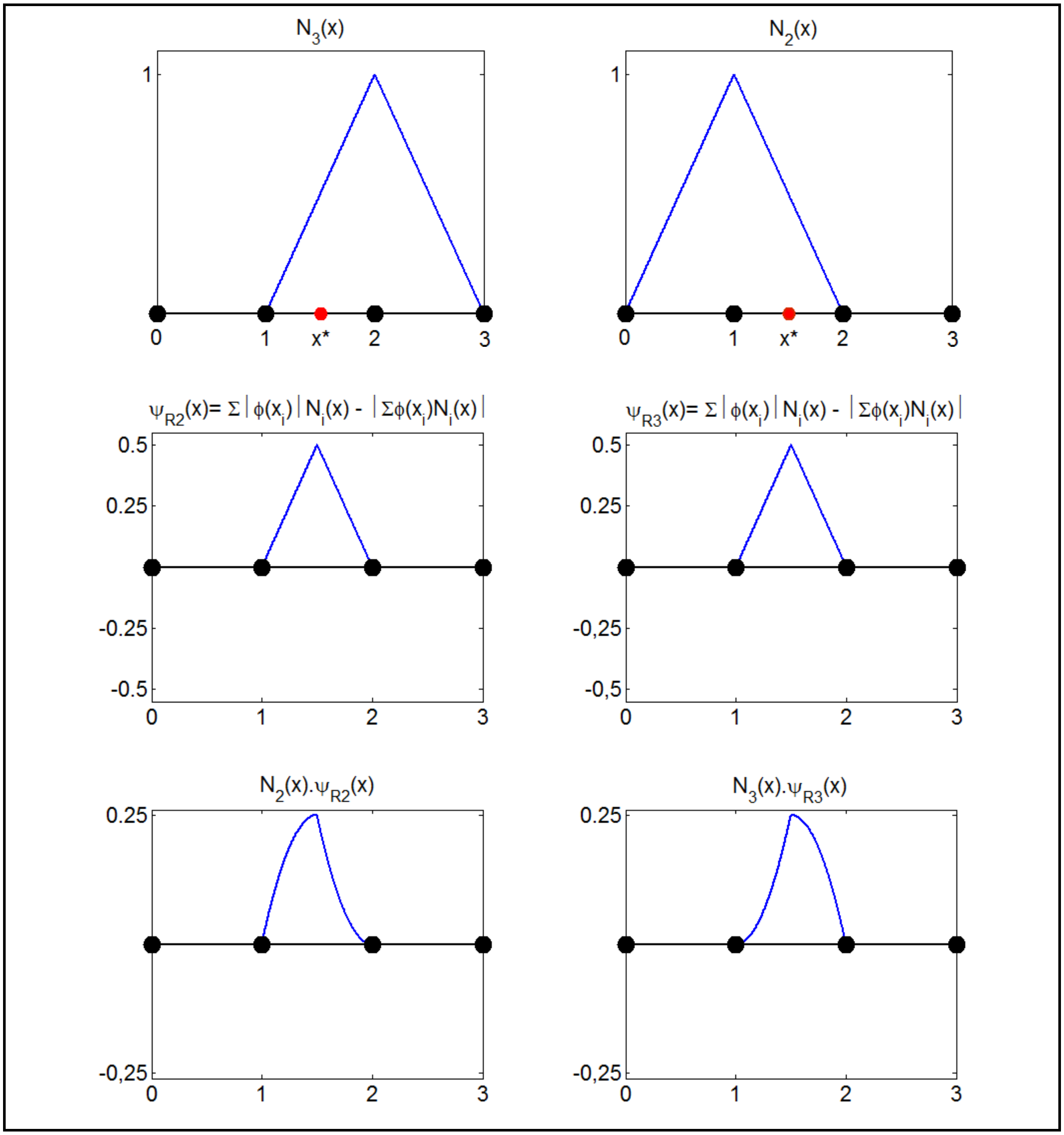

Figure 2.5 Enriched basis function for modified abs-enrichment (Moës, Cloirec et al. 2003) for a weak discontinuity in 1D

The level set function, as a scalar function, is discretized by the shape functions $N_i^{\phi}(\mathbf{x})$ (the same as for the velocity in the standard FEM):

$$\phi(\mathbf{x},t)=\sum_{i\in I} N_i^{\phi}(\mathbf{x})\,\phi_i(t) \tag{2.12}$$

where $\phi_i = \phi(\mathbf{x}_i)$ is the value of the level set function at node i.

2.3 Example: One dimension bi-material bar

This section serves the purpose to demonstrate the XFEM in a particular realization for the case of a weak discontinuity. We consider the example of a bi-material 1D rod in traction. Let us assume a bar of length $\mathrm{L}=1$ unit with two distinct Young moduli $E_1=1$ unit and $E_2=2$ unit subject to a traction force $F=1$ unit along the x axis (see Figure 2.6).

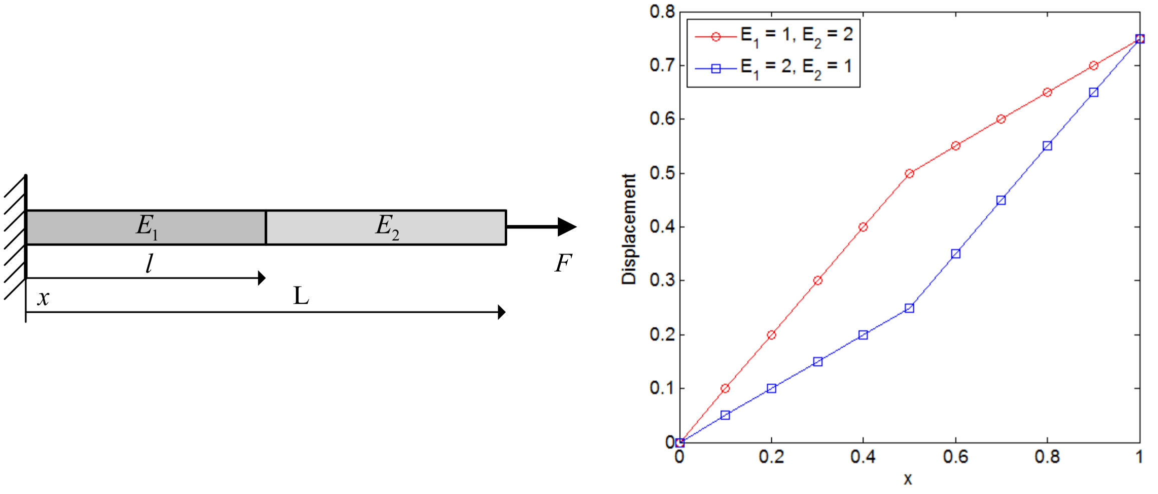

(a) Problem statement (b) Exact solution

Figure 2.6 Bi-material rod in traction

We can see in Figure 2.6 that the displacement field u present a kink (first order discontinuity) in $x^* = l$. The governing equation for a constant section A and no line force is in strong form

$$E_k\, A \frac{\partial^2 u}{\partial x^2} = 0 \tag{2.13}$$

and in weak form

$$\begin{aligned}&\int_0^{\mathrm{L}} E\, A \frac{\partial w}{\partial x}\frac{\partial u}{\partial x}\,\mathrm{d}x - \left[E\, A\, w(x) \frac{\partial u}{\partial x} \right]_0^{\mathrm{L}} \\ &= E_1\, A \int_0^{l} \frac{\partial w}{\partial x}\frac{\partial u}{\partial x}\,\mathrm{d}x + E_2\, A \int_l^{\mathrm{L}} \frac{\partial w}{\partial x}\frac{\partial u}{\partial x}\,\mathrm{d}x - F = 0\end{aligned} \tag{2.14}$$

where w denotes the test function.

A direchlet boundary condition is prescribed on the left side $u(0) = 0$ and a Neumann boundary condition on the right $E_2\, A \frac{\partial u(\mathrm{L})}{\partial x} = F$.

The exact solution to this problem is given by:

$$u^{ex}(x) = \begin{cases} \dfrac{F}{E_1 A} x & 0 \le x \le l \\ \dfrac{F}{E_2 A} x + \dfrac{F\, l}{A} \dfrac{E_2 - E_1}{E_2\, E_1} & l < x \le \mathrm{L} \end{cases} \tag{2.15}$$

First degree shape functions are used in this example and the analysis was carried out with a mesh consisting of 3 elements. We can see in Figure 2.7 that the classical finite element approximation fails at reproducing the analytical solution. Using the modified abs-enrichment, the XFEM approximation can retrieve the exact solution of the material rod.

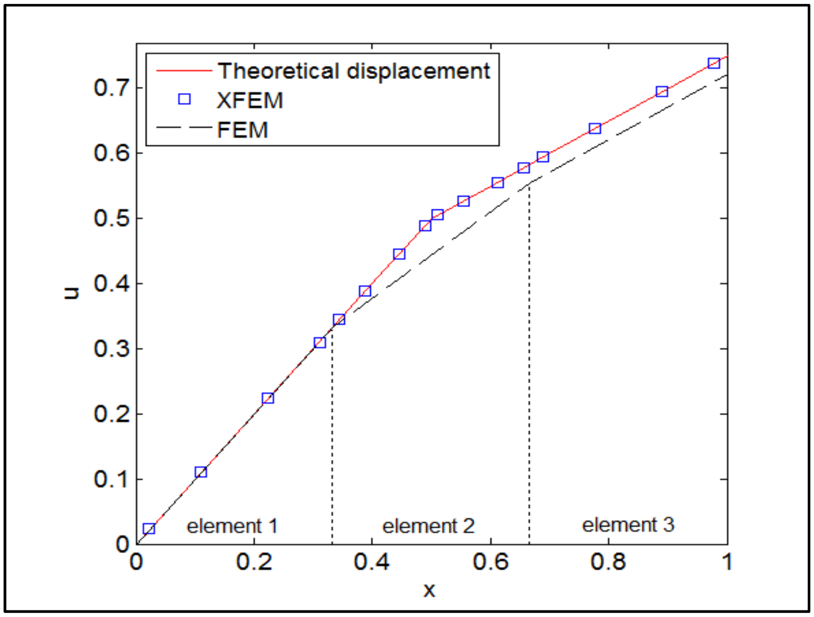

Figure 2.7 XFEM and FEM solutions of the bi-material rod

Using one single element, we can see in Figure 2.8 that the added shape functions are quadratic.

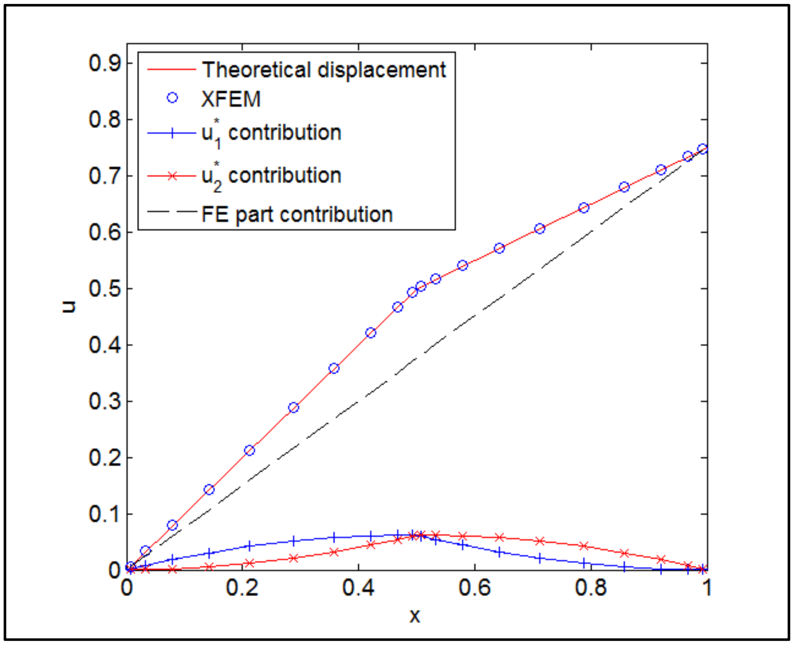

Figure 2.8 XFEM solution with 1 element and modified abs-enrichment function

2.4 Closure

In this chapter, we have given a brief literature review of the XFEM with definitions of the standard enrichment functions used for various kinds of discontinuities. We have seen the advantages of coupling the XFEM and level set methods. The simple examples presented have clarified the idea of introducing specific shape functions to model different discontinuities. We can remark that the integration has to be carried out carefully since the enrichment term in the XFEM approximation present discontinuities inside elements.

Summarized, in the context of the two-phase flows:

- the viscosity jump will require kink enrichment of the velocity field and jump enrichment of the pressure field;
- the density jump and gravity dominated flows will require kink enrichment of the pressure field; and
- surface tension force dominated flows will require jump enrichment of the pressure field.

CHAPTER 3

SPACE AND TIME DISCRETIZATIONS

In this chapter, the weak form of the governing Navier-Stokes and the level set transport equations are first derived. This is then followed by the temporal discretization of the Navier-Stokes equations. The subcell quadrature strategy essential to XFEM is then detailed. Subsequently, the issues of ill-conditioning and time-stepping in XFEM are discussed. The level set updating and the reinitialization procedure are presented next. Finally, the conditions for the inf-sup stability of mixed formulation are reviewed.

3.1 Derivation of the weak formulation of the Navier-Stokes equations

We will now proceed to derive the weak form. The finite element method is used to obtain a numerical solution for the governing equations. Using Galerkin's weight residual method and assuming appropriate solution function spaces $S_{\mathbf{u}}$ for $\mathbf{u}$ and S_p for p as well as weighting function spaces $V_{\mathbf{u}}$ for $\boldsymbol{v}$ and V_p for q, the weak form for the momentum equation (1.3) is given as follows: find $\mathbf{u} \in S_{\mathbf{u}}$ and $p \in S_p$ such that

$$\begin{aligned}\int_{\Omega} \boldsymbol{v} \cdot \rho \left(\frac{\partial \mathbf{u}}{\partial t} + \mathbf{u} \cdot \nabla \mathbf{u} - \mathbf{g} \right) \mathrm{d}\Omega + \int_{\Omega} \boldsymbol{v} \cdot \left(\nabla p - \nabla \cdot (2\mu\, \boldsymbol{\varepsilon}(\mathbf{u})) \right) \mathrm{d}\Omega \\ = \int_{\Gamma_{\text{int}}} \gamma \kappa(\phi)\, \boldsymbol{v} \cdot \mathbf{n}_{\text{int}}\, \mathrm{d}\Gamma \quad \forall \boldsymbol{v} \in V_{\mathbf{u}}\end{aligned} \tag{3.1}$$

The following reformulation can be carried out for the second integral:

$$\begin{aligned}\int_{\Omega} \boldsymbol{v} \cdot \left(\nabla p - \nabla \cdot (2\mu_i\, \boldsymbol{\varepsilon}(\mathbf{u})) \right) \mathrm{d}\Omega &= \int_{\Omega} \boldsymbol{v} \cdot \left(\nabla \cdot \boldsymbol{\sigma} \right) \mathrm{d}\Omega \\ &= \int_{\Gamma_{\mathrm{D}} \cup \Gamma_{\mathrm{N}}} \boldsymbol{v} \cdot \boldsymbol{\sigma} \cdot \mathbf{n}_{\Gamma}\, \mathrm{d}\Gamma - \int_{\Omega} \nabla \boldsymbol{v} : \boldsymbol{\sigma}\, \mathrm{d}\Omega\end{aligned} \tag{3.2}$$

Integration by parts is applied and the resulting boundary integrals are split into their complementary subsets.

$$\begin{aligned}\int_{\Gamma_D \cup \Gamma_N} \boldsymbol{v} \cdot \boldsymbol{\sigma} \cdot \mathbf{n}_\Gamma \,\mathrm{d}\Gamma - \int_\Omega \nabla \boldsymbol{v} : \boldsymbol{\sigma} \,\mathrm{d}\Omega &= \int_{\Gamma_N} \boldsymbol{v} \cdot \mathbf{h} \,\mathrm{d}\Gamma - \int_\Omega \nabla \boldsymbol{v} : \boldsymbol{\sigma} \,\mathrm{d}\Omega \\ &= \int_{\Gamma_N} \boldsymbol{v} \cdot \mathbf{h} \,\mathrm{d}\Gamma + \int_\Omega \nabla \boldsymbol{v}\, p \,\mathrm{d}\Omega - \int_\Omega 2\mu_i\, \boldsymbol{\varepsilon}(\boldsymbol{v}) : \boldsymbol{\varepsilon}(\mathbf{u}) \,\mathrm{d}\Omega\end{aligned} \tag{3.3}$$

In the following, the class of test functions $\boldsymbol{v}$ is restricted to those vanishing on the Dirichlet portion of the boundary Γ_D, i.e. $\boldsymbol{v} = 0$ on Γ_D. Thus, the boundary integral over Γ_D in equation (3.3) drops out. Further applying the Neumann boundary condition (1.8) the expression in equation (3.3) is obtained.

Substituting (3.3) into (3.1), we obtain

$$\begin{aligned}\int_\Omega \rho \boldsymbol{v} \cdot \left(\frac{\partial \mathbf{u}}{\partial t} + \mathbf{u} \cdot \nabla \mathbf{u} - \mathbf{g} \right) \mathrm{d}\Omega - \int_\Omega \nabla \cdot \boldsymbol{v}\, p \,\mathrm{d}\Omega + \int_\Omega 2\mu\, \boldsymbol{\varepsilon}(\boldsymbol{v}) : \boldsymbol{\varepsilon}(\mathbf{u}) \,\mathrm{d}\Omega \\ = \int_{\Gamma_N} \boldsymbol{v} \cdot \mathbf{h} \,\mathrm{d}\Gamma + \int_{\Gamma_{\text{int}}} \gamma \kappa(\phi) \boldsymbol{v} \cdot \mathbf{n}_{\text{int}} \,\mathrm{d}\Gamma \quad \forall \boldsymbol{v} \in V_{\mathbf{u}}\end{aligned} \tag{3.4}$$

The weak form of the continuity equation is found by multiplying (1.4) by the test function q and integrating over the entire domain Ω.

$$\int_\Omega q \nabla \cdot \mathbf{u} \,\mathrm{d}\Omega = 0 \quad \forall q \in V_p \tag{3.5}$$

This is then added to (3.4) to obtain

$$\begin{aligned}&\int_\Omega \rho\,\boldsymbol{v}\cdot\left(\frac{\partial \mathbf{u}}{\partial t}+\mathbf{u}\cdot\nabla\mathbf{u}-\mathbf{g}\right)\mathrm{d}\Omega-\int_\Omega \nabla\cdot\boldsymbol{v}\,p\,\mathrm{d}\Omega+\int_\Omega 2\mu\,\boldsymbol{\varepsilon}(\boldsymbol{v}):\boldsymbol{\varepsilon}(\mathbf{u})\,\mathrm{d}\Omega\\&+\int_\Omega q\,\nabla\cdot\mathbf{u}\,\mathrm{d}\Omega=\int_{\Gamma_\mathrm{N}}\boldsymbol{v}\cdot\mathbf{h}\,\mathrm{d}\Gamma+\int_{\Gamma_\mathrm{int}}\gamma\,\kappa(\phi)\,\boldsymbol{v}\cdot\mathbf{n}_\mathrm{int}\,\mathrm{d}\Gamma\quad\forall\boldsymbol{v}\in V_\mathbf{u},\forall q\in V_p\end{aligned}\tag{3.6}$$

The weak form can be written as

$$W=W_{\mathrm{N-S}}+W_{\mathrm{Cont}}\tag{3.7}$$

where

$$\begin{aligned}W_{\mathrm{N-S}}=&\int_\Omega \rho\,\nu_x\left[\frac{\partial u}{\partial t}+u\frac{\partial u}{\partial x}+\upsilon\frac{\partial u}{\partial y}-g_x\right]\mathrm{d}\Omega+\int_\Omega\left[\frac{\partial \nu_x}{\partial x}2\mu\frac{\partial u}{\partial x}+\frac{\partial \nu_x}{\partial y}\mu\left(\frac{\partial u}{\partial y}+\frac{\partial \upsilon}{\partial x}\right)\right]\mathrm{d}\Omega\\&+\int_\Omega \rho\,\nu_y\left[\frac{\partial \upsilon}{\partial t}+u\frac{\partial \upsilon}{\partial x}+\upsilon\frac{\partial \upsilon}{\partial y}-g_y\right]\mathrm{d}\Omega+\int_\Omega\left[\frac{\partial \nu_y}{\partial x}\mu\left(\frac{\partial u}{\partial y}+\frac{\partial \upsilon}{\partial x}\right)+\frac{\partial \nu_y}{\partial y}2\mu\frac{\partial \upsilon}{\partial y}\right]\mathrm{d}\Omega\\&-\int_\Omega\frac{\partial \nu_x}{\partial x}p\,\mathrm{d}\Omega-\int_{\Gamma_\mathrm{int}}\gamma\,\kappa(\phi)\,\nu_x\,n_{x,\mathrm{int}}\,\mathrm{d}\Gamma-\int_\Omega\frac{\partial \nu_y}{\partial y}p\,\mathrm{d}\Omega-\int_{\Gamma_\mathrm{int}}\gamma\,\kappa(\phi)\,\nu_y\,n_{y,\mathrm{int}}\,\mathrm{d}\Gamma\\&+\int_\Gamma \nu_x\,p\,n_{x,\Gamma}\,\mathrm{d}\Gamma-\int_\Gamma\left[\nu_x\,2\mu\frac{\partial u}{\partial x}n_{x,\Gamma}+\nu_x\,\mu\left(\frac{\partial u}{\partial y}+\frac{\partial \upsilon}{\partial x}\right)n_{x,\Gamma}\right]\mathrm{d}\Gamma\\&-\int_\Gamma\left[\nu_y\,\mu\left(\frac{\partial u}{\partial y}+\frac{\partial \upsilon}{\partial x}\right)n_{x,\Gamma}+\nu_y\,2\mu\frac{\partial \upsilon}{\partial y}n_{y,\Gamma}\right]\mathrm{d}\Gamma+\int_\Gamma \nu_y\,p\,n_{y,\Gamma}\,\mathrm{d}\Gamma\end{aligned}\tag{3.8}$$

$$W_{\mathrm{Cont}}=\int_\Omega q\left(\frac{\partial u}{\partial x}+\frac{\partial \upsilon}{\partial y}\right)\mathrm{d}\Omega\tag{3.9}$$

It is obvious from (3.6) that only first order derivatives of both the trial functions $\mathbf{u}$ and the test functions $\boldsymbol{v}$ appear. No derivatives of the pressure and the pressure test function q

occur. Moving on the boundary conditions, it is noted that the Neumann boundary condition (1.8) is incorporated as a natural boundary in the weak form.

The formulation (3.6) is discretized using the enriched Taylor-Hood element on triangles P2/P1 (quadratic velocity/linear pressure) or on rectangles Q2/Q1 (biquadratic velocity/bilinear pressure), see Figure 3.1. These finite elements satisfy the Babuska-Brezzi condition for single-phase flows (Brezzi and Fortin 1991); hence, it is not necessary to stabilize the continuity equation.

It should be noted that for high Reynolds numbers, it is possible to add some stabilization terms to the Galerkin weak form, as in the SUPG, GLS, and VMS methods of Hughes (Hughes, Feijóo et al. 1998).

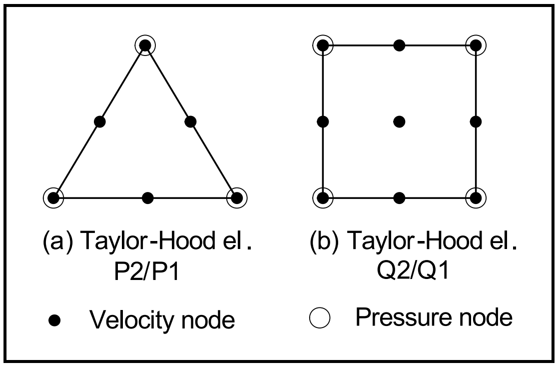

Figure 3.1 Elements used in this work

3.2 Time discretization of the Navier-Stokes equations

A semi-implicit Euler BDF1 (the backward differentiation formula of order 1) scheme is used for time discretization; let us denote by $\mathbf{u}^n$ and p^n the approximations of the velocity $\mathbf{u}$ and pressure p fields at time t^n, respectively, so that the resulting algebraic system of equations reads

$$\begin{bmatrix} \dfrac{1}{\Delta t}\mathbf{M}_{\mathbf{u}}^{n+1} + \mathbf{K}_{\mathbf{u}}^{n+1} + \mathbf{C}_{\mathbf{u}}^{n+1} & \mathbf{G}_{p}^{n+1} \\ \mathbf{G}_{p}^{{n+1}^{\mathrm{T}}} & \mathbf{0} \end{bmatrix} \begin{bmatrix} \bar{\mathbf{U}}^{n+1} \\ \bar{\mathrm{P}}^{n+1} \end{bmatrix} = \begin{bmatrix} \mathbf{F}_{\mathrm{grav}}^{n+1} + \mathbf{F}_{\mathrm{ST}}^{n+1} + \mathbf{F}_{\mathrm{ext}}^{n+1} + \dfrac{1}{\Delta t}\mathbf{M}_{\mathbf{u}}^{n}\,\bar{\mathbf{U}}^{n} \\ \mathbf{0} \end{bmatrix} \tag{3.10}$$

where

$$\bar{\mathbf{U}}^{n+1} = \begin{bmatrix} \mathbf{U}^{n+1} \\ \mathbf{U}^{*\,n+1} \end{bmatrix} \tag{3.11}$$

$$\mathbf{U}^{n+1} = \left[u_1^{n+1}, u_1^{n+1}, \ldots, u_{\mathrm{n}}^{n+1}, \upsilon_1^{n+1}, \upsilon_1^{n+1}, \ldots, \upsilon_{\mathrm{n}}^{n+1} \right]^{\mathrm{T}} \tag{3.12}$$

$$\mathbf{U}^{*n+1} = \left[u_1^{*\,n+1}, u_2^{*\,n+1}, \ldots, u_{\mathrm{n}}^{*\,n+1}, \upsilon_1^{*\,n+1}, \upsilon_2^{*\,n+1}, \ldots, \upsilon_{\mathrm{n}}^{*\,n+1} \right]^{\mathrm{T}} \tag{3.13}$$

where subscript n is the number of degrees of freedom for the velocity.

$$\bar{\mathbf{P}}^{n+1} = \begin{bmatrix} \mathbf{P}^{n+1} \\ \mathbf{P}^{*\,n+1} \end{bmatrix} \tag{3.14}$$

$$\mathbf{P}^{n+1} = \left[p_1^{n+1}, p_1^{n+1}, \ldots, p_{\mathrm{m}}^{n+1} \right]^{\mathrm{T}} \tag{3.15}$$

$$\mathbf{P}^{*\,n+1} = \left[p_1^{*\,n+1}, p_2^{*\,n+1}, \ldots, p_{\mathrm{m}}^{*\,n+1} \right]^{\mathrm{T}} \tag{3.16}$$

where subscript m is the number of degrees of freedom for the pressure.

$$\mathbf{M}_{\mathbf{u}}^{n+1} = \int_{\Omega} \rho^{n+1} (\bar{\mathbf{N}}^{\mathbf{u}})^{n+1} (\bar{\mathbf{N}}^{\mathbf{u}})^{{n+1}^{\mathrm{T}}} \,\mathrm{d}\Omega, \tag{3.17}$$

$$\mathbf{M}_{\mathbf{u}}^{n} = \int_{\Omega} \rho^{n} (\bar{\mathbf{N}}^{\mathbf{u}})^{n+1} (\bar{\mathbf{N}}^{\mathbf{u}})^{n^{\mathrm{T}}} \, \mathrm{d}\Omega, \tag{3.18}$$

$$\mathbf{K}_{\mathbf{u}}^{n+1} = \begin{bmatrix} K_{uu}^{n+1} & K_{u\upsilon}^{n+1} \\ K_{\upsilon u}^{n+1} & K_{\upsilon\upsilon}^{n+1} \end{bmatrix} \tag{3.19}$$

$$K_{uu}^{n+1} = \int_{\Omega} \mu^{n+1} \left[2 (\bar{\mathbf{N}}_{,x}^{\mathbf{u}})^{n+1} (\bar{\mathbf{N}}_{,x}^{\mathbf{u}})^{{n+1}^{\mathrm{T}}} + (\bar{\mathbf{N}}_{,y}^{\mathbf{u}})^{n+1} (\bar{\mathbf{N}}_{,y}^{\mathbf{u}})^{{n+1}^{\mathrm{T}}} \right] \mathrm{d}\Omega, \tag{3.20}$$

$$K_{u\upsilon}^{n+1} = \int_{\Omega} \mu^{n+1} (\bar{\mathbf{N}}_{,y}^{\mathbf{u}})^{n+1} (\bar{\mathbf{N}}_{,x}^{\mathbf{u}})^{{n+1}^{\mathrm{T}}} \, \mathrm{d}\Omega, \tag{3.21}$$

$$K_{\upsilon u}^{n+1} = \int_{\Omega} \mu^{n+1} (\bar{\mathbf{N}}_{,x}^{\mathbf{u}})^{n+1} (\bar{\mathbf{N}}_{,y}^{\mathbf{u}})^{{n+1}^{\mathrm{T}}} \, \mathrm{d}\Omega, \tag{3.22}$$

$$K_{\upsilon\upsilon}^{n+1} = \int_{\Omega} \mu^{n+1} \left[(\bar{\mathbf{N}}_{,x}^{\mathbf{u}})^{n+1} (\bar{\mathbf{N}}_{,x}^{\mathbf{u}})^{{n+1}^{\mathrm{T}}} + 2 (\bar{\mathbf{N}}_{,y}^{\mathbf{u}})^{n+1} (\bar{\mathbf{N}}_{,y}^{\mathbf{u}})^{{n+1}^{\mathrm{T}}} \right] \mathrm{d}\Omega, \tag{3.23}$$

$$\mathbf{C}_{\mathbf{u}}^{n+1} = \int_{\Omega} \rho^{n+1} (\bar{\mathbf{N}}^{\mathbf{u}})^{n+1} \, \mathbf{u}^{n} \cdot (\nabla \bar{\mathbf{N}}^{\mathbf{u}})^{{n+1}^{\mathrm{T}}} \, \mathrm{d}\Omega, \tag{3.24}$$

$$\mathbf{G}_{p}^{n+1} = -\int_{\Omega} (\nabla \cdot \bar{\mathbf{N}}^{\mathbf{u}})^{n+1} (\bar{\mathbf{N}}^{p})^{{n+1}^{\mathrm{T}}} \, \mathrm{d}\Omega, \tag{3.25}$$

$$\mathbf{F}_{\mathrm{grav}}^{n+1} = \int_{\Omega} \rho^{n+1} (\bar{\mathbf{N}}^{\mathbf{u}})^{n+1} \, \mathbf{g} \, \mathrm{d}\Omega, \tag{3.26}$$

$$\mathbf{F}_{\mathrm{ST}}^{n+1} = \int_{\Gamma_{\mathrm{int}}} \gamma \, \kappa(\phi) \, (\bar{\mathbf{N}}^{\mathbf{u}})^{n+1} \, \mathbf{n}_{\mathrm{int}} \, \mathrm{d}\Gamma, \tag{3.27}$$

$$\mathbf{F}_{\mathrm{ext}}^{n+1} = \int_{\Gamma_{\mathrm{N}}} (\bar{\mathbf{N}}^{\mathbf{u}})^{n+1} \, \mathbf{h} \, \mathrm{d}\Gamma. \tag{3.28}$$

and where $\bar{\mathbf{N}}$ includes the enrichment functions:

$$\bar{\mathbf{N}}(\mathbf{x},\phi)=\left[N_1,N_1,\ldots,N_{nn},M_1,M_1,\ldots,M_{nn}\right]^{\mathrm{T}} \tag{3.29}$$

Following the proposed time discretization, the discrete semi-implicit formulation (3.10) yields a linear problem in the variables $\mathbf{u}^{n+1}$ and p^{n+1} to be solved only once at each time t^{n+1}.

3.3 Strategies for numerical integrations

Due to the addition of discontinuous enrichment functions in the approximation space, some parts of the integrands in the weak formulation (3.6) also comprise discontinuities. Therefore, the application of the standard Gauss quadrature leads to significant errors. Particular procedures are required for an accurate quadrature of the weak formulation, see, e.g., (Fries and Belytschko 2010).

3.3.1 Decomposition of elements

We can decompose an element Ω^e into sub-elements Ω_i^e such that $\cup_i \Omega_i^e=\Omega^e$, $\cap_i \Omega_i^e=\varnothing$. Since

$$\begin{aligned}\int_{\Omega^e} g\,\mathrm{d}\Omega^e &= \sum_i \int_{\Omega_i^e} g\,\mathrm{d}\Omega_i^e \\ &\approx \sum_i \sum_{j=1}^{Q} \omega_j^i\, g\left(\mathbf{x}_j^i\right)\end{aligned} \tag{3.30}$$

Where $\mathbf{x}_j^i$ and ω_j^i are the knot points and weights of the $Q-$point Gauss quadrature used in sub-element Ω_i^e. This decomposition does not affect the value of the analytic integral.

However, if we can choose a decomposition such that the integrand g is smooth on each sub-element then standard Gauss quadrature can be used on each part and the same accuracy can be obtained for the integration over elements with a discontinuity as for those without. The sub-elements are used simply for the integration so they need not conform, and they introduce ne new unknowns into the problem. We exclude the case where the interface intersects the same element edge twice.

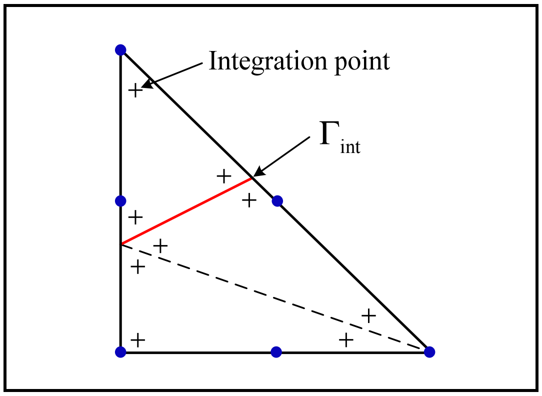

Figure 3.2 Sub-elements and integration points. Red line depicts the interface, and blue points depict the nodes

Decomposing into sub-elements of the same type as the original element has the advantage that the element's integration scheme can be used. The order of the integration scheme must be increased for integrals involving enriched basis function they have a higher polynomial degree.

Figure 3.3(a) shows the integration error committed. For quadratic elements, the use of a linear approximation of the interface inside each cut element is not adequate. To improve the numerical integration we consider a piecewise linear interface. The cut quadratic element is subdivided into four triangular sub-elements so that linear interpolation of the interface can be employed in each. We see in Figure 3.3(b) that this approach is much accurate, and will be used later for all numerical examples.

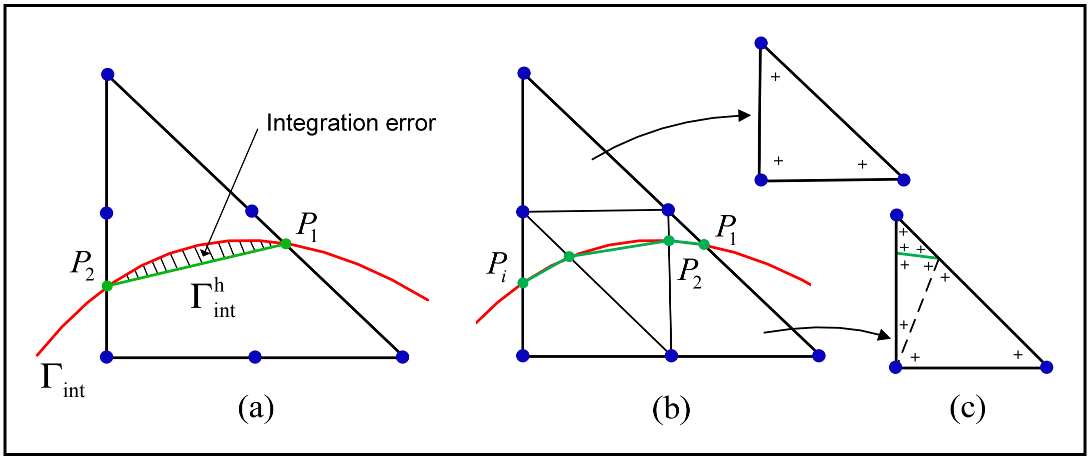

Figure 3.3 Curved interface inside a quadratic element and integration error committed with the linear approximation of the interface. In green, the approximated interface and computed points P_i on the interface

In the case of a curved interface, the estimation of the iso-zero level set position P_i can suffer from imprecisions, as shown in Figure 3.4.

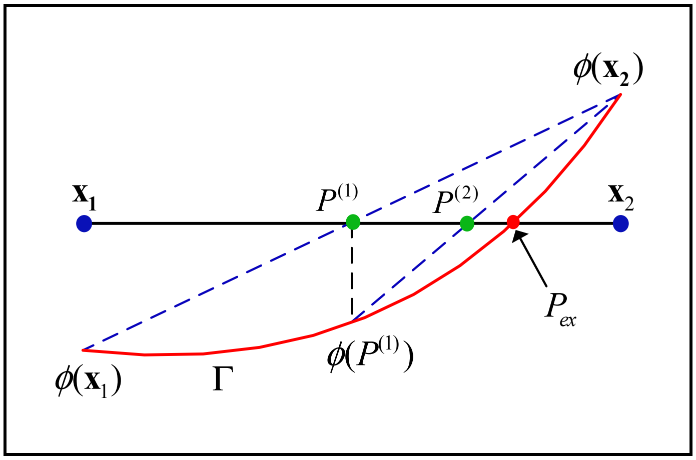

Figure 3.4 Estimation of the iso-zero level set position. In blue, grid points

To obtain a better geometrical accuracy, we implement the secant method (Norato, Haber et al. 2004).

$$P^{(i+1)} = P^{(i)} - \frac{\phi(P^{(i)})}{\phi(P^{(i)}) - \phi(\mathbf{x}_n)}\left(P^{(i)} - \mathbf{x}_n\right) \quad \text{if } \phi(P^{(i)})\phi(\mathbf{x}_n) < 0 \tag{3.31}$$

where $\phi(\mathbf{x}_n)$ is the level set value at node 1 or 2 (for example, in Figure 3.4: $P^{(0)} = \mathbf{x}_1$ and $\mathbf{x}_n = \mathbf{x}_2$). The procedure is repeated until $\left|\phi(P^{i+1})\right| \le \varepsilon_s$. We use two iterations in our computations ($\varepsilon_s = 10^{-3}$).

3.3.2 Linear dependence and ill-conditioning

One disadvantage of the XFEM is that an ill-conditioned system of equations may occur in some circumstances, specifically, if a sub-element of an intersected element is too small (as in Figure 3.5) , the matrix will be ill-conditioned (Fries and Belytschko 2010).

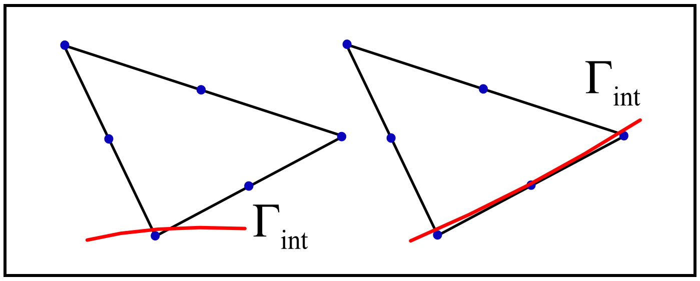

Figure 3.5 An interface passing close to a vertex (left) or edge (right)

It is common to remove the enrichments associated with these nodes (Bordas, Nguyen et al. 2007), whose enrichment functions have very small supports, by imposing a Dirichlet boundary condition. For any corner node i,

$$\mathbf{u}_i^* = 0 \text{ and } p_i^* = 0 \quad \text{if } \left|\phi_i\right| \le \phi_{\min} \tag{3.32}$$

for example, in this work $\phi_{\min} = \min(\mathrm{h}^e)\cdot 10^{-3}$. An alternative option is to apply special preconditioners in the solution phase (Béchet, Minnebo et al. 2005).

Another possibility is to shift the level set of these nodes during the XFEM iteration in order to improve the ratio of the areas on both sides of the interface. The nodal level set value is thus changed to:

$$\phi_i^{\mathrm{corr}} = \phi_i + \mathrm{sign}(\phi_i)\cdot\phi_{\min} \quad \text{if } |\phi_i| \le \phi_{\min} \tag{3.33}$$

where i is a corner node. In this work, we choose the last strategy (3.33), that of shifting the level set.

3.3.3 Time-Stepping in the XFEM

In problem with stationary interfaces, the level set function is kept fixed. In this case the enriched basis functions are independent of time. However, in problems with moving interface, the level set function varies with time.
Chessa et al. (Chessa, Smolinski et al. 2002) and Chessa and Belytschko (Chessa and Belytschko 2004; Chessa and Belytschko 2006) have identified that serious problems may occur if standard time-integration methods from the classical FEM are used with time-dependent enrichments.

The time integration of the local acceleration term in the weak form requires that special attention be given to the cut elements. Note that the interface positions in time levels n and $n+1$ are required. This is a consequence of integrating the mass matrix $\mathbf{M}_{\mathbf{u}}^n$.

$$\mathbf{M}_{\mathbf{u}}^n = \int_\Omega \rho^n (\bar{\mathbf{N}}^{\mathbf{u}})^{n+1}_{\Gamma_{\mathrm{int}}(t^{n+1})} (\bar{\mathbf{N}}^{\mathbf{u}})^{n^{\mathrm{T}}}_{\Gamma_{\mathrm{int}}(t^n)} \, \mathrm{d}\Omega \tag{3.34}$$

Fries and Zilian (Fries and Zilian 2009) specified that it is essential in this case to use a more elaborate quadrature in cut-elements that considers $\Gamma_{\text{int}}(t^n)$ and $\Gamma_{\text{int}}(t^{n+1})$. However, as only the cut elements are enriched, there are some nodes that were enriched at the previous time level but are not enriched at the current time level, and vice versa. That is, some enrichment degrees of freedom are removed, and new ones are added.

Rasthofer et al. (Rasthofer, Henke et al. 2011), suggested a quasi-static enrichment approach for the velocity field, that consists of ignoring the enrichment part of the previous time level:

$$\mathbf{u}^n = \sum_{i \in I} N_i^{\mathbf{u}}(\mathbf{x})(\mathbf{u}_i^n)_{\Gamma_{\text{int}}(t^n)} \tag{3.35}$$

In this work, this simpler approach is used. For further discussion, we refer the reader to Henke’s thesis (Henke 2012).

3.4 Derivation of the weak formulation of the level set transport equation

To obtain the weak formulation of the level set transport equation using the Streamline Upwind Petrov-Galerkin (SUPG) finite element method, an appropriate solution function space S_ϕ for ϕ and a weighting function space V_ϕ for $\boldsymbol{w}$ are assumed: find $\phi \in S_\phi$ such that

$$\begin{aligned} &\int_\Omega \boldsymbol{w} \cdot \left(\frac{\partial \phi}{\partial t} + \mathbf{u} \cdot \nabla \phi \right) \mathrm{d}\Omega + \\ &\sum_{e=1}^{ne} \int_{\Omega^e} \tau_{\mathrm{L}} (\mathbf{u} \cdot \nabla \boldsymbol{w}) \cdot \left(\frac{\partial \phi}{\partial t} + \mathbf{u} \cdot \nabla \phi \right) \mathrm{d}\Omega = 0 \quad \forall\, \boldsymbol{w} \in \mathrm{V}_\phi \end{aligned} \tag{3.36}$$

where τ_{L} is the SUPG stabilization parameter. There are numerous definitions for this parameter proposed in the literature; we use the simplest definition

$$\tau_{\mathrm{L}} = \frac{1}{\sqrt{\left(\frac{2}{\Delta t}\right)^2 + \left(\frac{2\|\mathbf{u}\|}{\mathrm{h}^e}\right)^2}} \tag{3.37}$$

where Δt denotes the time-step length.

3.5 Level set update and reinitialization

The temporal part of the level set equation is discretized using a sufficiently accurate explicit time-marching scheme. For this purpose, we use the strong-stability preserving (SSP) explicit high-order TVD Runge-Kutta method (Shu and Osher 1989).

If we rewrite (1.19) as

$$\frac{\partial \phi}{\partial t} = -\mathbf{u} \cdot \nabla \phi = L(\phi) \tag{3.38}$$

then, for example, the third order SSP Runge-Kutta method gives

$$\begin{aligned} \phi^{(1)} &= \phi^n + \Delta t\, L(\phi^n) \\ \phi^{(2)} &= \frac{3}{4}\phi^n + \frac{1}{4}\left(\phi^{(1)} + \Delta t\, L(\phi^{(1)})\right) \\ \phi^{n+1} &= \frac{1}{3}\phi^n + \frac{2}{3}\left(\phi^{(2)} + \Delta t\, L(\phi^{(2)})\right) \end{aligned} \tag{3.39}$$

3.5.1 Numerical example: Vortex in a box

In this example, we measure a dissipation error that is relevant in level set method. If the velocity field $\mathbf{u}$ is incompressible (i.e. $\nabla \cdot \mathbf{u} = 0$), then area delimited by iso-zero level set should be conserved in time. Our problem is the vortex in a box, introduced by Bell et al.

(Bell, Colella et al. 1989) and applied as a level set test problem by Enright et al. (Enright, Fedkiw et al. 2002). We consider a disk of radius $r = 0.15$ placed at $(0.50, 0.75)^{\mathrm{T}}$. The initial level set function is given by

$$\phi(\mathbf{x}) = r - \sqrt{(x-0.50)^2 + (y-0.75)^2} \tag{3.40}$$

The computational domain is a square of size $[0,1]\times[0,1]$. We consider the following stream function

$$\psi = \frac{1}{\pi}\sin^2(\pi x)\sin^2(\pi y) \tag{3.41}$$

That defines the following velocity field

$$\begin{aligned} u &= \frac{\partial \psi}{\partial y} = \sin(2\pi y)\sin^2(\pi x) \\ \upsilon &= -\frac{\partial \psi}{\partial x} = -\sin(2\pi x)\sin^2(\pi y). \end{aligned} \tag{3.42}$$

By multiplying $\mathbf{u}$ by a periodic function in time $g(t) = \cos(\pi t/T)$, the velocity field is inverted after half of the period $T = 8\ \mathrm{s}$ and the level set function ϕ comes back to its initial position. The domain is discretized using 50×50 triangular elements. Figure 3.6 shows the evolution in time of the disk (represented by the iso-zero level set). Result provided by a pure advection of the level set function, i.e. by merely solving the level set transport equation (1.19).

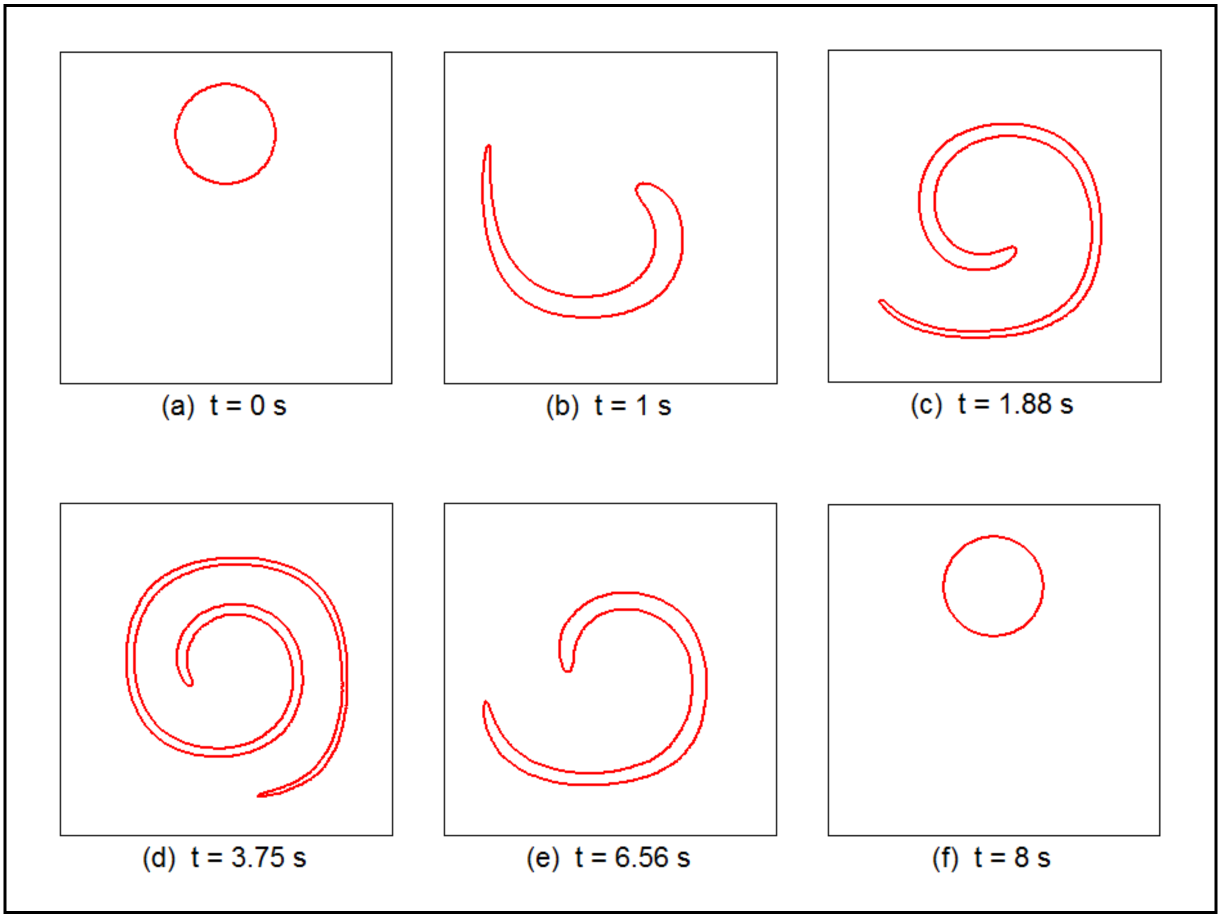

Figure 3.6 Time evolution of the iso-zero level set for the vortex in a box

Figure 3.7 shows a zoom of the superposition of the initial solution and the solution after one period.

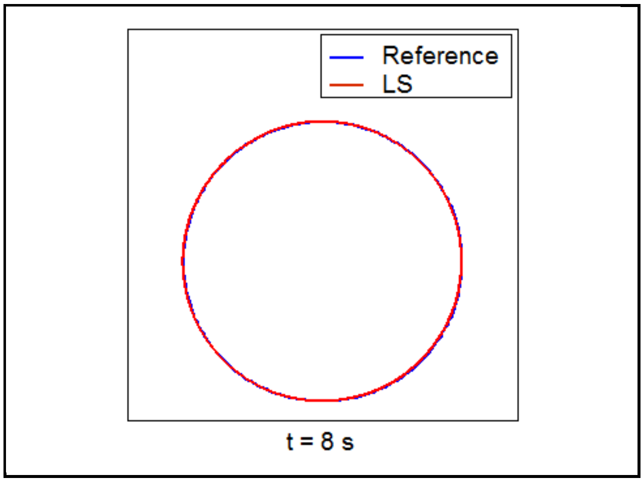

Figure 3.7 Comparison of the final shape of the iso-zero level set for the vortex in a box. The initial shape of the disk is taken as a reference

A more detailed insight into area (or mass) conservation is obtained from (3.43), which provides the area of the disk $A\left(\Omega_{\mathrm{d}}(t)\right)$, given in terms of the initial area $A\left(\Omega_{\mathrm{d}}(t=0)\right)$ as

$$\mathrm{a}\,\% = \frac{A\left(\Omega_{\mathrm{d}}(t)\right)}{A\left(\Omega_{\mathrm{d}}(t=0)\right)} \times 100 \tag{3.43}$$

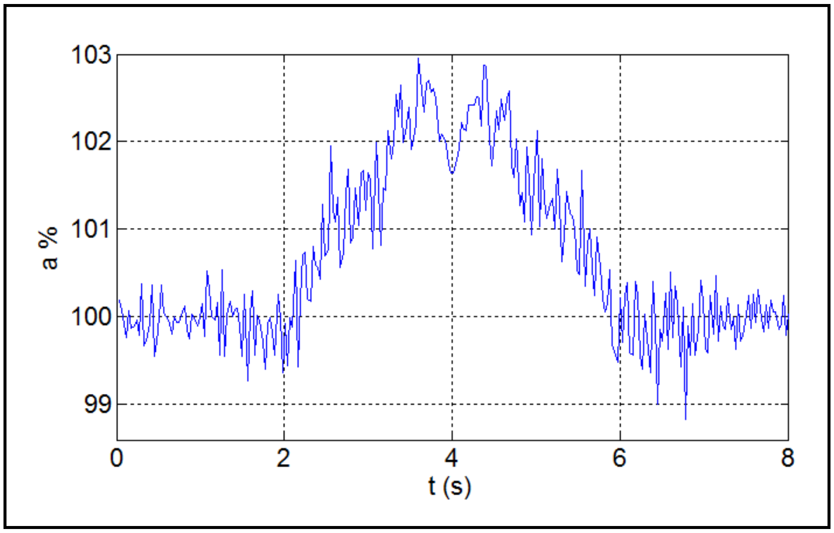

Figure 3.8 Area of the disk over time t

We observe that the interface is retained accurately.

3.5.2 Reinitialization

Because the level set function is transported by the discrete velocity field, its smoothness and its distance function properties (i.e. $\|\nabla\phi(\mathbf{x},t)\|=1$) will not necessarily be preserved due to the accumulation of numerical errors. A reinitialization process is usually adopted when updating the level set function ϕ such that the intended smoothness and properties are maintained as much as possible throughout the simulation. There are many ways to reinitialize the signed distance function, including using a straightforward method, as in (Merriman, Bence et al. 1994; Smolianski 2001), or solving a Hamilton-Jacobi type PDE, as in (Sussman, Smereka et al. 1994; Peng, Merriman et al. 1999). Only the straightforward geometric reinitialization technique is used in this study. This technique is simple; it consists of subdividing the cut elements recursively into sub-elements of the same type (for details, please refer to section 4.1.2), finding the points on the interface with a zero level set in each sub-element, and connecting those points with straight segments S_i that are stored. Figure 3.9 shows a refined mesh of level 4 to localize a circular interface.

Next, the signed distance from a point $\mathbf{x}$ that does not belong to any cut element to the set of segments S_i is computed as

$$\phi_{\text{mod}}(\mathbf{x})=\text{sign}\left(\phi(\mathbf{x})\right)\times\min_i\left(dist\left(\mathbf{x},S_i\right)\right),\quad\forall\mathbf{x}\in\Omega\cap I^* \tag{3.44}$$

where I^* denotes the set of near nodes defined in section 2.2.

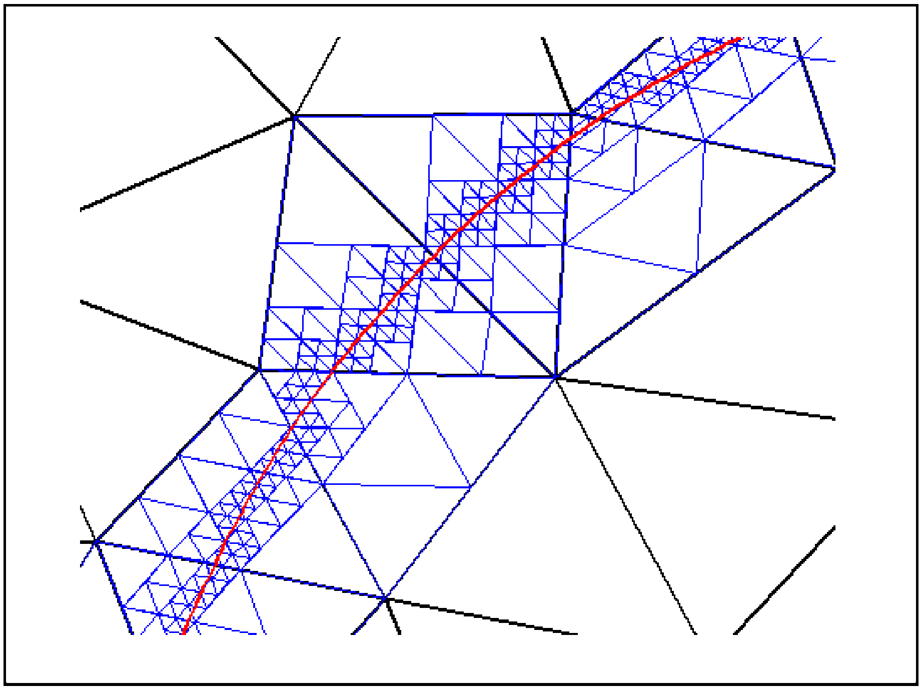

Figure 3.9 Example of recursive subdivision of level 4 to localize a circular interface. In black, the initial mesh. In blue, the refined mesh

As an illustration, consider a distorted circle on the domain $\Omega=[-0.02, 0.02]^2$; the interface is the circle with center $(0, 0)^{\mathrm{T}}$ and radius $r=0.01$. We disturb the level set by a random signal, and the obtained perturbed level set function is given by equation (3.45), such that the interface $\Gamma(\phi)$ is unchanged and the other iso-contours are gradually made false (cf. Figure 3.10a). Applying the reinitialization scheme, the corrected iso-contours are found in Figure 3.10b.

$$\phi(x, y) = l + \frac{r}{20}\sin\left(\frac{\pi l}{r}\right)\sin(5\theta) \tag{3.45}$$

with $l = r - \sqrt{x^2 + y^2}$ and $\theta = \tan^{-1}(y/x)$.

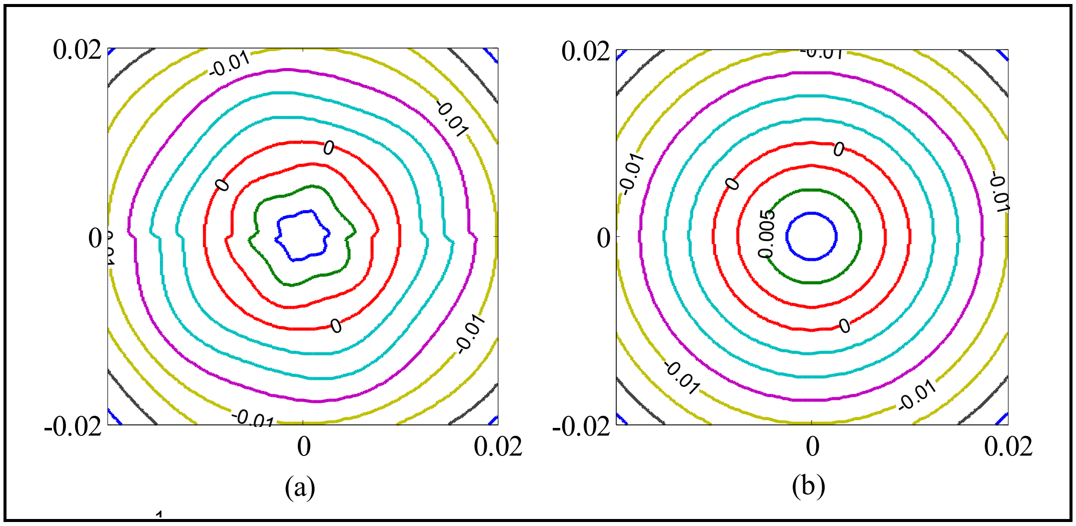

(a)

(b)

Figure 3.10 Reinitialization of the level set function using a recursive subdivision of level 4: (a) before the reinitialization; (b) after the reinitialization

3.6 Inf-sup stability issue with XFEM

The standard $\mathrm{P2}/\mathrm{P1}$ approximations satisfy the inf-sup stability condition for single-phase flows. As the enrichments are used, the resulting XFEM element must satisfy the compatibility condition (also known as the LBB condition)

$$\inf_{q^h \in S_p} \sup_{\mathbf{v}^h \in S_{\mathbf{u}}} \frac{\int_\Omega q^h \operatorname{div}(\mathbf{v}^h)\, \mathrm{d}\Omega}{\left\| \mathbf{v}^h \right\|_1 \left\| q^h \right\|_0} = \beta_h \geq \beta_0 > 0 \tag{3.46}$$

where $\left\| \bullet \right\|_1$ and $\left\| \bullet \right\|_0$ denote the H^1 and L^2 norms, respectively, and β_0 is the stability coefficient independent of the mesh size h^e. If the inf-sup stability condition is satisfied, then the numerical solution $(\mathbf{u}^h, p^h)$ is oscillation-free and converges to the exact solution $(\mathbf{u}_{ex}, p_{ex})$ at the optimal order

$$\left\| \mathbf{u}_{ex} - \mathbf{u}^h \right\|_1 + \left\| p_{ex} - p^h \right\|_0 \le \left(1 + \mathrm{C}/\beta_0\right) \left(\inf_{v^h \in S_{\mathbf{u}}} \left\| \mathbf{u}_{ex} - \mathbf{v}^h \right\|_1 + \inf_{q^h \in S_p} \left\| p_{ex} - q^h \right\|_0 \right) \tag{3.47}$$

where C denotes a constant independent of h^e.

The inf-sup stability condition (3.46) is difficult to prove analytically for the XFEM approximations considered (to our knowledge, there is no theoretical proof in the literature). A numerical test has been proposed, in which β_h is evaluated using meshes of increasing refinement (Babuška, Caloz et al. 1994; Babuška and Melenk 1997). If β_h does not decrease to zero as the mesh size is decreased, it can be concluded that the inf-sup stability test is passed for that problem (Legrain, Moës et al. 2008; Sousa, Ausas et al. 2012). Consider the finite element discrete system corresponding to the steady Stokes problem written in the form

$$\begin{bmatrix} \mathbf{K}_{\mathbf{uu}} & \mathbf{K}_{\mathbf{u}p} \\ \mathbf{K}_{\mathbf{u}p}^{\mathrm{T}} & \mathbf{0} \end{bmatrix} \begin{bmatrix} \bar{\mathrm{U}} \\ \bar{\mathrm{P}} \end{bmatrix} = \begin{bmatrix} \mathbf{F} \\ \mathbf{0} \end{bmatrix} \tag{3.48}$$

where

$$\left.\mathbf{K}_{\mathbf{uu}}\right|_{ij} = \int_\Omega \nabla \bar{\mathbf{N}}^{\mathbf{u}} : \nabla \bar{\mathbf{N}}^{\mathbf{u}} \, \mathrm{d}\Omega \quad \forall (i, j) \in \{1, 2, \ldots, \mathrm{n}, \ldots, 2\mathrm{n}\} \times \{1, 2, \ldots, \mathrm{n}, \ldots, 2\mathrm{n}\} \tag{3.49}$$

$$\left.\mathbf{K}_{\mathbf{u}p}\right|_{ij} = -\int_\Omega \mathrm{div}\left(\bar{\mathbf{N}}^{\mathbf{u}}\right) \bar{\mathbf{N}}^p \, \mathrm{d}\Omega \quad \forall (i, j) \in \{1, 2, \ldots, \mathrm{n}, \ldots, 2\mathrm{n}\} \times \{1, 2, \ldots, \mathrm{m}, \ldots, 2\mathrm{m}\} \tag{3.50}$$

with n and m are the numbers of degrees of freedom for the velocity and pressure fields, respectively. We also use the pressure mass matrix, defined by

$$\left.\mathbf{M}_p\right|_{ij} = \int_\Omega \bar{\mathbf{N}}^p \, \bar{\mathbf{N}}^p \, \mathrm{d}\Omega \quad \forall (i, j) \in \{1, 2, \ldots, \mathrm{m}, \ldots, 2\mathrm{m}\} \times \{1, 2, \ldots, \mathrm{m}, \ldots, 2\mathrm{m}\} \tag{3.51}$$

To test if an XFEM scheme is stable, we numerically compute the inf–sup parameter β_h. It can be proven that β_h is given by the square root of the lowest positive eigenvalue of the generalized eigenvalue problem

$$\mathbf{K}_{\mathbf{u}p}^{\mathrm{T}}\,\mathbf{K}_{\mathbf{uu}}^{-1}\,\mathbf{K}_{\mathbf{u}p}\,\mathrm{q} = \lambda\,\mathbf{M}_p\,q \tag{3.52}$$

where $\mathbf{K}_{\mathbf{u}p}^{\mathrm{T}}\,\mathbf{K}_{\mathbf{uu}}^{-1}\,\mathbf{K}_{\mathbf{u}p}$ is the Schur complement.

To solve this eigenvalue problem, the matrices $\mathbf{K}_{\mathbf{uu}}$ and $\mathbf{M}_p$ should be non-singular; therefore, the interface should not pass very close to the nodes (section 3.3.2). If β_h is bounded from below as the mesh is refined, then the inf-stability test is passed and the error approximation is bounded by the projection error of the exact solution $(\mathbf{u}_{ex}, p_{ex})$ onto the enriched finite element spaces. The projection error is expected to converge faster with XFEM than with the standard finite element approximations.

3.7 Closure

In this chapter, we have presented a detailed derivation of the weak form of the Navier-Stokes equations. The strategy of numerical integration is discussed in Section 3.3 were subcell integration is used due to the discontinuous enrichment functions in the XFEM. The intersected quadratic element is subdivided into four triangular sub-elements so that linear interpolation of the interface can be employed in each. Thereafter, the resulting sub-elements are further subdivided to obtain subcells for the purpose of integration.

The weak formulation of the level set equation is given in Section 3.4. For time discretization we have chosen an explicit Runge-Kutta (RK) method of order 3. Because the level set function is transported by the flow velocity, its signed distance property (i.e., $\|\nabla\phi(\mathbf{x},t)\| = 1$) is not preserved. Therefore, a reinitialization procedure is indispensable. In this thesis, we employ a straightforward geometric reinitialization (Section 3.5.2).

In the context of XFEM, there are still important areas open to further research:

- the solution to the ill-conditioned; and
- the development of efficient and accurate techniques for time-stepping in the XFEM.

Improvement has been made in the ill-conditioned, as mentioned in this chapter. However, the issue of the time-stepping is not resolved yet.

CHAPTER 4

NUMERICAL SIMULATION OF SURFACE TENSION EFFECTS

For many multi-fluids flows, surface tension effects may play an important role and can therefore not be neglected. The surface tension forces are a result of the uneven molecular forces of attraction experienced by fluid molecules near the interface. In this chapter we are concerned with the accurate modeling of surface tension forces.

The modeling of surface tension forces is computationally difficult and still remains a challenge for two reasons. The first one is that it requires the computation of the normal and surface curvatures of the interface, i.e., first and second derivatives of the level set function. The second difficulty is that the surface tension is applied at the interface, i.e., in the context of the level set function, on a surface embedded in the mesh.

We recall from the weak formulation of the Navier-Stokes equations (3.6) that the surface tension term is expressed as

$$\gamma \int_{\Gamma_{\mathrm{int}}} \kappa(\phi)\, \boldsymbol{v} \cdot \mathbf{n}_{\mathrm{int}}\, \mathrm{d}\Gamma \tag{4.1}$$

where γ is the surface tension coefficient, κ is the curvature, and $\mathbf{n}_{\mathrm{int}}$ is the unit normal vector to the interface Γ_{int} between the two fluids Ω_1 and Ω_2 (pointing to the domain where $\phi > 0$).

4.1 Numerical computation of normal and curvature

It was noted before that the curvature is given by the Laplacian of the level set function. It is therefore natural to expect that unless $\phi(\mathbf{x})$ is sufficiently smooth, the computed curvature κ will be noisy (Groß and Reusken 2007). In this section, two numerical methods for computing the normal vectors to the interface are discussed and compared. The first method computes the normal vectors using the gradient of the level set function:

$$\mathbf{n}_{\text{int}} = \frac{\nabla\phi}{\|\nabla\phi\|}$$

Smooth normal vectors are reconstructed using the $L2-$projection method. This method is stable and convergent in the sense of L_2. The second method evaluates the normal vectors in a straightforward way. In this method, a multi-level mesh refinement is first realized inside cut elements. Next, the points on the interface with a zero level set in each sub-element are computed and connected with straight segments S_i that are stored. Finally, the normal vectors to the piecewise linear interface are constructed.

4.1.1 L2-projection method

Because the interface normal unit vector $\mathbf{n}_{\text{int}}$ and curvature κ are the first and second derivatives of the level set function, respectively, they can be approximated by a combination of appropriate projection and gradient recovery techniques. The continuous approximation $\mathbf{G}$ of the gradient of the level set function is reconstructed via the L_2-projection:

$$\int_{\Omega} \boldsymbol{w}\cdot\mathbf{G}\,\mathrm{d}\Omega = \int_{\Omega} \boldsymbol{w}\cdot\nabla\phi\,\mathrm{d}\Omega, \quad \forall\,\boldsymbol{w}\in \mathrm{V}_{\phi} \tag{4.2}$$

where $\boldsymbol{w}$ denotes the test function.

Therefore, the vector of the nodal dof of $\mathbf{G}$ is the solution of the linear system

$$\mathbf{M}_{\mathrm{G}}\,\mathbf{G} = \mathbf{F}_{\mathrm{G}} \tag{4.3}$$

where

$$\mathbf{M}_{\mathrm{G}} = \int_{\Omega} \mathbf{N}^{\phi} \mathbf{N}^{\phi^{\mathrm{T}}} \,\mathrm{d}\Omega, \quad \mathbf{F}_{\mathrm{G}} = \int_{\Omega} \mathbf{N}^{\phi} \nabla \phi \,\mathrm{d}\Omega \tag{4.4}$$

Subsequently, we compute the unit normal for each node i as

$$\mathbf{n}_{\mathrm{int},i} = \frac{\mathbf{G}_i}{\| \mathbf{G}_i \|} \tag{4.5}$$

Similarly, the interfacial curvature can be obtained by the L_2 - projection

$$\int_{\Omega} \boldsymbol{w} \cdot \kappa \,\mathrm{d}\Omega = -\int_{\Omega} \boldsymbol{w} \cdot \left(\nabla \cdot \mathbf{n}_{\mathrm{int}} \right) \mathrm{d}\Omega \quad \forall \boldsymbol{w} \in \mathrm{V}_{\phi} \tag{4.6}$$

For a closed domain Ω, the surface integral can be integrated by parts, and the result involves only the normal to the interface

$$\int_{\Omega} \boldsymbol{w} \cdot \kappa \,\mathrm{d}\Omega = \int_{\Omega} \nabla \boldsymbol{w} \cdot \mathbf{n}_{\mathrm{int}} \,\mathrm{d}\Omega - \int_{\Gamma} \boldsymbol{w} \cdot \mathbf{n}_{\mathrm{int}} \cdot \mathbf{n}_{\Gamma} \,\mathrm{d}\Gamma, \quad \forall \boldsymbol{w} \in \mathrm{V}_{\phi} \tag{4.7}$$

where $\mathbf{n}_{\Gamma}$ denotes the unit normal to the domain boundary Γ.

Denoting by κ the vector of the interfacial curvature at the nodes, one solves the linear system

$$\mathbf{M}_{\mathrm{G}}\, \kappa = \mathbf{F}_{\kappa} \tag{4.8}$$

where

$$\mathbf{F}_{\kappa} = \int_{\Omega} \nabla \mathbf{N}^{\phi} \cdot \mathbf{n}_{\text{int}} \, \mathrm{d}\Omega - \int_{\Gamma} \mathbf{N}^{\phi} \cdot \mathbf{n}_{\text{int}} \cdot \mathbf{n}_{\Gamma} \, \mathrm{d}\Gamma \tag{4.9}$$

Equation (4.7) avoids the direct imposition of derivatives on the normal vector $\mathbf{n}_{\text{int}}$. For an accurate and stable approximation of the gradient and the curvature, it is important that $\phi(\mathbf{x}, t)$ be very close to a signed distance function satisfying the Eikonal equation (1.16):

$$\| \nabla \phi(\mathbf{x}, t) \| = 1$$

Even if ϕ is initially a distance function, it typically ceases to be so with time, due to the deformations induced by the velocity field. One remedy to this problem is to recover relation (1.16) by means of a reinitialization procedure, as described in section 3.5.

4.1.2 Geometric method: Closest point on the interpolated interface

The normal vector can be found using the closest point $\mathbf{c}(\mathbf{x})$ to the interface. The strategy is employed as follows:

First, to obtain an accurate interface representation, the intersected elements are recursively subdivided. Figure 4.1 illustrates the general refinement procedure. Here, four levels of refinement are applied. The approach is quite simple, as the elements from the initial mesh that are cut by the interface are subdivided into four sub-elements of the same type; see Figure 4.1(a). Those sub-elements resulting from the first refinement being cut by the interface are refined a second time, see Figure 4.1(b) and so forth for the next level refinements. Subsequently, the points on the interface with a zero level set in each sub-element are connected with straight segments (cf. Figure 4.1(d)).

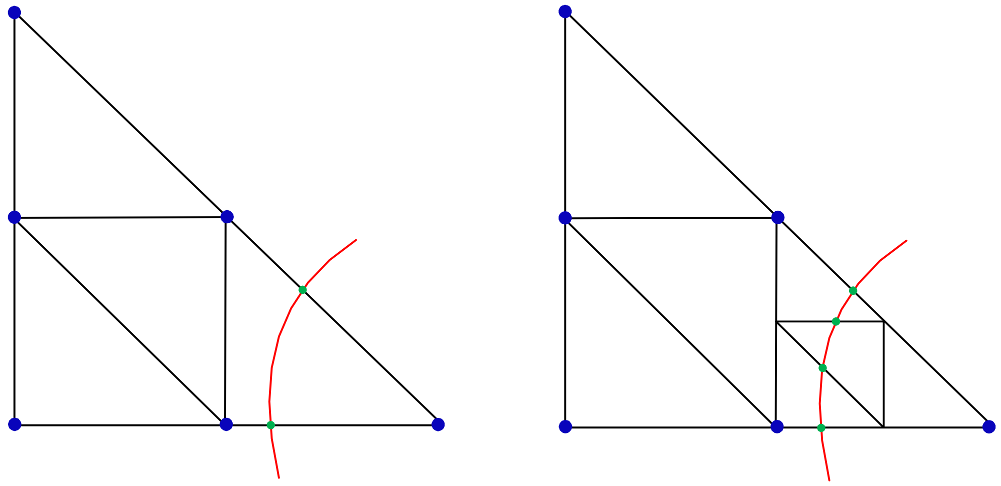

(a) Recursive subdivision of level $n_r = 1$.

(b) Recursive subdivision of level $n_r = 2$.

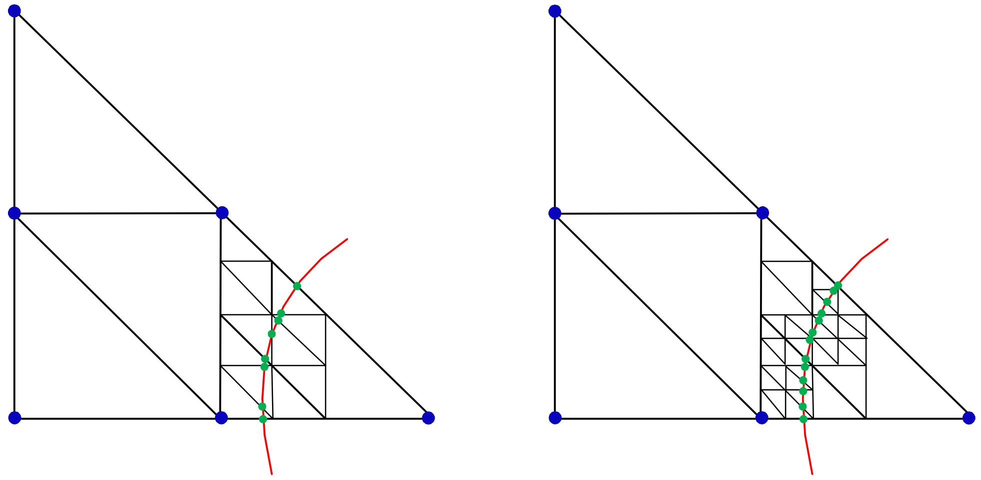

(c) Recursive subdivision of level $n_r = 3$.

(d) Recursive subdivision of level $n_r = 4$.

Figure 4.1 Example of recursive subdivisions of different levels to localize the interface. Red curve depicts the exact interface, and green points depict the iso-zeros level set

The value of the level set function at a point $\mathbf{x}$ can be computed using a usual finite element interpolation:

$$\phi(x) = \sum_{i=1}^{6} N_i(\mathbf{x})\phi_i \tag{4.10}$$

where $\phi_i = \phi(\mathbf{x}_i)$ is the value of the level set function at node i. It is to be noted that the above computations are performed only for elements or sub-elements which are affected by the interface Γ_{int}.

In local coordinate system, the real shape functions for a 6-noded triangle are defined as

$$\begin{aligned}
N_1(\mathbf{x}) &= L_1\left(2L_1 - 1\right) \\
N_2(\mathbf{x}) &= L_2\left(2L_2 - 1\right) \\
N_3(\mathbf{x}) &= L_3\left(2L_3 - 1\right) \\
N_4(\mathbf{x}) &= 4L_1L_2 \\
N_5(\mathbf{x}) &= 4L_3L_2 \\
N_6(\mathbf{x}) &= 4L_3L_1
\end{aligned} \tag{4.11}$$

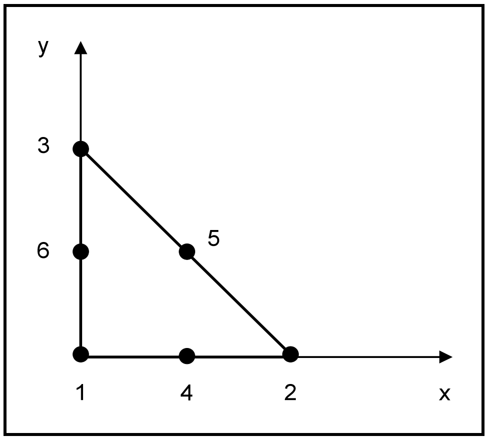

Figure 4.2 A quadratic element

where L_i are the area coordinates

$$L_i = \frac{a_i + b_i\, x + c_i\, y}{2\mathrm{A}} \tag{4.12}$$

The area of the triangle is simply computed as

$$\mathrm{A} = \frac{1}{2}\det\begin{bmatrix} 1 & x_1 & y_1 \\ 1 & x_2 & y_2 \\ 1 & x_3 & y_3 \end{bmatrix} \tag{4.13}$$

and

$$\begin{aligned} a_1 &= x_2 y_3 - x_3 y_2 \qquad & b_1 &= y_2 - y_3 \qquad & c_1 &= x_3 - x_2 \\ a_2 &= x_3 y_1 - x_1 y_3 \qquad & b_2 &= y_3 - y_1 \qquad & c_2 &= x_1 - x_3 \\ a_3 &= x_1 y_2 - x_2 y_1 \qquad & b_3 &= y_1 - y_2 \qquad & c_3 &= x_2 - x_1 \end{aligned}$$

Second, for each grid point in Ω, we calculate the closest point to the approximated interface (see Figure 4.3). The closest point from $\mathbf{x}$ to the interface $\Gamma_{\mathrm{int}}^{\mathrm{h}}$ is defined as

$$\mathbf{c}(\mathbf{x}) = \min_{\mathbf{x}^* \in \Gamma_{\mathrm{int}}^{\mathrm{h}}} \left(\| \mathbf{x} - \mathbf{x}^* \| \right) \tag{4.14}$$

and the collinear unit vector $\mathbf{v}_{col}$ is

$$\mathbf{v}_{col}(\mathbf{x}) = \mathrm{sign}\left(\phi(\mathbf{x})\right) \frac{\mathbf{x} - \mathbf{c}(\mathbf{x})}{\| \mathbf{x} - \mathbf{c}(\mathbf{x}) \|} \tag{4.15}$$

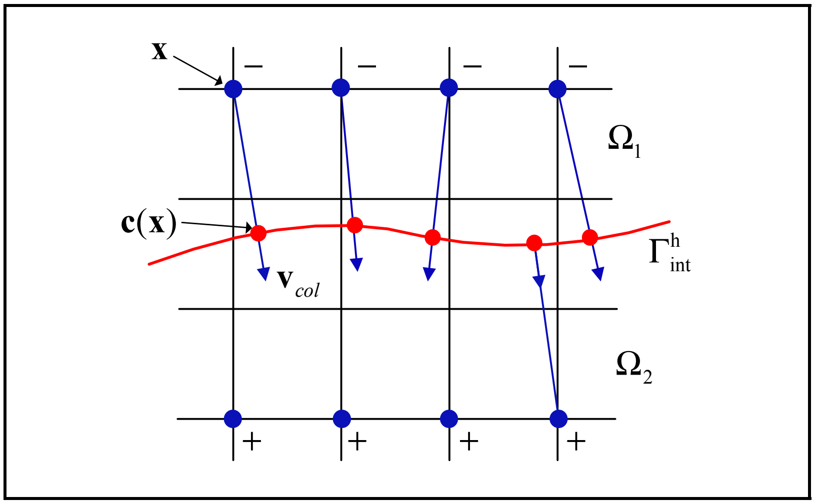

Figure 4.3 Closest point. Blue dots are grid points with their corresponding closest point $\mathbf{c}(\mathbf{x})$ on the interface as red dots. Collinear vectors $\mathbf{v}_{col}(\mathbf{x})$ are drawn from $\overrightarrow{\mathbf{xc}(\mathbf{x})}$. "$+$" and "$-$" indicate the signs of the level set nodal values

In the next step, the tangential unit vectors on the piecewise linear interface are computed by exploiting recursive subdivision (see Figure 4.4).

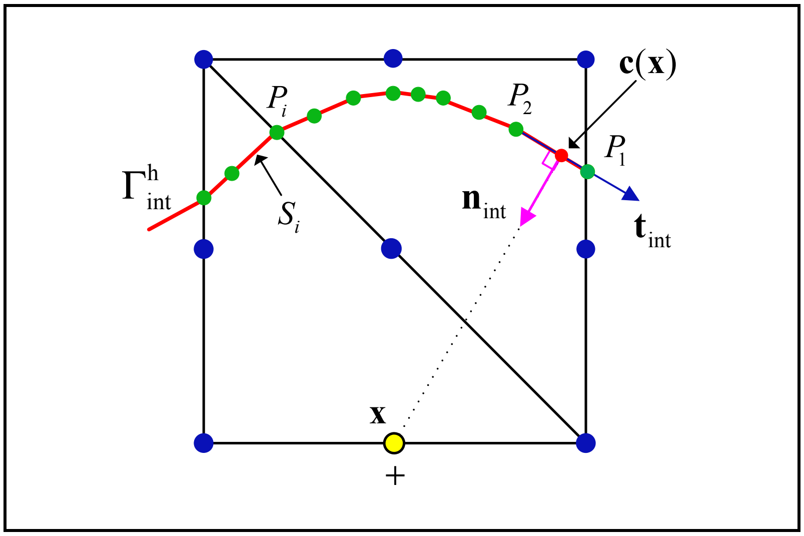

Figure 4.4 Projection of the tangential unit vector $\mathbf{t}_{int}$. The normal unit vector $\mathbf{n}_{int}$ is then computed using (4.17); the segments S_i are in red and the iso-zeros level set P_i are in green

The tangential unit vectors are therefore

$$\mathbf{t}_{\text{int}} = \frac{P_i - P_{i+1}}{\left\| P_i - P_{i+1} \right\|} \tag{4.16}$$

The direction adopted when computing the tangential vectors is inconsequential because the direction of the normal unit vector is to be chosen according to the sign of the collinear unit vector. Recall from section 1.2.1 that the normal unit vector is defined to always points to the domain where $\phi > 0$. The situation is presented in Figure 4.3 and in Figure 4.4.

The normal vectors can now be computed as

$$\mathbf{n}_{\text{int}} = \begin{bmatrix} \text{sign}(v_{col}^{x}) \left| t_{\text{int}}^{y} \right| \\ \text{sign}(v_{col}^{y}) \left| t_{\text{int}}^{x} \right| \end{bmatrix} \tag{4.17}$$

where t_{int}^{x} and t_{int}^{y} are the $x-$ and $y-$components of the tangential unit vector $\mathbf{t}_{\text{int}}$, respectively, and v_{col}^{x} and v_{col}^{y} are the $x-$ and $y-$components of the collinear unit vector $\mathbf{v}_{col}$, respectively.

Subsequently, the curvature is calculated using equation (4.7). The quality of the representation depends on the mesh size (i.e., level of refinement $\mathrm{n_r}$) and on the curve characteristics. Therefore, when the level set is made of non-smooth curves, the level of refinement is very important to obtain a satisfying geometrical representation of the interface. Both the numerical and geometrical errors are reduced as the mesh becomes more refined.

4.2 Comparison: Spatial convergence

First, we compare the accuracy of the normal and curvature approximations with the two methods proposed above.

A stationary disc is considered. The following test case is proposed by Marchandise et al. (Marchandise, Geuzaine et al. 2007). The radius of the disc is $r = 1.0\,\mathrm{m}$ and is positioned at the center of the computational domain Ω that is a square of size $[-2, 2]\times[-2, 2]$ as shown in Figure 4.5. The level set is given by

$$\phi(\mathbf{x}) = \sqrt{x^2 + y^2} - r \tag{4.18}$$

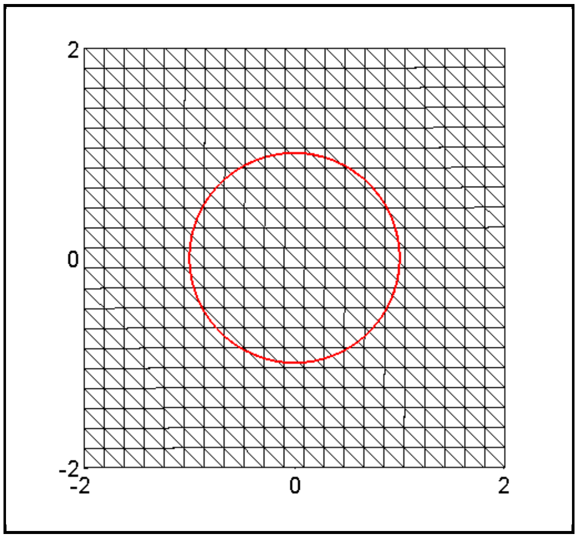

Figure 4.5 Computational domain for the static disc test case

The accuracy is evaluated by computing the $L_2-\mathrm{norm}$ of the error on the normal and curvature fields

$$\begin{aligned} L_{2,\mathbf{n}}(\Omega) &= \frac{\left\| \mathbf{n} - \mathbf{n}^{ex} \right\|_{L_2}}{\left\| \mathbf{n}^{ex} \right\|_{L_2}} \\ &= \frac{\sqrt{\sum_{\Omega^e} \int_{\Omega^e} (n_x - n_x^{ex})^2\, \delta^\varepsilon\, \mathrm{d}\Omega^e + \sum_{\Omega^e} \int_{\Omega^e} (n_y - n_y^{ex})^2\, \delta^\varepsilon\, \mathrm{d}\Omega^e}}{\sqrt{\sum_{\Omega^e} \int_{\Omega^e} n_x^{ex\,2}\, \delta^\varepsilon\, \mathrm{d}\Omega^e + \sum_{\Omega^e} \int_{\Omega^e} n_y^{ex\,2}\, \delta^\varepsilon\, \mathrm{d}\Omega^e}} \end{aligned} \tag{4.19}$$

$$L_{2,\kappa}(\Omega) = \frac{\| \kappa - \kappa_{ex} \|_{L_2}}{\| \kappa_{ex} \|_{L_2}} = \frac{\sqrt{\sum_{\Omega^e} \int_{\Omega^e} (\kappa - \kappa_{ex})^2 \, \delta^{\varepsilon} \, \mathrm{d}\Omega^e}}{\sqrt{\sum_{\Omega^e} \int_{\Omega^e} {\kappa_{ex}}^2 \, \delta^{\varepsilon} \, \mathrm{d}\Omega^e}} \tag{4.20}$$

where n_x and n_x^{ex} (n_y and n_y^{ex}) are the approximated and exact normal in the $x-$direction ($y-$direction), respectively, κ and κ_{ex} are the approximated and exact values of the curvature, Ω^e refers to the element domain, and δ^{ε} is the Dirac delta function. We have

$$n_x^{ex}(\mathbf{x}) = \frac{x}{\sqrt{x^2 + y^2}}, \quad n_y^{ex}(\mathbf{x}) = \frac{y}{\sqrt{x^2 + y^2}} \tag{4.21}$$

and:

$$\kappa_{ex}(\mathbf{x}) = \frac{-1}{\sqrt{x^2 + y^2}} \tag{4.22}$$

$$\delta^{\varepsilon}(\phi) = \begin{cases} 0 & |\phi| > \varepsilon \\ \dfrac{3}{4\varepsilon}\left(1 - (\phi/\varepsilon)^2\right) & |\phi| \leq \varepsilon \end{cases} \tag{4.23}$$

where ε represents the interface thickness, $\varepsilon = 0.5$.

For this example, we have chosen a linear triangular element (T3) and a quadratic triangular element (T6) to approximate the level set function. Figure 4.6 shows the L_2-norm of the error for the normal and curvature fields as a function of the mesh size. A constant refinement level $\mathrm{n_r} = 7$ is employed. The convergence rates (m) indicated in Figure 4.6 are the average slopes of the respective convergence curves.

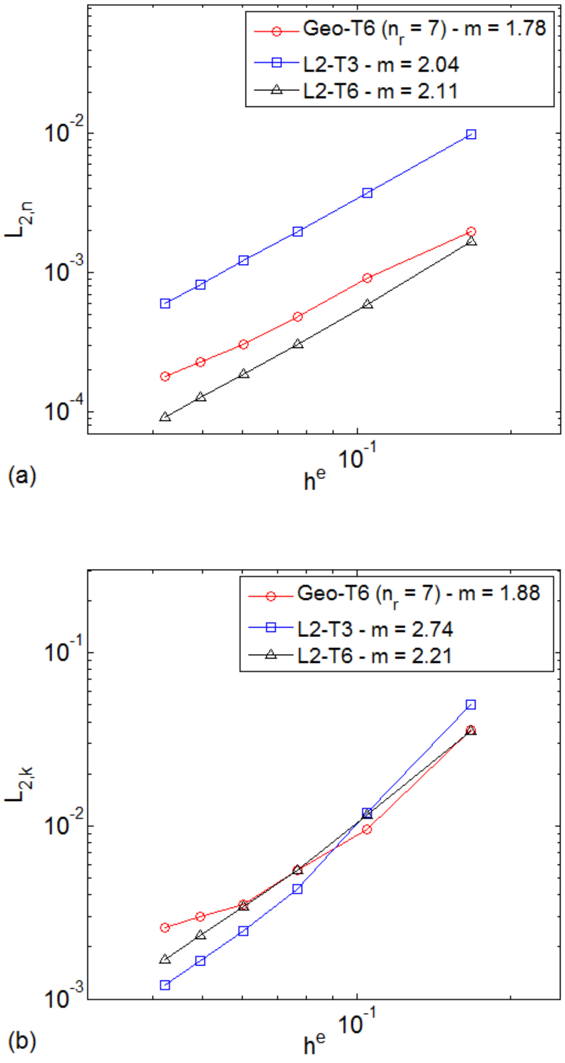

Figure 4.6 Stationary circular bubble: convergence study, L_2 − norm of the error on the normal (a) and curvature (b). We compare the two following methods on structured meshes: The geometrical method ($Geo-\mathrm{T6}$) and the $L2-$projection method using a linear element ($L2-\mathrm{T3}$) and a quadratic element ($L2-\mathrm{T6}$)

From Figure 4.6(a), we observe that the quadratic interpolation $L2-\mathrm{T6}$ leads to better accuracy. However, the convergence rate is only suboptimal at approximately $\mathrm{O}(\mathrm{h}^{2.11})$. On the other hand, using linear interpolation $L2-\mathrm{T3}$, the accuracy is significantly lower, and the normal vectors approximation is on the order $\mathrm{O}(\mathrm{h}^{2.04})$, which compares well with the optimal rate of $\mathrm{O}(\mathrm{h}^{2})$. The $Geo-\mathrm{T6}$ method yields good accuracy.

For the curvature approximation, in Figure 4.6(b), we observe that all three methods lead to approximately the same accuracy. However, the results show that the convergence rate of the $L2-\mathrm{T3}$ method is much faster.

Figure 4.7 compares the convergence study of the $Geo-\mathrm{T6}$ method for different levels of refinement $3 \leq \mathrm{n}_\mathrm{r} \leq 7$. We observe a clear convergence to the exact solutions as the refinement level increases.

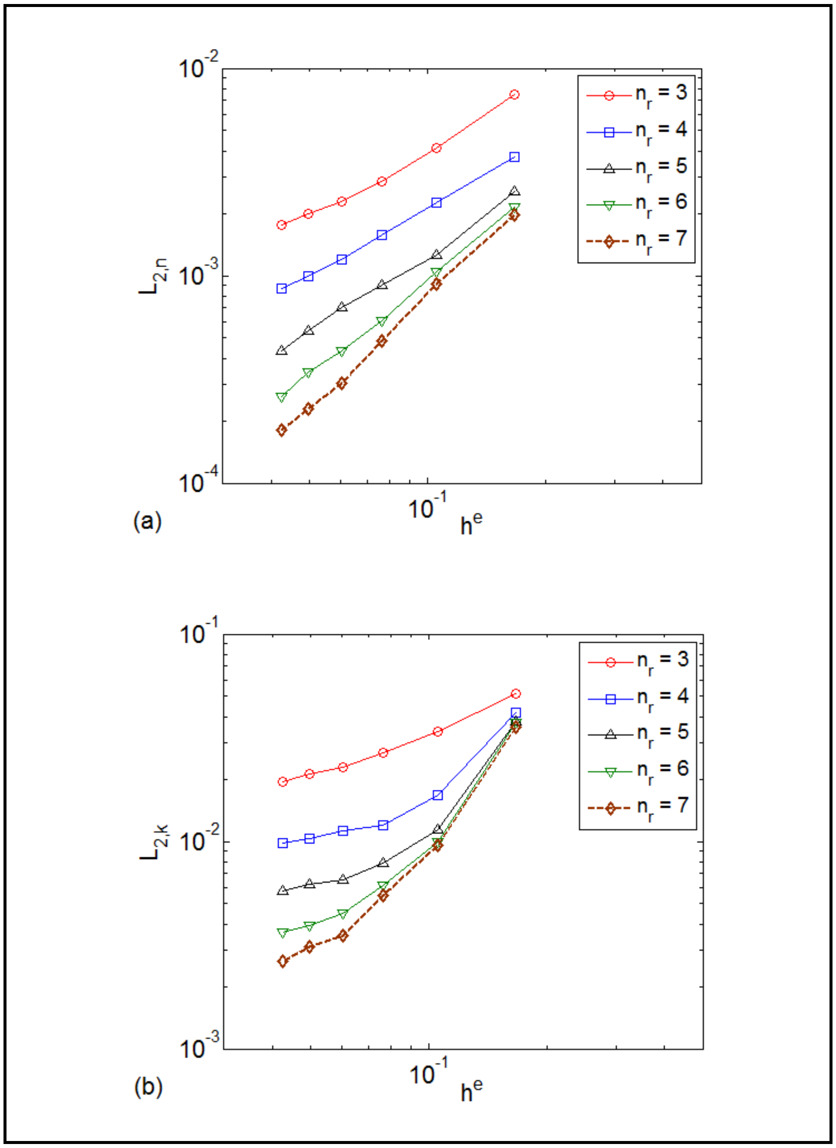

Figure 4.7 Stationary circular bubble: convergence study of the $Geo-\mathrm{T6}$ method for different levels of refinement n_r

4.3 Comparison: Moving interface

To test the robustness of the method in a more general case, we performed the same spatial convergence study when the interface evolves over time. The center of the disc is initially placed at $(-0.50,-0.50)^\mathrm{T}$. The advection is driven by a constant velocity field

$\mathbf{u} = (0.50, 0.50)^{\mathrm{T}}$ so that the disk moves from its initial position to the center of the square in $1.0\ \mathrm{s}$.

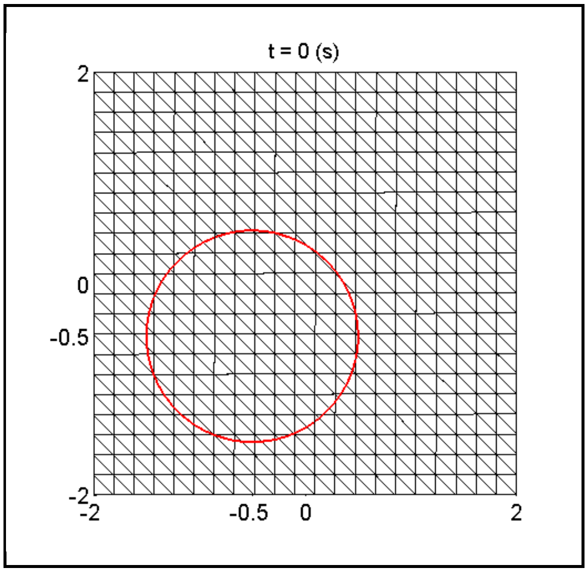

Figure 4.8 Moving circular bubble: initial configuration

Figure 4.9 shows the L_2 – norm of the error for the normal and curvature fields, computed at the final time $t_{end} = 1.0\ \mathrm{s}$, as a function of the mesh size. The time step length is set to $\Delta t = 0.001\ \mathrm{s}$ for all simulations, and the reinitialization procedure (described in Section 3.5) is performed every 25 time steps. A constant refinement level $\mathrm{n}_{\mathrm{r}} = 7$ is maintained.

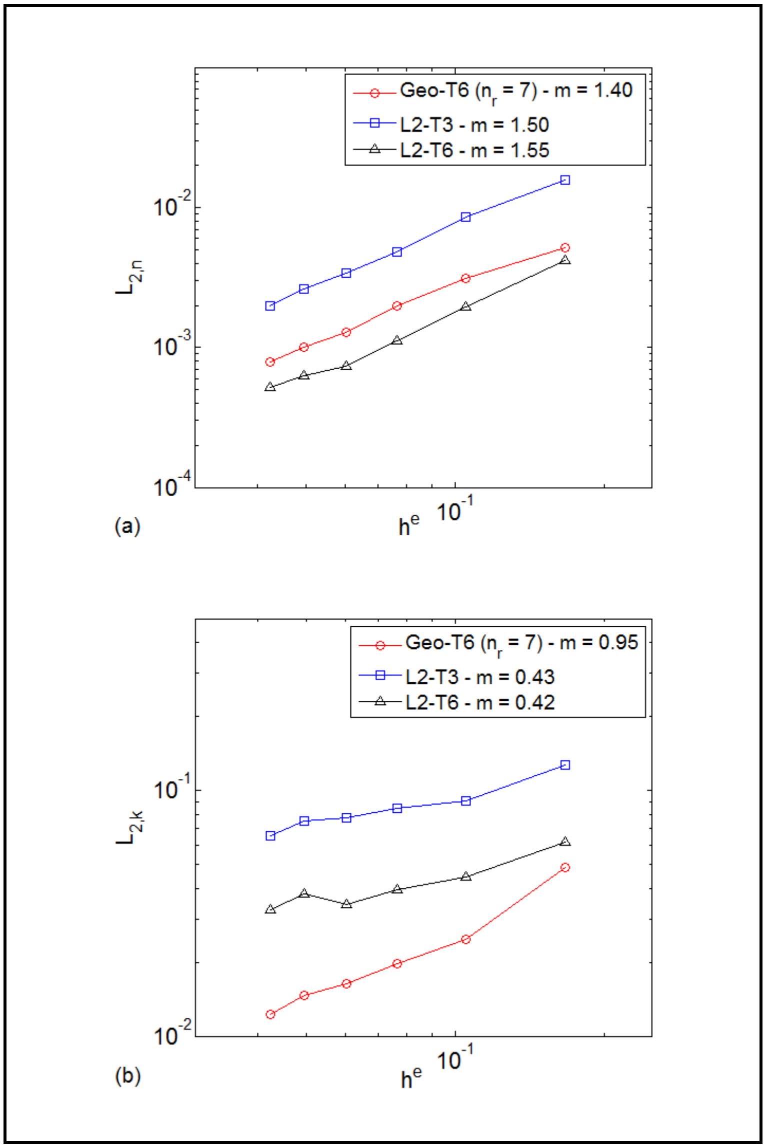

Figure 4.9 Moving circular bubble: convergence study at $t = 1\ \mathrm{s}$, $L_2 -$norm of the error on the normal (a) and curvature (b) and convergence rates (m)

Figure 4.9(a) compares the convergence results on the normal; we can see that the accuracy of all three methods is lower than that obtained from the stationary bubble case. The $L2-\mathrm{T6}$ method still offers a more accurate result than the $Geo-\mathrm{T6}$ method.

From Figure 4.9(b), we clearly see that the $L2-$projection method fails to predict an accurate curvature; our method $Geo-\mathrm{T6}$ leads to a much better accuracy and convergence rate. The above simple demonstration has tremendous implications on the numerical accuracy of the curvature term that is used for the computation of the surface tension force.

From the remarks made in this section, we retain the following rule. In the case of flow problems with moving interfaces, the normal vectors will be computed by means of the geometrical method $Geo-\mathrm{T}6$. Another advantage of using this method is that the normal vectors are naturally perpendicular to the piecewise linear interface. On the other hand, for problems with stationary interfaces, the $L2-$projection method using a quadratic interpolation will be used.

CHAPTER 5

SOLUTION PROCEDURE

In this chapter, the solution procedure will be described. Almost all the necessary ingredients have been presented in previous chapters: governing equations, spatial and temporal discretization, enrichment of the approximation space, sub-cell quadrature and discretization of the surface tension. This is then followed by a discussion on the time-step imposed due to the time scales of the various involved physical phenomena (gravitational force, viscous term, surface tension force, etc.).

5.1 Coupling of Navier-Stokes equations with level set transport equation

The time dependence of the enrichment functions not only complicates the time integration, but it also intervenes and couples the fluid flow with the level set.

In a two-phase fluid flow, a change in fluid velocity affects the position of the interface, which in turn affects the fluid velocity and so on. In general, this type of coupled problem is solved using a segregated approach (Fries and Belytschko 2010). This means that the flow field is calculated with a fixed interface, and then the interface is moved by the computed velocity field. We distinguish two methods: a weak coupling and strong coupling. In a weak coupling, the procedure is carried out only once per time step. In contrast, with a strong coupling, the procedure is repeated until convergence is achieved in both the velocity field and the interface position. Strong coupling between the flow and the interface solvers should offer high accuracy. However, the convergence of the segregated solver is not guaranteed (Carlos, Park et al. 2001), and the required number of iterations may increase significantly. On the other hand, as a small time step size of $10^{-4} \square 10^{-3}\ (\mathrm{s})$ is required for the greater accuracy of the level set, the differences in the solution fields between two successive time levels are sufficiently small. Due to its stability and rapidity, a weak coupling is employed in this work. The flowchart in Figure 5.1 summarizes the solution procedure.

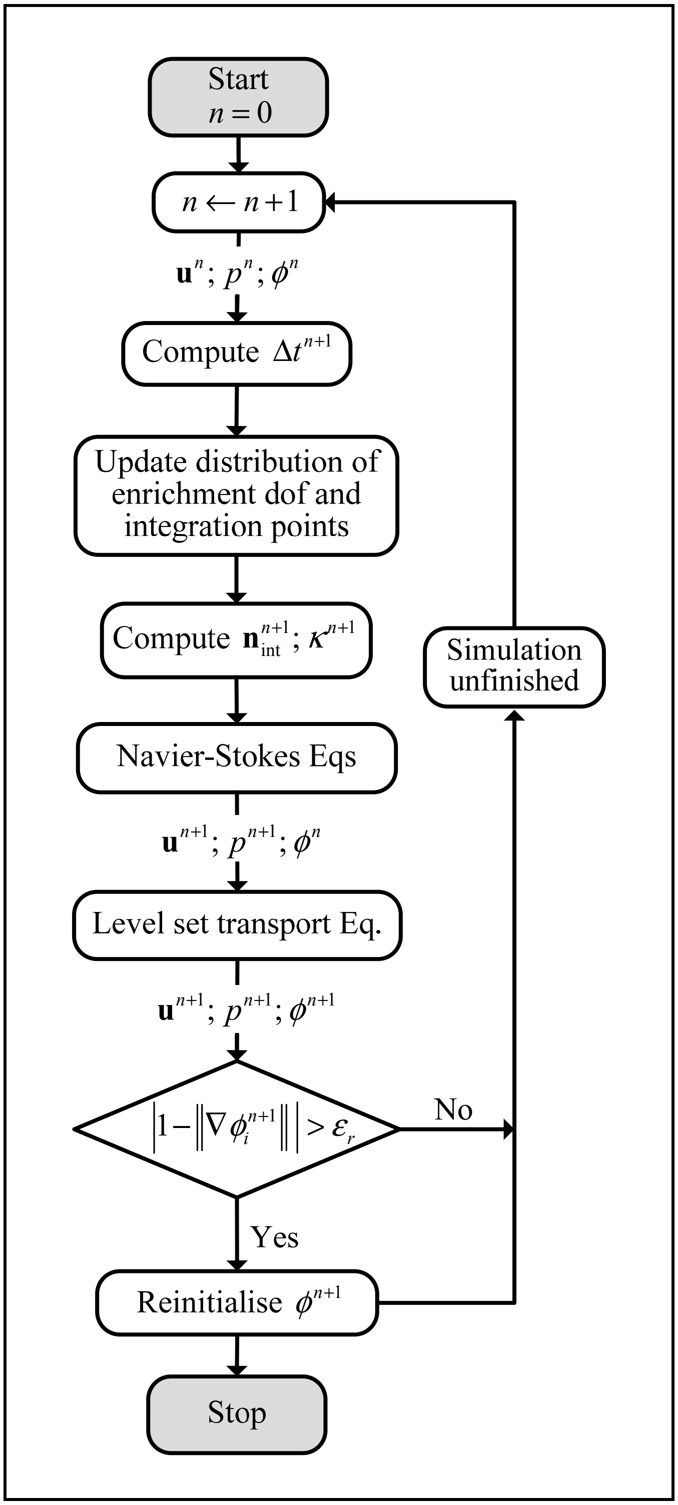

Figure 5.1 Flowchart for weak coupling between Navier-Stokes and level set transport equations

Our experience indicates that the reinitialization procedure of the level set function only has to be performed for long-time two-phase flow simulations. The level set is reinitialized if

$$\max\left(\left|\mathbf{1}-\|\nabla\phi_i\|\right|\right)>\varepsilon_r \tag{5.1}$$

with $\varepsilon_r \in [0.05, 0.10]$.

5.2 Time step size limit

The time step must be controlled to maintain the stability when updating the flow field and the level sets. The time step is obtained based on the CFL number, the gravitational force, the viscous term, and the surface tension force

$$\Delta t_c \le \min_{\Omega}\left(\frac{\mathrm{h}^e}{\|\mathbf{u}\|}\right) \tag{5.2}$$

$$\Delta t_g \le \min_{\Omega}\left(\sqrt{\frac{\mathrm{h}^e}{g}}\right) \tag{5.3}$$

$$\Delta t_v \le \min_{\Omega}\left(\frac{3}{14}\frac{\rho\,\mathrm{h}^{e2}\,\mathrm{Re}}{\mu}\right) \tag{5.4}$$

where the elemental Reynolds number is defined as

$$\mathrm{Re}=\frac{\rho\|\mathbf{u}\|\mathrm{h}^e}{2\mu}$$

According to Brackbill et al. (Brackbill, Kothe et al. 1992), due to the explicit treatment of the surface tension, the time step restriction is given as follows:

$$\Delta t_{st} \le \min_{\Omega}\left(\sqrt{\frac{\rho}{\gamma}}\,\mathrm{h}^{e^{3/2}}\right) \tag{5.5}$$

The time step is then updated as

$$\Delta t^{n+1} = \beta \times \min(\Delta t_c, \Delta t_g, \Delta t_v, \Delta t_{st}) \tag{5.6}$$

where the factor β is a user-defined CFL number.

5.3 The Navier-Stokes/level set coupling algorithm

The coupling between the flow and the level set field is detailed in Algorithm 5-1. Recall that the level set function is used for two reasons: to locate the interface and to construct the enriched functions. Therefore, the same spatial discretization is used for both the flow and the level set fields. Given fluid properties, initial conditions for the flow and level set fields, and boundary conditions the time loop is started. At the beginning of each time step, the flow is first computed (3.6). An update of the distribution of the enriched nodes and elements is realized. This step is followed by a construction of integration cells. And then we solve for the velocity and pressure. The computed velocity field is used to advect the interface to a new position (3.36). Reinitalization of the level-set field is arranged at the end of the time step.

Algorithm 5-1 Coupling algorithm

```
set domain $\Omega$ and generate mesh
initialise flow and level set solvers: $\phi^0, \rho_k, \mu_k, \gamma, \mathbf{g}, \beta$
set $t = 0$ and $n = 0$
set initial values $\mathbf{u}^n = \mathbf{u}^0$, $p^n = p^0$, and $\phi^n = \phi^0$ on $\Omega$
set boundary values for $\mathbf{u}^0$ and $p^0$ on $\Gamma_\mathrm{D}$ and $\Gamma_\mathrm{N}$

time-loop: while $t \le t_\mathrm{end}$

    time step restriction
        compute time step $\Delta t$ according to Section 5.2

    level set solver
        compute $\mathbf{n}_\mathrm{int}(\phi^n)$ and $\boldsymbol{\kappa}(\phi^n)$ according to Section 4.1.2

    level set solver $\rightarrow$ flow solver: transfer $\phi^n, \mathbf{n}_\mathrm{int}(\phi^n), \boldsymbol{\kappa}(\phi^n)$

    flow solver
        update distribution of enriched nodes and elements
        construct XFEM elements sub-divided into cells $\Omega_i^e$ such that $\cup_i \Omega_i^e = \Omega^e$
        and $\cap_i \Omega_i^e = \varnothing$
        define the knot points $\mathbf{x}_j^i$ and weights $\omega_j^i$ of the $Q-$point Gauss
        quadrature in each cell $\Omega_i^e$
        compute surface tension term
        set boundary values for $\mathbf{u}^{n+1}$ and $p^{n+1}$ on $\Gamma_\mathrm{D}$ and $\Gamma_\mathrm{N}$
```

```
23.         solve for $\mathbf{u}^{n+1}$ and $p^{n+1}$ according to Section 3.2
24.
25. flow solver → level set solver: transfer $\mathbf{u}^{n+1}$
26.
27.     **level set solver**
28.         solve for $\phi^{n+1}$ according to section 3.4
29.         compute $\nabla \phi^{n+1}$
30.         if reinitialization: $\left| \mathbf{1} - \left\| \nabla \phi_i^{n+1} \right\| \right| > \varepsilon_r$
31.             reinitialize $\phi^{n+1}$ according to Section 3.5.2
32.         end if
33.
34.     update time step: $t = t + \Delta t^{n+1}$ and $n = n + 1$ and return to step 7
35.
36. end while
```

CHAPTER 6

NUMERICAL TESTS

This chapter presents the numerical tests. We investigate different enrichment schemes of velocity and/or pressure fields with $N_i^{\mathbf{u}*}(\mathbf{x})$ of different orders than $N_i^{\mathbf{u}}(\mathbf{x})$. Whenever possible, we choose test cases where theoretical or numerical solutions are available such that comparisons can be made with our results.

The first part is devoted to problems with a stationary interface. All test cases in this part are calculated using the stationary Navier-Stokes equations. The classical Poiseuille problem is chosen to compare the numerical solutions with the analytical solution. The stability, in the sense of the inf-sup condition, is studied numerically. Next, an extensional flow is considered; the problem exhibits a strong discontinuity in the pressure field because of a jump in the viscosity.

The second part addresses flow problems with a moving interface. First, a simple test case of two immiscible fluids flowing in a tank subjected to a constant horizontal acceleration is studied. At steady state, the interface should remain straight, and the theoretical slope is known. Subsequently, a time-varying acceleration causing water sloshing with large amplitude is considered; this test case helps to verify that the chosen enrichment schemes are capable of simulating unsteady interfaces with large deformations. The validation work is continued for the test case of a dam break over a terrain with or without an obstacle. The last test is a bubble rising in a container fully filled with water; the problem exhibits a weak discontinuity in the velocity field and a strong discontinuity in the pressure field. We compare the two methods of computing the normal vectors (Section 4.1) in this test case.

6.1 Stationary straight interface

6.1.1 Poiseuille two-phase flow

The horizontal stratified flow of two immiscible and incompressible fluids between parallel walls is first considered. The length of the channel is $\mathrm{L}=1.25\ \mathrm{m}$, the height is $\mathrm{H}=0.25\ \mathrm{m}$, and the interface is located at $\mathrm{h}_0=\frac{\mathrm{H}}{2}+\alpha$, where α is set to be 10^{-3} (the parameter α is used to avoid the interface being too close to a node). The gravitational acceleration is $\mathbf{g}=(0,-9.81)^{\mathrm{T}}\ \mathrm{m/s^2}$.

The fluid characteristics are as follows:

- density $\rho_1=1000\ \mathrm{kg/m^3}$, $\rho_2=1\ \mathrm{kg/m^3}$; and
- dynamic viscosity $\mu_1=1\ \mathrm{kg/(m.s)}$, $\mu_2=0.10\ \mathrm{kg/(m.s)}$.

Surface tension is not included in this test case, that is, weak discontinuities in the velocity and pressure fields occur across the interface.

The long-time solution will converge to the steady state solution, which can be described by an analytical solution (6.3).

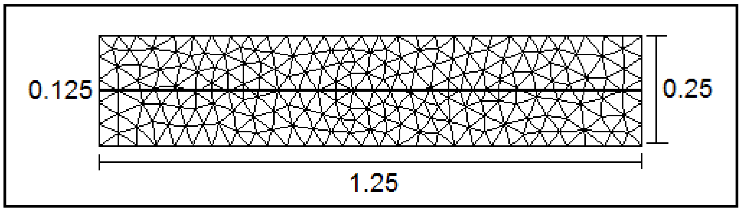

Figure 6.1 Two-phase Poiseuille: computational domain and mesh, with $\mathrm{h}^e=0.05$

The pressures are imposed on the right and left limits of the calculation domain to ensure a pressure difference $\Delta p = -10^3\ \mathrm{Pa}$. The velocity is set to zero at the top and bottom boundaries:

$$\mathbf{u}(x, y = 0) = \mathbf{u}(x, y = \mathrm{H}) = 0 \tag{6.1}$$

and the vertical velocity component υ is zero at the inlet and outlet boundaries for all degrees of freedom (i.e., the enrichment dofs are also set to zero):

$$\upsilon(x = 0, y) = \upsilon(x = \mathrm{L}, y) = 0 \tag{6.2}$$

The analytical solution assuming fully developed flow is

$$u_{ex}(x, y) = \begin{cases} \dfrac{\Delta p}{2\mu_1 \mathrm{L}} y^2 + \dfrac{c_1}{\mu_1} y & \text{if } 0 \leq y \leq \mathrm{h} \\ \dfrac{\Delta p}{2\mu_2 \mathrm{L}} y^2 + \dfrac{c_1}{\mu_2} y + c_2 & \text{if } \mathrm{h} < y \leq \mathrm{H} \end{cases} \tag{6.3}$$

and

$$\upsilon_{ex}(x, y) = \ 0 \tag{6.4}$$

where

$$\begin{aligned} c_1 &= \frac{\Delta p}{2\mathrm{L}} \frac{(\mu_1 - \mu_2)\mathrm{h}_0{}^2 - \mu_1 \mathrm{H}^2}{\mu_2 \mathrm{h}_0 - \mu_1 (\mathrm{h}_0 - \mathrm{H})}; \\ c_2 &= -\frac{\Delta p}{2\mu_2 \mathrm{L}} \mathrm{H}^2 - \frac{c_1}{\mu_2} \mathrm{H}. \end{aligned} \tag{6.5}$$

The errors between the analytical and numerical solutions are measured using the normalized L_2 – norm defined as

$$L_{2,\mathbf{u}}(\Omega)=\frac{\left\|\mathbf{u}-\mathbf{u}_{ex}\right\|_{L_2}}{\left\|\mathbf{u}_{ex}\right\|_{L_2}}=\frac{\sqrt{\sum_{\Omega^e}\int_{\Omega^e}(u-u_{ex})^2\,\mathrm{d}\Omega^e+\sum_{\Omega^e}\int_{\Omega^e}(\upsilon-\upsilon_{ex})^2\,\mathrm{d}\Omega^e}}{\sqrt{\sum_{\Omega^e}\int_{\Omega^e}u_{ex}^2\,\mathrm{d}\Omega^e+\sum_{\Omega^e}\int_{\Omega^e}\upsilon_{ex}^2\,\mathrm{d}\Omega^e}} \qquad (6.6)$$

where u and u_{ex} (υ and υ_{ex}) are the approximated and exact velocities in the x -direction (y -direction), respectively, and Ω^e refers to the element domain.

It seems natural to use the ridge enrichment (2.11) for the velocity, and sign-enrichment (2.4) or the ridge-enrichment for the pressure. We use the following abbreviations:

Table 6-1 XFEM approximations and their abbreviations

case		**velocity**	**pressure**	$N_i^{\mathbf{u}*}$	$\psi^{\mathbf{u}}$	N_i^{p*}	ψ^{p}
1	$\emptyset - \mathrm{P}_1$ enrich.	none	$\mathrm{P}_1\times\mathrm{R}$	$\emptyset$	-	P_1	ψ_R
2		none	$\mathrm{P}_1\times\mathrm{sign}$	$\emptyset$	-	P_1	ψ_{sign}
3	$\mathrm{P}_1 - \mathrm{P}_1$ enrich.	$\mathrm{P}_1\times\mathrm{R}$	$\mathrm{P}_1\times\mathrm{R}$	P_1	ψ_R	P_1	ψ_R
4		$\mathrm{P}_1\times\mathrm{R}$	$\mathrm{P}_1\times\mathrm{sign}$	P_1	ψ_R	P_1	ψ_{sign}
5	$\mathrm{P}_2 - \mathrm{P}_1$ enrich.	$\mathrm{P}_2\times\mathrm{R}$	$\mathrm{P}_1\times\mathrm{R}$	P_2	ψ_R	P_1	ψ_R
6		$\mathrm{P}_2\times\mathrm{R}$	$\mathrm{P}_1\times\mathrm{sign}$	P_2	ψ_R	P_1	ψ_{sign}

The comparison between the numerical and analytical velocity field is presented in Figure 6.2. The solutions have been computed for the unstructured mesh shown in Figure 6.1. We can clearly observe a parabolic profile for each subdomain.

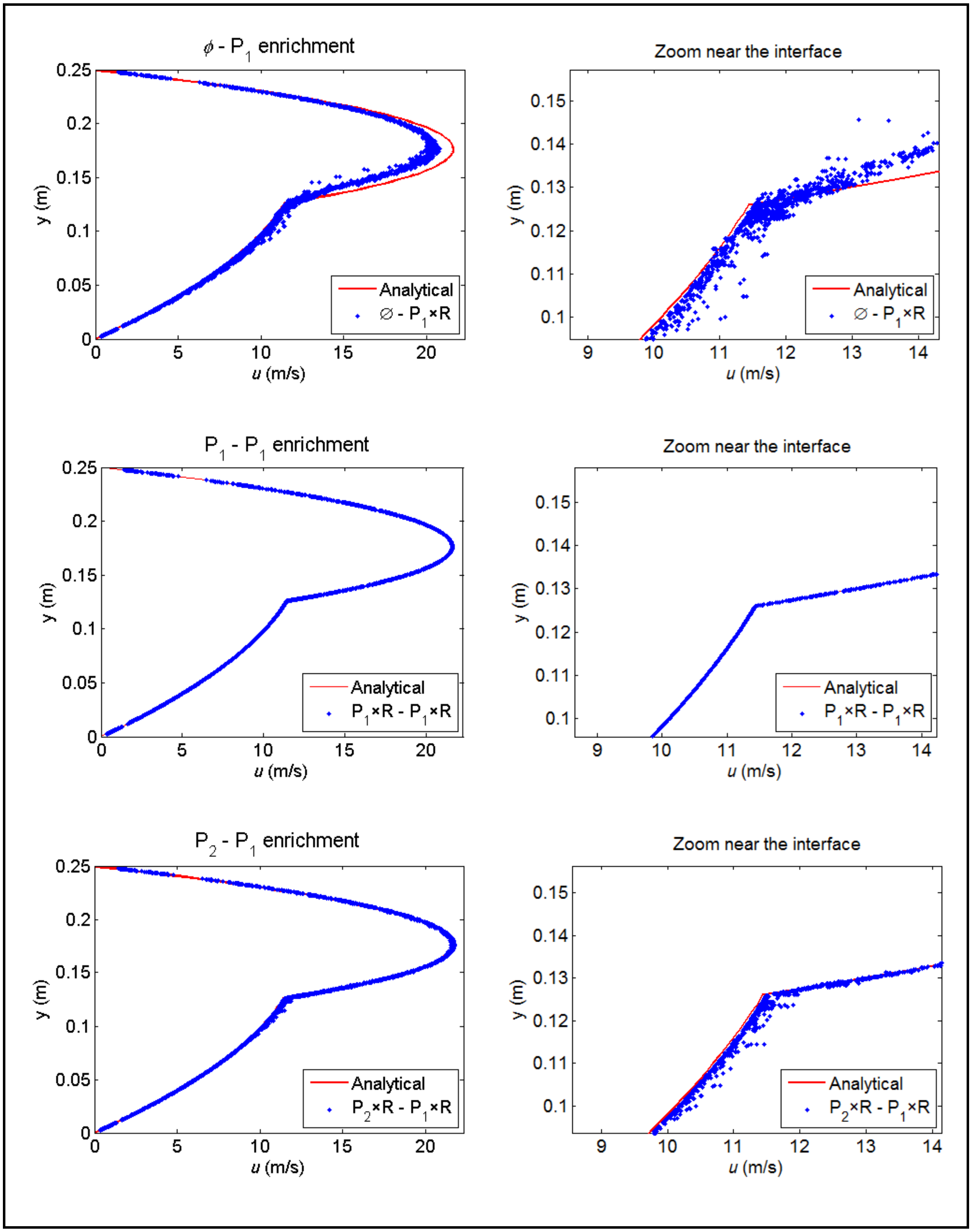

Figure 6.2 Two-phase Poiseuille: the $P_1 - P_1$ enrichment performs better than the $\emptyset - P_1$ and $P_2 - P_1$ enrichments. The horizontal velocity is evaluated at the Gauss points of each element

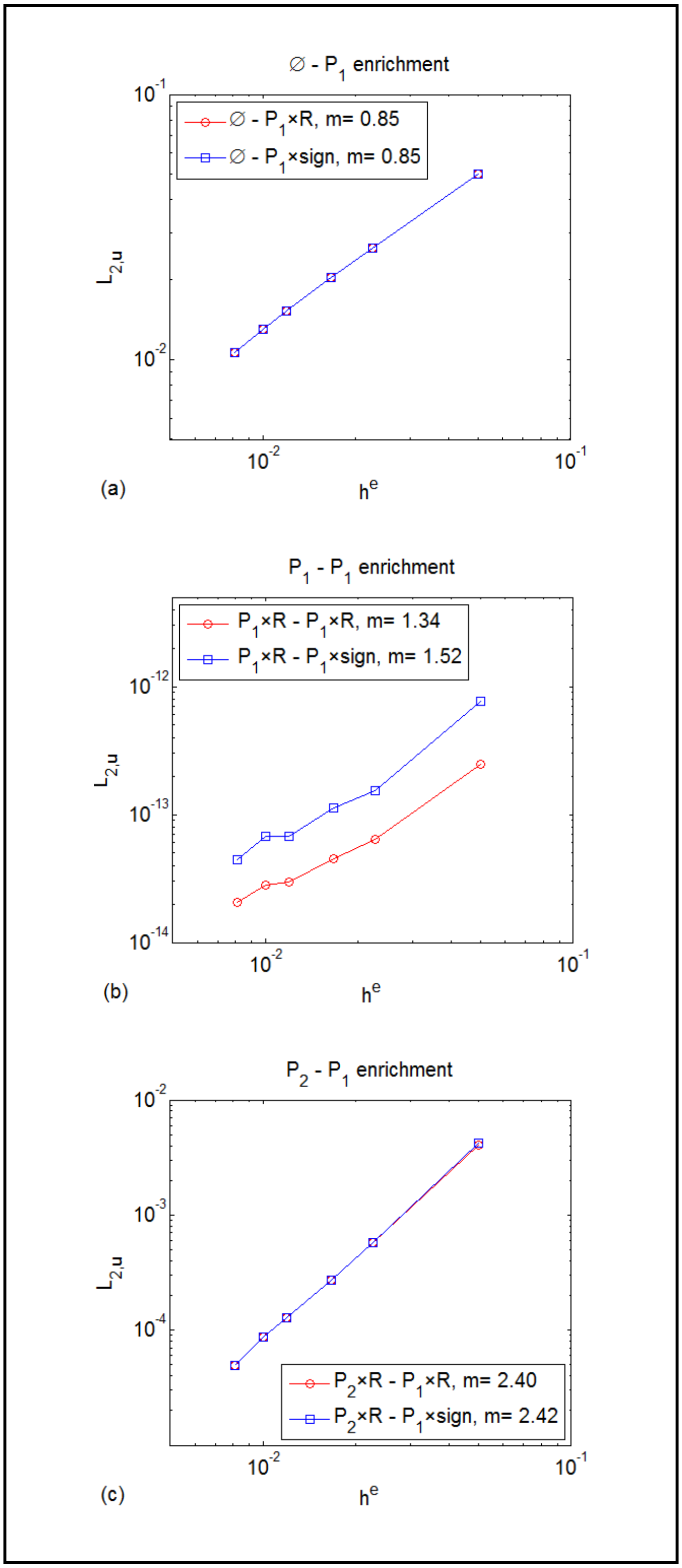

Figure 6.3 Two-phase Poiseuille: convergence study for the different enrichment schemes

Figure 6.3 compares the convergence results between different enrichment schemes. The horizontal axis refers to the element size, and the vertical axis refers to the $L_2-\mathrm{norm}$ of the error. A sequence of unstructured meshes was generated, with mesh sizes of 1/N where $\mathrm{N}=\{20, 40, 60, 80, 100, 124\}$. The convergence rates (m) indicated in Figure 6.3 are the average slopes (m).

In the case where the velocity field is not enriched (i.e., $\emptyset-\mathrm{P}_1$ enrichment), there is high error and poor convergence $\mathrm{O}(\mathrm{h}^1)$, as shown in Figure 6.3(a). The enrichment of the pressure field does not improve the convergence rate of the velocity error. This result can be explained by the fact that the interface conditions are not respected.

The interface condition for the normal stress (1.12) can be rewritten as

$$\left\llbracket -p\,\mathbf{I}+\mu\left(\nabla\mathbf{u}+(\nabla\mathbf{u})^{\mathrm{T}}\right)\right\rrbracket\cdot\mathbf{n}_{\mathrm{int}}=\gamma\kappa\mathbf{n}_{\mathrm{int}},\quad \forall\mathbf{x}\in\Gamma_{\mathrm{int}} \tag{6.7}$$

The influence of the surface tension is neglected in this test case.

$$\begin{aligned}
&\Leftrightarrow \left\llbracket -p\,\mathbf{I}+\mu\left(\nabla\mathbf{u}+(\nabla\mathbf{u})^{\mathrm{T}}\right)\right\rrbracket\cdot\mathbf{n}_{\mathrm{int}}=0\\
&\Rightarrow \mathbf{n}_{\mathrm{int}}^{\mathrm{T}}\cdot\left\llbracket -p\,\mathbf{I}+\mu\left(\nabla\mathbf{u}+(\nabla\mathbf{u})^{\mathrm{T}}\right)\right\rrbracket\cdot\mathbf{n}_{\mathrm{int}}=0\\
&\Rightarrow -\llbracket p\rrbracket+\llbracket 2\mu(\nabla\mathbf{u}\cdot\mathbf{n}_{\mathrm{int}})\cdot\mathbf{n}_{\mathrm{int}}\rrbracket=0\\
&\Rightarrow -\llbracket p\rrbracket+2\left\llbracket \mu\frac{\partial u_n}{\partial n_{\mathrm{int}}}\right\rrbracket=0
\end{aligned} \tag{6.8}$$

where $u_n=\mathbf{u}\cdot\mathbf{n}_{\mathrm{int}}$ is the normal component of the velocity at the interface.

From Eq. (6.8) we should have $\left\llbracket \mu\frac{\partial u_n}{\partial n_{\mathrm{int}}}\right\rrbracket=0$ and $\llbracket p\rrbracket=0$. The first condition cannot be satisfied since we have $\left\llbracket \frac{\partial u_n}{\partial n_{\mathrm{int}}}\right\rrbracket=0$ and $\llbracket \mu\rrbracket\neq 0$, leads to

$$-\llbracket p \rrbracket + 2\left\llbracket \mu \frac{\partial u_n}{\partial n_{\text{int}}} \right\rrbracket \neq 0, \quad \forall \mathbf{x} \in \Gamma_{\text{int}} \tag{6.9}$$

This error can be decreased by refining the mesh in the vicinity of the interface.

On the other hand, using first-order $N_i^*(\mathbf{x})$ (i.e., $\mathrm{P}_1 - \mathrm{P}_1$ enrichment, first-order $N_i^{\mathbf{u}*}(\mathbf{x})$ and $N_i^{p*}(\mathbf{x})$) leads to the (nearly) exact solution, as shown in Figure 6.3(b), with the L_2-norm on the order of 10^{-13}.

For the functions $N_i^{\mathbf{u}*}(\mathbf{x})$ and $N_i^{p*}(\mathbf{x})$ of the same order as the FEM shape functions $N_i^{\mathbf{u}}(\mathbf{x})$ and $N_i^{p}(\mathbf{x})$, respectively, (i.e., $\mathrm{P}_2 - \mathrm{P}_1$ enrichment, Figure 6.3(c)), we observe a convergence order of $\mathrm{O(h^{5/2})}$, which is suboptimal to the supposedly optimal convergence order $\mathrm{O(h^3)}$ for the velocity.

An important observation can be made that both the convergence rate and accuracy are affected significantly when the order of $N_i^{\mathbf{u}*}(\mathbf{x}) \cdot [\psi(\mathbf{x},t) - \psi(\mathbf{x}_i,t)]$ in the enrichment part is higher than the order of $N_i^{\mathbf{u}}(\mathbf{x})$; indeed, this is one condition for the XFEM convergence. Furthermore, to satisfy the velocity continuity as required by the Galerkin formulation, a continuous $\psi(\mathbf{x},t)$ must be used, such as the Ridge enrichment, and therefore $N_i^{\mathbf{u}*}(\mathbf{x})$ should be of order 1.

This convergence study was a first step to evaluate the different enrichment strategies for stationary interfaces. The verification of the inf-sup condition is another aspect in the validation. The inf-sup β_h is approximated for the Poiseuille problem using gradually refined unstructured triangular meshes. The evolution β_h value is plotted in Figure 6.4.

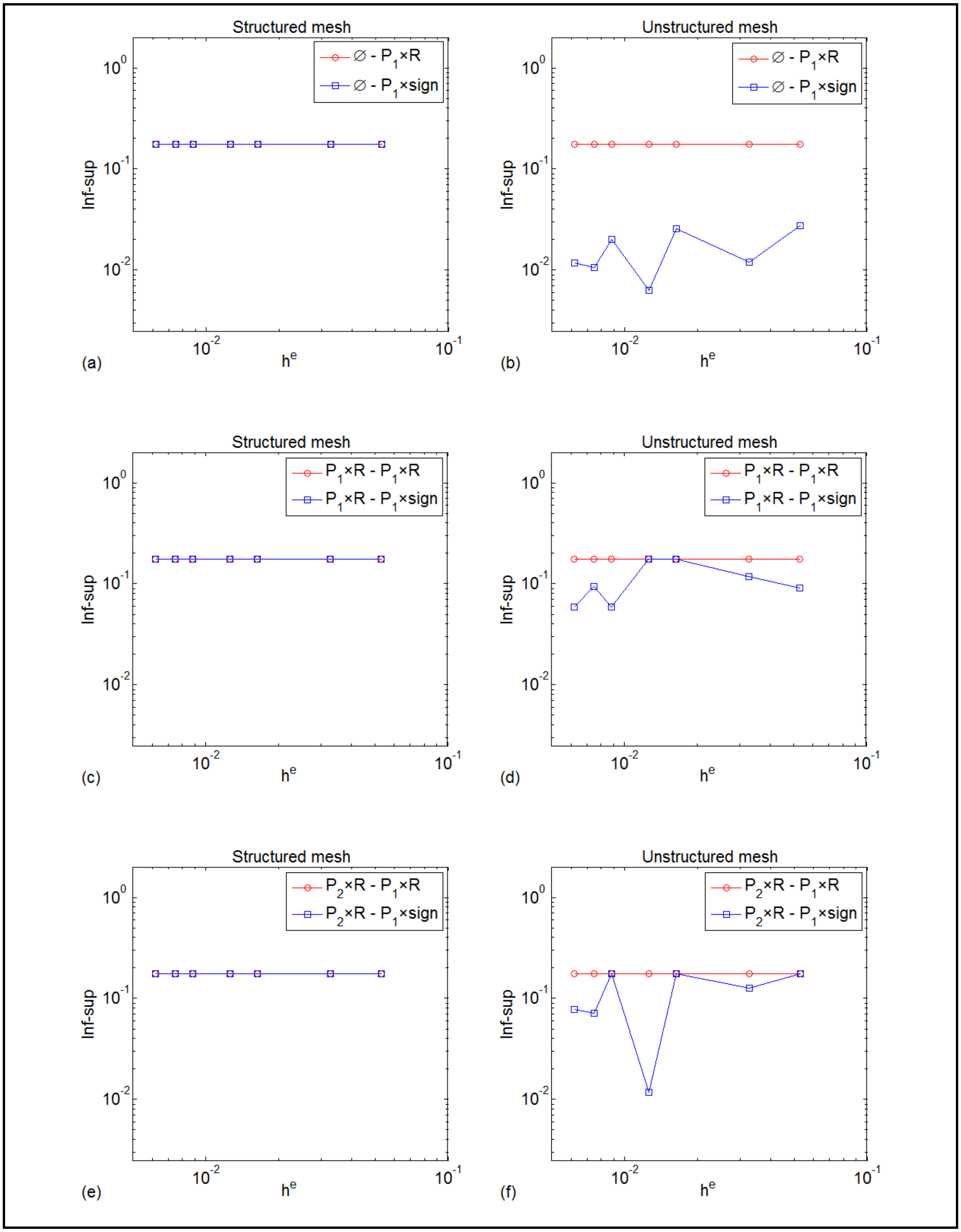

Figure 6.4 Two-phase Poiseuille: evolution of the numerical inf-sup β_h

For a structured mesh, the inf-sup values are constant for all enrichments (cf. Figure 6.4 (a), (c), and (e)). This indicates that these enrichments pass the inf-sup test (equation (3.46)) and are predicted to be stable.

In contrast, for an unstructured mesh, Figure 6.4 (b), (d), and (f) show that as the mesh is made finer, the inf-sup values corresponding to all $p\times\text{sign}$ enrichments vary significantly. This trend indicates that the enrichments do not pass the inf-sup test. We believe that this comes from an ill-conditioned system.

To allow for a clear comparison, we analyze the effect of an ill-conditioned system on the accuracy of the different enrichment schemes in the following study. We discretize the domain with a structured 16×80 mesh ($\text{h}^e \approx 0.0156$) to easily change the position of the interface across elements, as depicted in Figure 6.5. An ill-conditioned system will occur when the interface Γ_{int} is approximately aligned with a node or an element edge. The interface position is varied from $\delta = 10^{-4}$ to $\delta = 10^{-7}$.

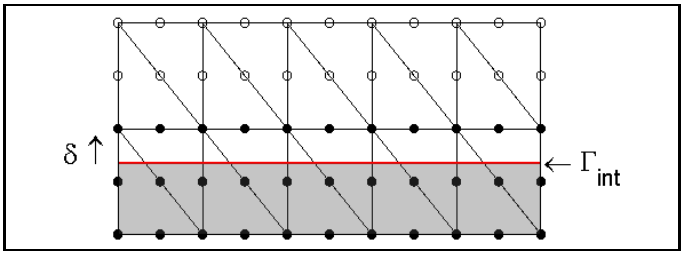

Figure 6.5 Position of the interface across elements

The variation of the minimum element area ratio $\text{A}_{\min}$ with δ is shown Figure 6.6.

$$\text{A}_{\min} = \min_{e\in I^*}\left(\text{A}^e_{\Omega_1} / \text{A}^e_{\Omega_2}\right) \tag{6.10}$$

where I^* is the set of intersected elements. The minimum area ratio is on the order of 10^{-4} to 10^{-10}.

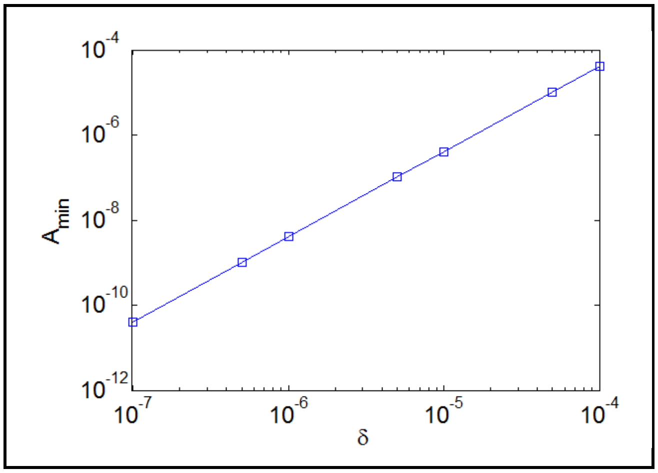

Figure 6.6 Minimum element area ratio A_{min}

The criterion in equation (3.32) is not applied when constructing the system matrices. The values of the $L_2-\text{norm}$ error on the velocity field are shown in Figure 6.7 as the interface position δ varies.

As seen from Figure 6.7, if the pressure is enriched with the sign-enrichment, the $L_{2,\mathbf{u}}$ value increases drastically as the ratio of the intersected areas decreases, and the accuracy is significantly affected. In contrast, for the Ridge-enrichment, we observe that $L_{2,\mathbf{u}}$ remains approximately constant, which indicates very little effect on the accuracy. This is particularly advantageous for iterative solvers and/or nonlinear problems.

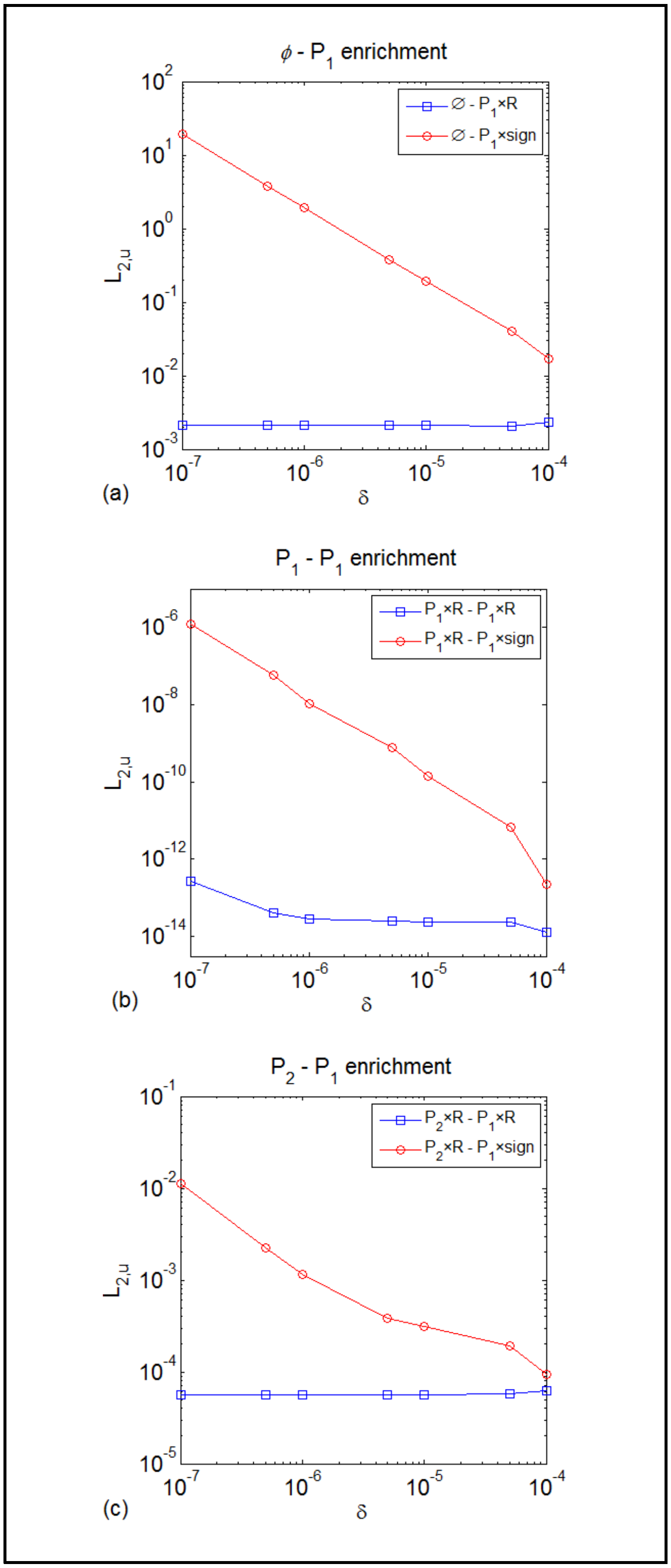

Figure 6.7 Two-phase Poiseuille: influence of an ill-conditioned system

6.1.2 Extensional flow problem

The following test case is proposed by Ausas et al. (Ausas, Buscaglia et al. 2012). We consider two fluids in a unit square domain with viscosities $\mu_1 = 5\ \mathrm{kg/(m.s)}$ and $\mu_2 = 1\ \mathrm{kg/(m.s)}$, separated by a straight horizontal interface at $\mathrm{h}_0 = 0.5\ \mathrm{m}$ (cf. Figure 6.8). The density ρ is equal to $10\ \mathrm{kg/m^3}$ for both fluids. Neglecting the gravity and the influence of the surface tension and imposing the linear velocity field

$$\mathbf{u}(\mathbf{x}) = \begin{pmatrix} 1-x \\ y \end{pmatrix} \tag{6.11}$$

the pressure field has a jump across the interface because of a jump in the viscosity.

$$p(\mathbf{x}) = \begin{cases} \rho\left(x - \tfrac{1}{2}(x^2+y^2)\right) + 2(\mu_1 - \mu_2) & \text{if } y < \mathrm{h}_0 \\ \rho\left(x - \tfrac{1}{2}(x^2+y^2)\right) & \text{if } y \geq \mathrm{h}_0 \end{cases} \tag{6.12}$$

The pressure is imposed null at the point $(1,1)^{\mathrm{T}}$.

A sequence of unstructured meshes was generated; the first one is presented in Figure 6.8. We compute the pressure error in the $L_2 -$norm as a function of h^e for two enrichment schemes. The results of the convergence study are shown in Figure 6.9.

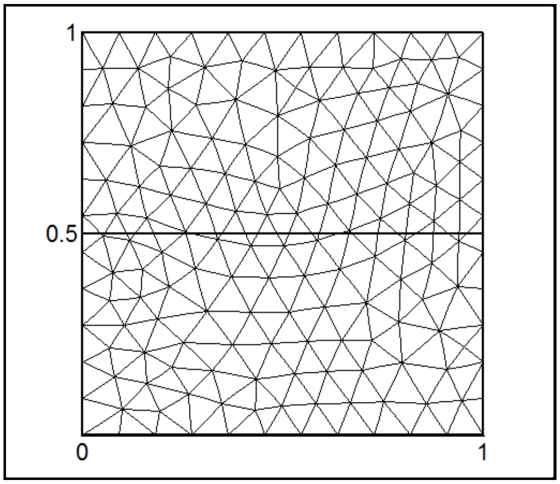

Figure 6.8 Extensional flow problem: computational mesh, with $h^e = 0.091$

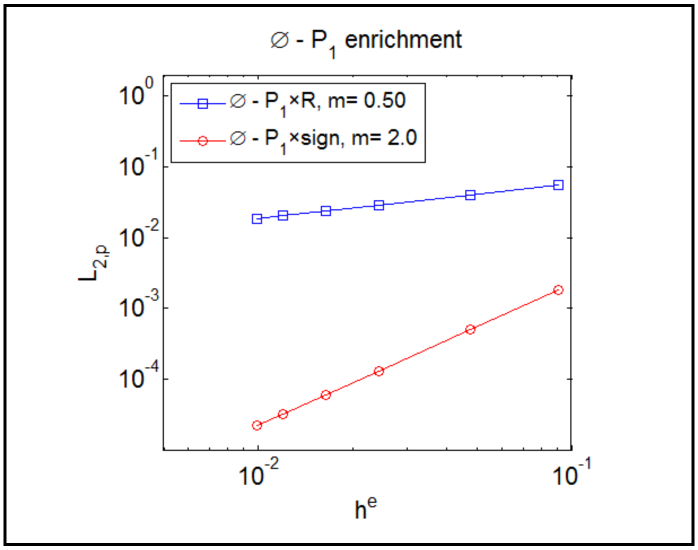

Figure 6.9 Extensional flow problem with jump in the viscosity: convergence study, L_2 – norm of the error in the pressure field and convergence rates (m)

Figure 6.9 compares the convergence results between the Ridge-enrichment and the sign-enrichment. We observe that using the Ridge-enrichment leads to a poor convergence rate of $O(h^{1/2})$ and produces higher pressure errors due to the jump in the pressure field. In contrast, using the sign-enrichment leads to the optimal convergence rate of $O(h^2)$ and to a much better accuracy.

Figure 6.10 shows the pressure fields for the sign function (top) and the ridge function (bottom).

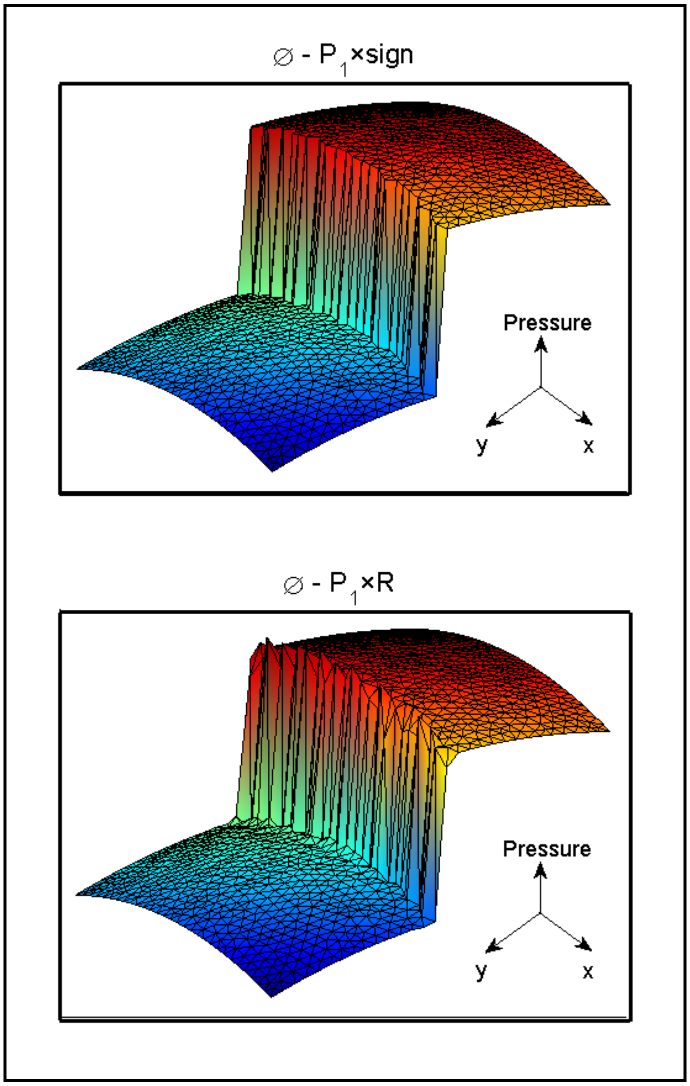

Figure 6.10 Extensional flow problem with jump in the viscosity: pressure field

Note that the case without inertial effects (i.e., $\rho_1 = \rho_2 = 0$) corresponds to a constant pressure field on each fluid, with a jump at the interface of magnitude $2(\mu_1 - \mu_2)$.

The views of these pressure fields at $x = 0.5$ are compared in Figure 6.11, in which we can clearly observe the improved behavior near the interface when the sign-enrichment is used.

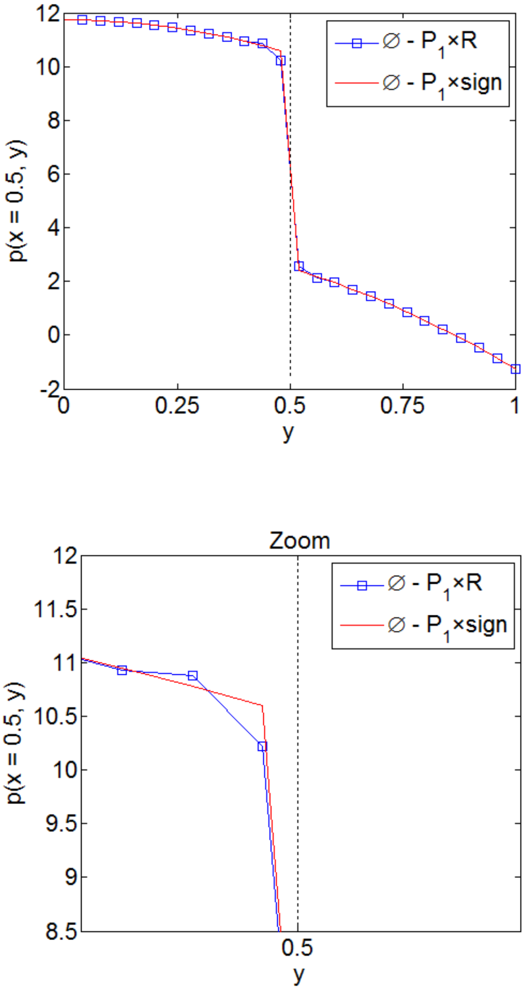

Figure 6.11 Extensional flow problem with jump in the viscosity: comparison of the pressure field section at $x = 0.5$

If a discontinuous volume force is introduced,

$$g_x = 0;$$
$$g_y = \begin{cases} -10 & \text{if } y < \mathrm{h}_0 \\ 0 & \text{if } y \geq \mathrm{h}_0 \end{cases} \tag{6.13}$$

the analytical solution for the pressure field is given by:

$$p(x, y) = \begin{cases} \rho\left(x - \frac{1}{2}(x^2 + y^2) - g_y(\mathrm{h}_0 - \mathrm{y})\right) + 2(\mu_1 - \mu_2) & \text{if } y < \mathrm{h}_0 \\ \rho\left(x - \frac{1}{2}(x^2 + y^2)\right) & \text{if } y \geq \mathrm{h}_0 \end{cases} \tag{6.14}$$

in which there is a jump in the pressure of size $2(\mu_1 - \mu_2)$ and a jump in the pressure gradient of size $\rho|g_y|$. The boundary conditions and interface position are the same as in the previous case. Figure 6.12 shows the $L_2 - \text{norm}$ of the error in the pressure field for different meshes, and Figure 6.13 indicates the pressure fields for the sign function (left) and the ridge function (right).

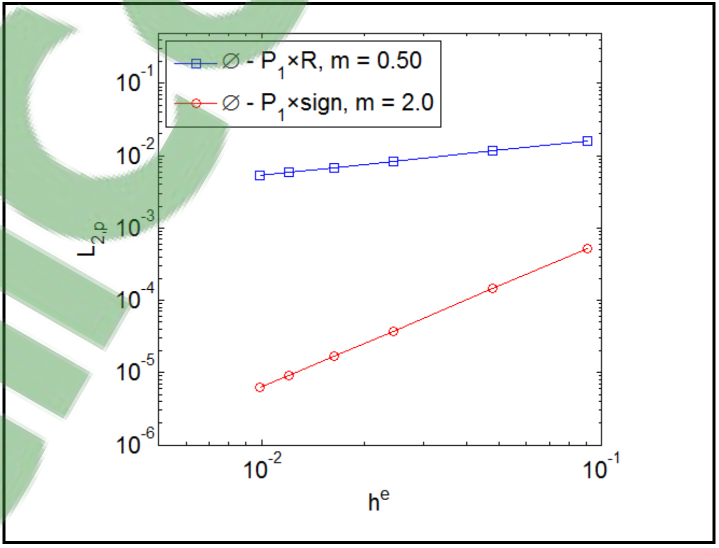

Figure 6.12 Extensional flow problem with jump in the viscosity and discontinuous volume force: convergence study, $L_2 - \text{norm}$ of the error in the pressure field

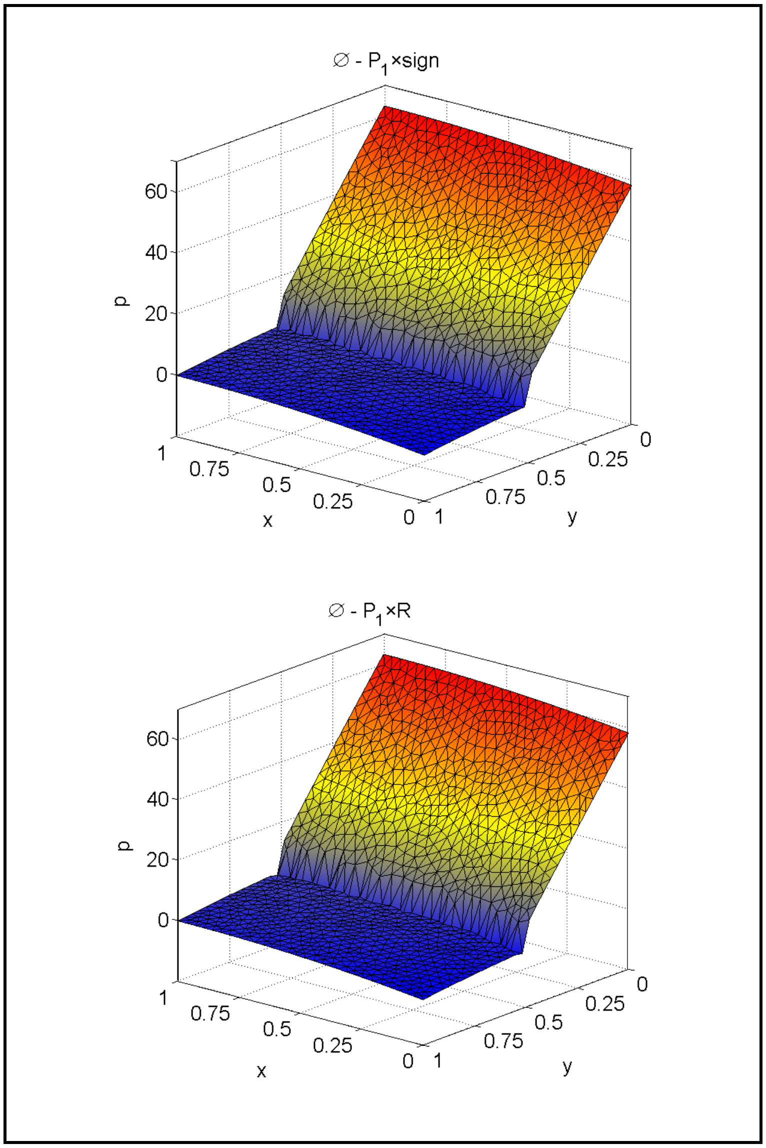

Figure 6.13 Extensional flow problem with jump in the viscosity and discontinuous volume force: pressure fields for the sign function (left) and the ridge function (right)

The sign-enrichment still achieves an optimal convergence rate of $O(h^2)$ and an optimal accuracy.

6.2 Numerical examples: A moving interface

In this section, we extend the comparison of different XFEM enrichments to cases of unsteady flows with moving interfaces.

For all test cases in this section, the reinitialization procedure is performed using a constant refinement level of $\mathrm{n_r} = 4$.

6.2.1 Rectangular tank under horizontal acceleration

The first test case is that of the flow of two fluids in a rectangular tank moving with a horizontal acceleration. The height of the tank is $\mathrm{H} = 0.365\ \mathrm{m}$, the length is $\mathrm{L} = 0.584\ \mathrm{m}$, and the interface is located at $\mathrm{h_0} = 0.2\ \mathrm{m}$. This is a relatively simply case where the behavior of the enrichments can be easily assessed; the slope of the free water surface obtained at the steady regime can be compared with the theoretical result.

At the initial instant, the two fluids are at rest (cf. Figure 6.14), and then the acceleration is increased over a period T,

$$\begin{aligned} g_x(t) &= \frac{g}{3} \times \min\left(\frac{t}{T}, 1.0\right); \\ g_y(t) &= g. \end{aligned} \tag{6.15}$$

where $g = -9.81\ \mathrm{m/s^2}$ and $T = 2\ \mathrm{s}$.

The properties of the fluids are $\rho_1 = 1000\ \mathrm{kg/m^3}$, $\rho_2 = 1\ \mathrm{kg/m^3}$, $\mu_1 = 0.03\ \mathrm{kg/(m.s)}$, and $\mu_2 = 0.001\ \mathrm{kg/(m.s)}$. The influence of the surface tension is neglected in this test case. Slip boundary conditions are prescribed along the walls of the tank, and the reference pressure

$p = 0.0\ \mathrm{N/m^2}$ is applied at the top wall. The domain Ω is discretized with 1114 triangular elements (cf. Figure 6.14), and the simulation spans $3.0\ \mathrm{s}$.

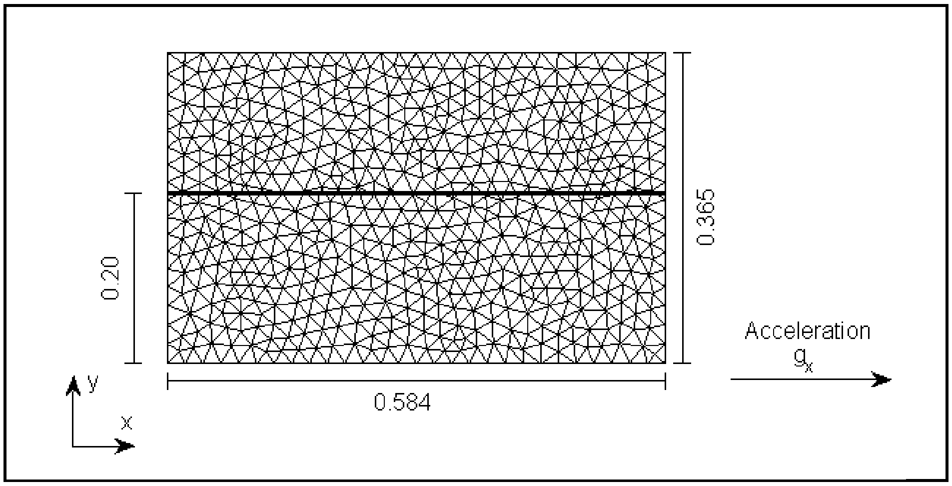

Figure 6.14 Tank under horizontal acceleration: initial configuration and computational mesh, $\mathrm{h}^e = 0.016$

The position of the interface between two fluids in a rectangular tank when the tank is subjected to constant acceleration along the $x-$direction is given by

$$y_0 = -\frac{g_x}{g_y}\left(x - \frac{\mathrm{L}}{2}\right) + \mathrm{h}_0 \tag{6.16}$$

where y_0 is the free surface height of the liquid from the bottom of the tank.

The observed flow shows an interface (free surface) whose slope gradually increases until it reaches a steady value close to the theoretical $S_{\mathrm{ex}} = -g_x/g_y = -1/3$ when the enrichments are stable.

Table 6-2 shows the relative error in the computed slope for different enrichments when a steady solution is reached.

$$E\,\% = \frac{|\,S_{\text{num}} - S_{\text{ex}}\,|}{|\,S_{\text{ex}}\,|}\times 100 \tag{6.17}$$

Table 6-2 Errors of the interface slope for different enrichments

case		**velocity**	**pressure**	$\boldsymbol{S}_{\textbf{num}}$	$\boldsymbol{E}$ **%**
1	$\emptyset - \mathrm{P}_1$ enrich.	none	$\mathrm{P}_1\times\mathrm{R}$	-0.3316	0.65 %
2		none	$\mathrm{P}_1\times\mathrm{sign}$	-0.3307	0.79 %
3	$\mathrm{P}_1 - \mathrm{P}_1$ enrich.	$\mathrm{P}_1\times\mathrm{R}$	$\mathrm{P}_1\times\mathrm{R}$	-	
4		$\mathrm{P}_1\times\mathrm{R}$	$\mathrm{P}_1\times\mathrm{sign}$	-	
5	$\mathrm{P}_2 - \mathrm{P}_1$ enrich.	$\mathrm{P}_2\times\mathrm{R}$	$\mathrm{P}_1\times\mathrm{R}$	incomputable	
6		$\mathrm{P}_2\times\mathrm{R}$	$\mathrm{P}_1\times\mathrm{sign}$	incomputable	

(-) computations diverge.

As indicated in cases (c) to (f) in Figure 6.15, when the velocity field is enriched, unstable solutions are obtained. In comparison, the solutions only enriched by the pressure field show no oscillations (cases (a) and (b) in Figure 6.15). The combination of enriched $\mathrm{P}_1 - \mathrm{P}_1$ approximations appears to suffer from instability (cases (c) and (d) in Figure 6.15); the segregated solver broke down during a fluid solve.

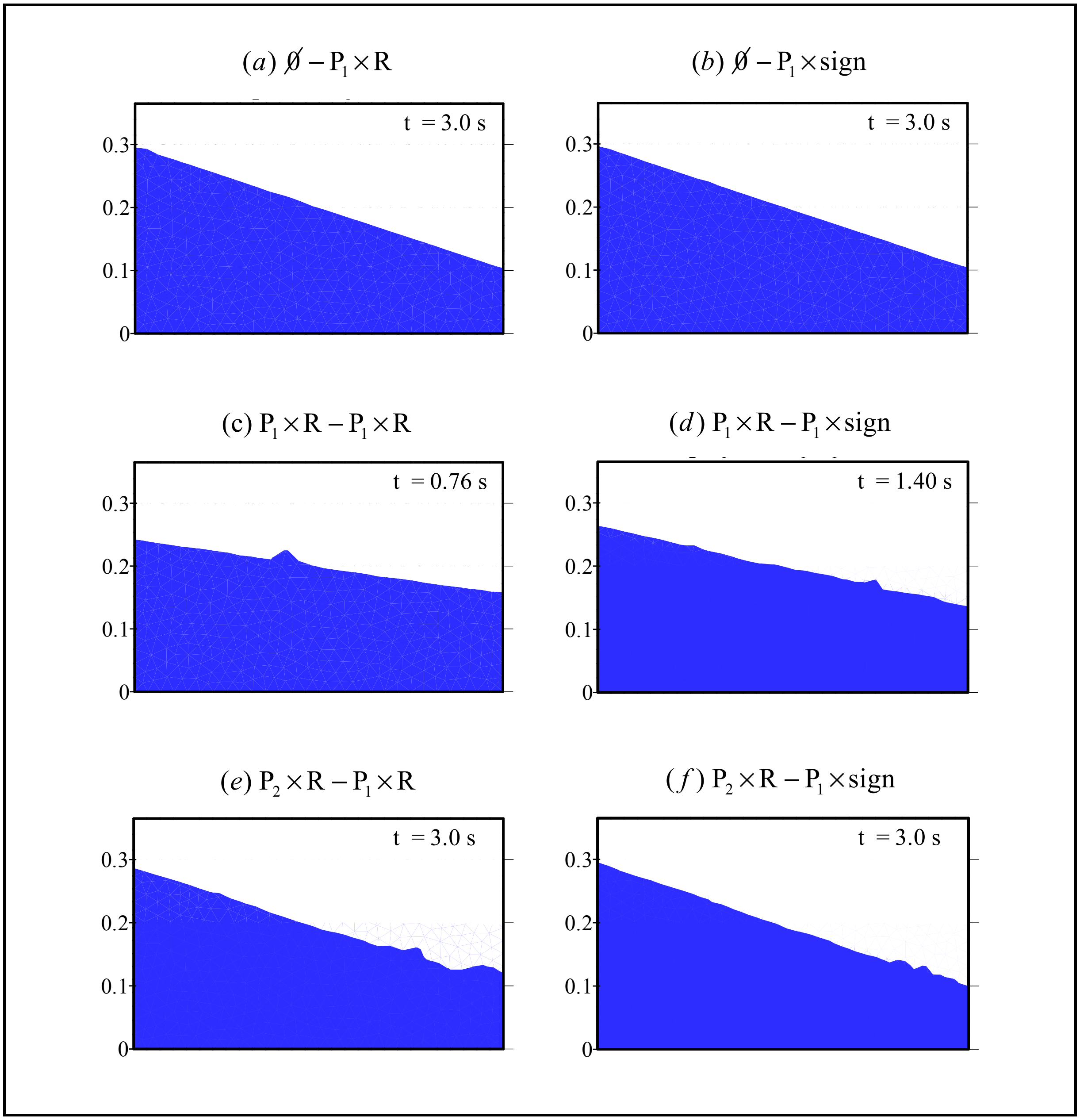

$(a)\ \emptyset - P_1 \times R$

$(b)\ \emptyset - P_1 \times \text{sign}$

$(c)\ P_1 \times R - P_1 \times R$

$(d)\ P_1 \times R - P_1 \times \text{sign}$

$(e)\ P_2 \times R - P_1 \times R$

$(f)\ P_2 \times R - P_1 \times \text{sign}$

Figure 6.15 Tank under horizontal acceleration: free surface for different enrichments

The velocity enrichment led to spurious velocities or unphysical currents close to the interface. These parasite velocities initially disrupt the flow, leading to the phenomenon being amplified until the system can no longer be resolved (cf. Figure 6.15(c) and (d)). We observe that these currents decrease slightly in magnitude with the increased mesh refinement and/or with smaller computational time steps.

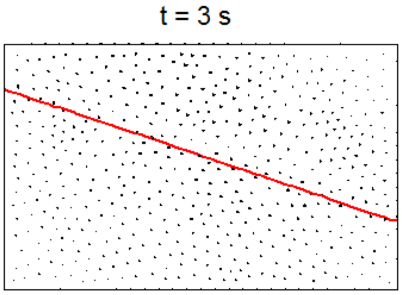

(a) ϕ - P_1 enrich., || $\mathbf{u}_{max}$ || = 0.022

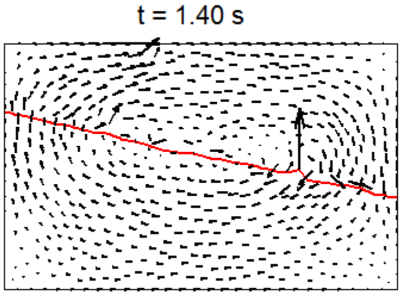

(b) P_1 - P_1 enrich., || $\mathbf{u}_{max}$ || = 0.455

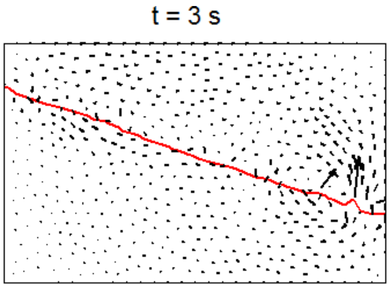

(c) P_2 - P_1 enrich., || $\mathbf{u}_{max}$ || = 0.328

Figure 6.16 Parasite velocities: the $\emptyset - \mathrm{P}_1$ enrichment (a) performs better than the $\mathrm{P}_1 - \mathrm{P}_1$ (b) and the $\mathrm{P}_2 - \mathrm{P}_1$ (c) enrichments

We conclude that velocity enrichments require additional stabilization terms in the variational formulation, as performed in (Schott, Rasthofer et al. 2015). These results motivate the decision to not enrich the velocity field, but rather employ a smoother viscosity (6.18) across the interface. The subsequent test cases will further justify this choice.

The viscosity μ in the flow field can be smoothed out across the interface as

$$\mu(\phi) = 1 + \left(\frac{\mu_i}{\mu_j} - 1 \right) H_\alpha(\phi) \tag{6.18}$$

in which subscripts i and j denote two adjacent phases, and the smoothed Heaviside function is usually expressed as:

$$H_\alpha(\phi) = \begin{cases} 0 & \phi \le -\alpha \\ \dfrac{(\phi+\alpha)}{2\alpha} + \dfrac{\sin(\pi\phi/\alpha)}{2\pi} & |\phi| < \alpha \\ 1 & \phi \ge \alpha \end{cases} \tag{6.19}$$

where α represents the interface thickness. This parameter must be chosen adequately, we refer to (Zahedi and Tornberg 2010) for a discussion of how the regularisation zone decays for different values of $\alpha = m\,\mathrm{h}^e$. Based on these results, we have chosen $\alpha = 1.5\,\mathrm{h}^e \sim 2\,\mathrm{h}^e$.

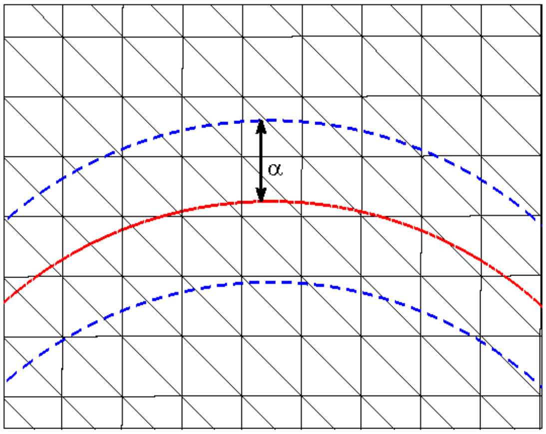

Figure 6.17 Numerical smoothing region

6.2.2 Sloshing flow in a tank

We consider a two-phase sloshing flow. The sloshing of liquids in moving containers is of practical concern in many engineering applications, such as containers for transporting liquids on highways, the design of automotive fuel tanks, seismically excited storage tanks, ships and space vehicles, and dams. The amplitude of the sloshing depends on the frequency and amplitude of the tank motion, the fluid fill level, the tank geometry and the liquid properties. The unsteady character of the flow and the strong deformation of the interface make this case test interesting for assessing the numerical solver.

The domain Ω is a rectangular tank with height $\mathrm{H} = 0.50\,\mathrm{m}$ and width $\mathrm{L} = 1\,\mathrm{m}$. The two fluids in Ω_1 and Ω_2 are initially at rest and separated by a horizontal level set $\mathrm{h}_0 = 0.275\,\mathrm{m}$ (cf. Figure 6.18). The fluids' movement is driven by an oscillating gravity vector. This is to mimic a periodic 'tank' motion, swinging forth and back and pointing up to 4 degrees away from the downward y direction at its limits,

$$\begin{aligned} g_x(t) &= -g\sin\left(\theta_{\max}\sin(2\pi f\,t)\right); \\ g_y(t) &= g\cos\left(\theta_{\max}\sin(2\pi f\,t)\right). \end{aligned} \tag{6.20}$$

where $g = -9.81\,\mathrm{m/s^2}$, $\theta_{\max} = 4\pi/180$, and $f = 1\,\mathrm{Hz}$.

The densities of the two fluids in Ω_1 and Ω_2 are $\rho_1 = 1000\,\mathrm{kg/m^3}$ and $\rho_2 = 1\,\mathrm{kg/m^3}$, and the dynamic viscosities are $\mu_1 = 0.03\,\mathrm{kg/(m.s)}$ and $\mu_2 = 0.001\,\mathrm{kg/(m.s)}$, respectively. The influence of the surface tension is neglected in this test case.

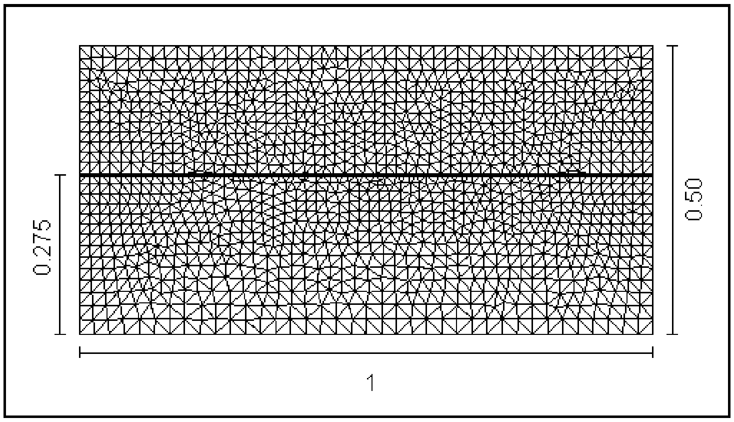

Figure 6.18 Sloshing tank: initial configuration and computational mesh, with $h^e \approx 0.015$

Slip boundary conditions are prescribed along the walls of the tank, and $p = 0.0 \text{ N/m}^2$ is set along the upper boundary. The domain Ω is discretized with 2497 triangular elements (cf. Figure 6.18), and the simulation spans $t_{end} = 6.0 \text{ s}$.

No enrichment is used for the velocity field, which is continuous at the interface and merely exhibits a kink; however, the pressure field is enriched with either the sign-enrichment or the Ridge-enrichment.

The simulation presented is not based on any experimental or analytical test case; it only serves to show the potential of the method to capture the large-amplitude sloshing.

The fluid movement thus initiated tends to amplify, forming a large-amplitude wave. Figure 6.19 shows the interface position and velocity solution in m/s for various time instances using the $\not{0} - \text{P}_1 \times \text{sign}$ enrichment. The inclination angle of the tank is exactly the same as the angle of the gravity vector from its initial vertical position.

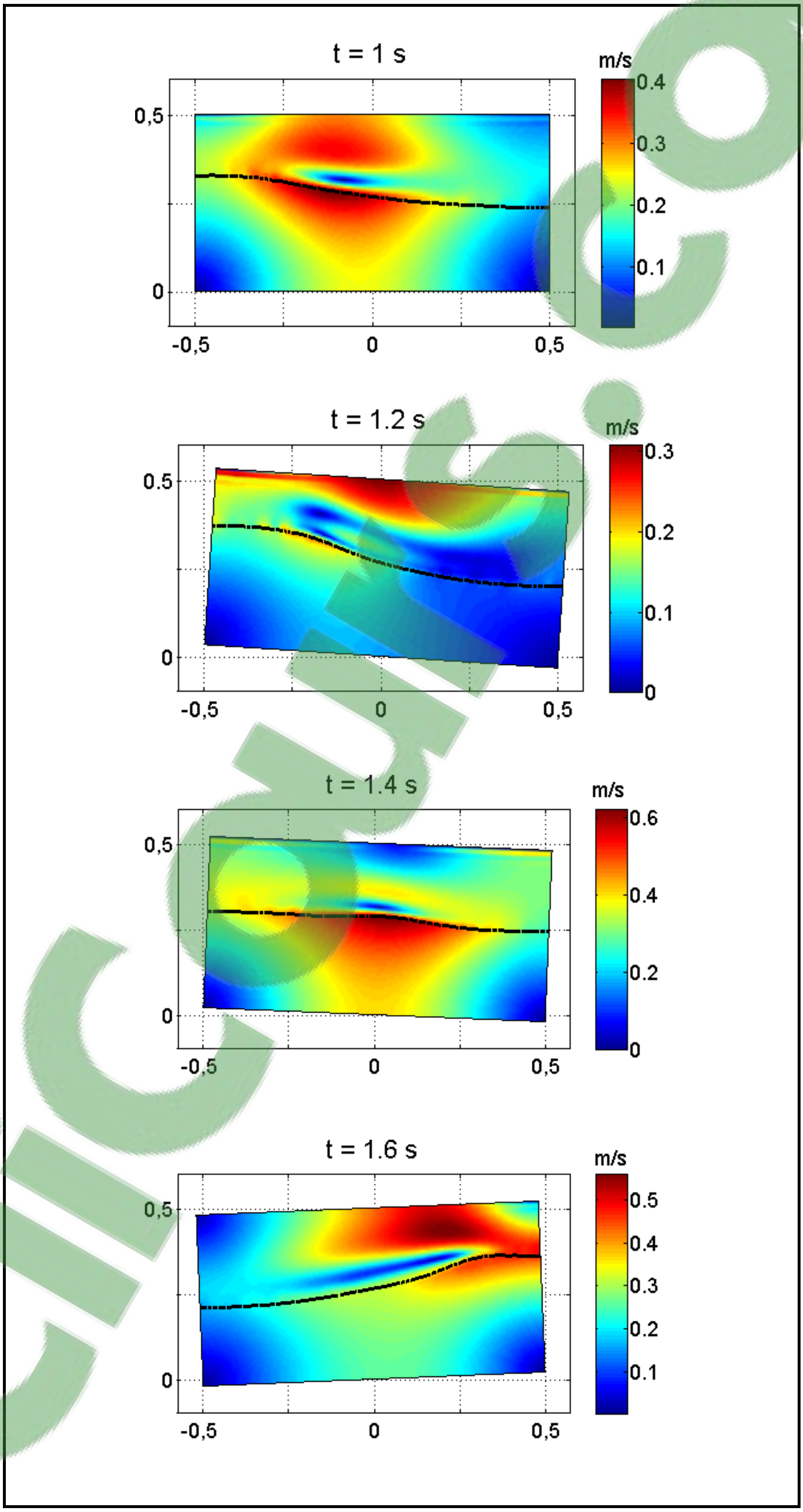

Figure 6.19 Sloshing tank: interface position and velocity solution in m / s for various time instances

To depict the dynamics in the tank, we plot the interface height versus time at the right side wall, as shown in the following plot.

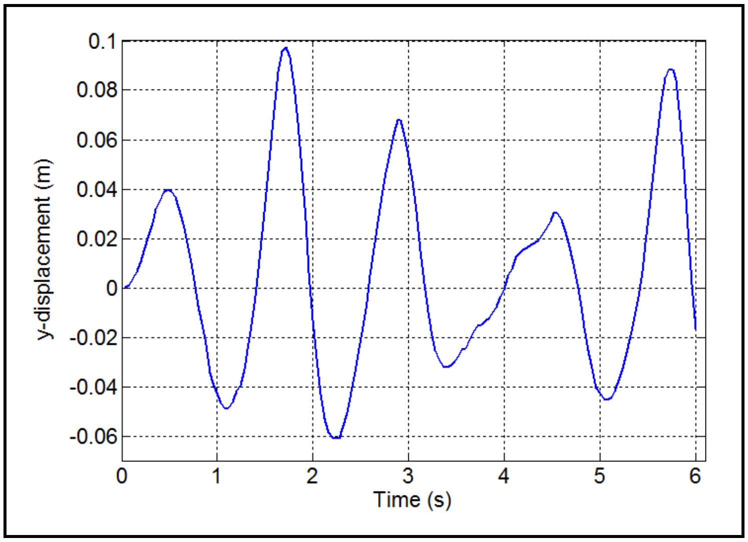

Figure 6.20 Sloshing tank: interface height at the right side wall

6.2.2.1 Comparison of $\emptyset - P_1 \times R$ and $\emptyset - P_1 \times \mathrm{sign}$ enrichment

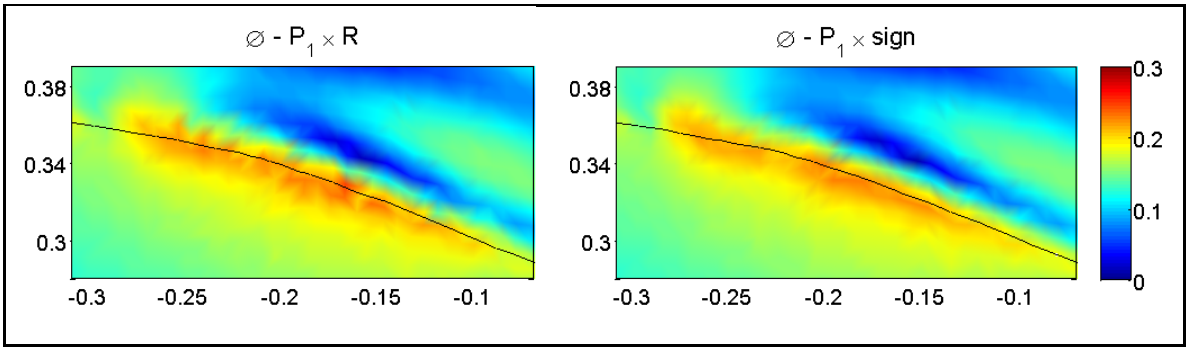

Figure 6.21 Sloshing tank: comparison of snapshots of the velocity field at $t = 1.20\ \mathrm{s}$

Figure 6.21 illustrates that $\emptyset - \mathrm{P}_1 \times \mathrm{R}$ enrichment leads to disturbed and higher values for the velocity field, while a smooth and regular velocity field can be observed using $\emptyset - \mathrm{P}_1 \times \mathrm{sign}$ enrichment.

Finally, we perform a study on the mass conservation properties of the two enrichments. Because both fluids are incompressible, the densities are constant. Mass conservation then dictates that the area of each fluid should not change over time. Figure 6.23 compares the mass errors of the liquid in Ω_1 over time calculated by

$$\text{Mass error } \% = \frac{\left| A\left(\Omega_1(t)\right) - A\left(\Omega_1(t=0)\right) \right|}{A\left(\Omega_1(t=0)\right)} \times 100 \qquad (6.21)$$

where $A\left(\Omega_1(t)\right)$ is the total area of the liquid in Ω_1 at time t. We should note that we have not used any *ad hoc* algorithm to enforce the global mass conservation.

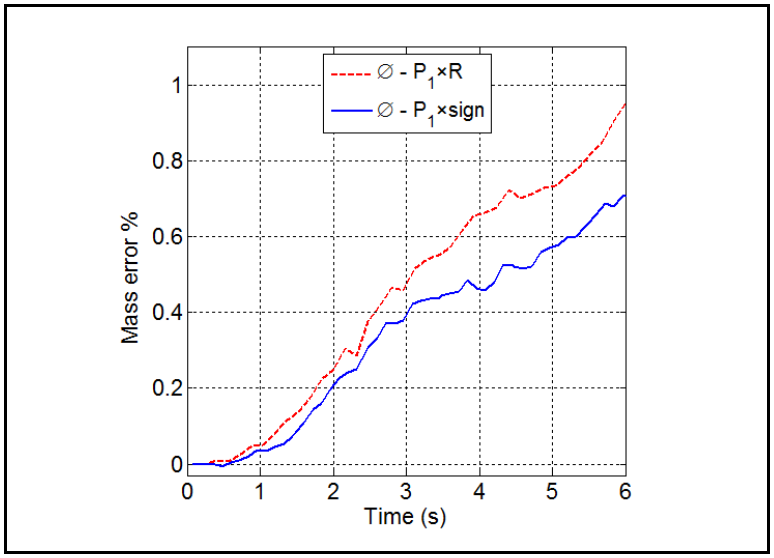

Figure 6.22 Sloshing tank: mass conservation for $\mathrm{t} \in [0, 6\ \mathrm{s}]$

As mentioned before, the surface tension force is neglected; the magnitude of the pressure jump across the interface depends on the jump in the normal derivative of the normal velocity u_n and the jump in the viscosity. Although the jump in the viscosity is too small, this error ($-\llbracket p \rrbracket + 2\llbracket \mu \frac{\partial u_n}{\partial n_{\mathrm{int}}} \rrbracket \neq 0$) should not be neglected. This is may be the reason that the $\emptyset - \mathrm{P}_1 \times \mathrm{sign}$ enrichment is more accurate compared to the $\emptyset - \mathrm{P}_1 \times \mathrm{R}$ enrichment.

We also tested the procedure, described in Section 3.3.1, for the subcell division required for the Gaussian quadrature of the Galerkin weak form. We recall that the numerical integration used employs the subdivision procedure ($\mathrm{n}_r = 1$). For comparison, the above test is repeated for the $\emptyset - \mathrm{P}_1 \times \mathrm{sign}$ enrichment without any subdivision ($\mathrm{n}_r = 0$). Figure 3.3 shows an improvement in the mass conservation using the subdivision integration.

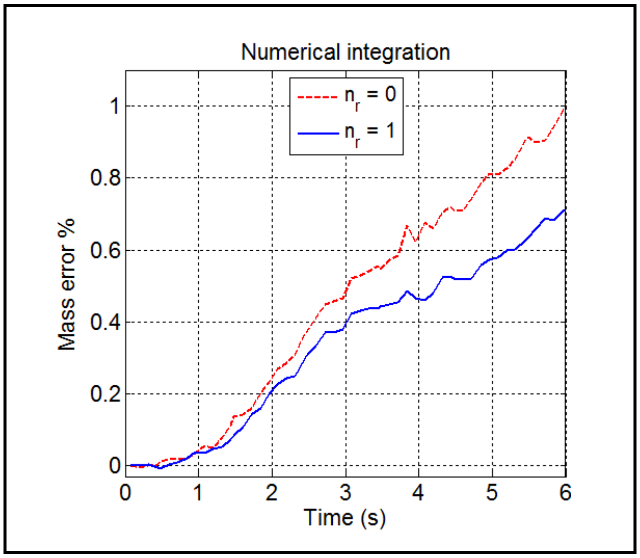

Figure 6.23 Sloshing tank: comparison of mass conservation using $\mathrm{n}_r = 0$ and $\mathrm{n}_r = 1$ for the numerical integration

6.2.3 Dam break problem

The simulation of the collapse of a column of water in a tank is a test case commonly used to validate the ability of a code to simulate complex unsteady free surface flows. The simulations presented here correspond to the experimental tests carried out by Martin and Moyce (Martin and Moyce 1952) and Koshizuka et al. (Koshizuka, Tamako et al. 1995).

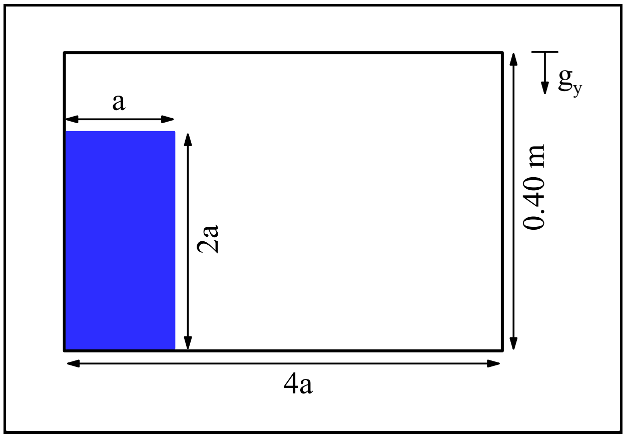

Figure 6.24 Dam break problem: initial configuration

The problem consists of a rectangular column of water initially sustained by a dam that is suddenly removed. Under the influence of gravity $\mathbf{g} = (0.0, -9.81)^T$ m/s^2, the water collapses and flows downward until it violently hits the opposite wall. Then, the water rises along the wall and collapses again, producing a sloshing effect.

The maximum flow speed, between the instants $t = 0.23$ s and $t = 0.27$ s, exceeds 2.60 m/s, and the depth is approximately 0.05 m. The Reynolds number based on these values is $\mathrm{Re} = 13000$.

The domain Ω, as shown in Figure 6.24, is a tank with dimensions $[0, 4a]\times[0, 0.40]$, where $a = 0.146$ m, following references (Martin and Moyce 1952) and (Koshizuka, Tamako et al. 1995). The water column has dimensions $[0, a]\times[0, 2a]$. The densities of the fluids are $\rho_1 = 1000$ kg/m^3 and $\rho_2 = 1$ kg/m^3, and the dynamic viscosities are $\mu_1 = 0.01$ kg/(m.s) and $\mu_2 = 0.001$ kg/(m.s). The influence of surface tension is neglected in this test case.

Slip boundary conditions are assumed along the three solid walls and the upper boundary is free; a zero-traction Neumann boundary condition is set along the upper boundary. The computational domain is discretized with 1949 elements $(38\times25)\times2$, and the simulation lasts for $t_{end}=1.0\ \mathrm{s}$.

In Figure 6.26 the evolution of the free surface is compared with the experimental results published in (Koshizuka, Tamako et al. 1995), showing good qualitative agreement.

The evolution of the water front x_w, the position of its tip $x_w(t=0)=a$, and the height y_w of the column, measured at the left vertical wall $y_w(t=0)=2a$, as functions of time are shown in Figure 6.25. For comparison, the experimental values taken from Martin and Moyce (Martin and Moyce 1952), denoted by "MM", are also included.

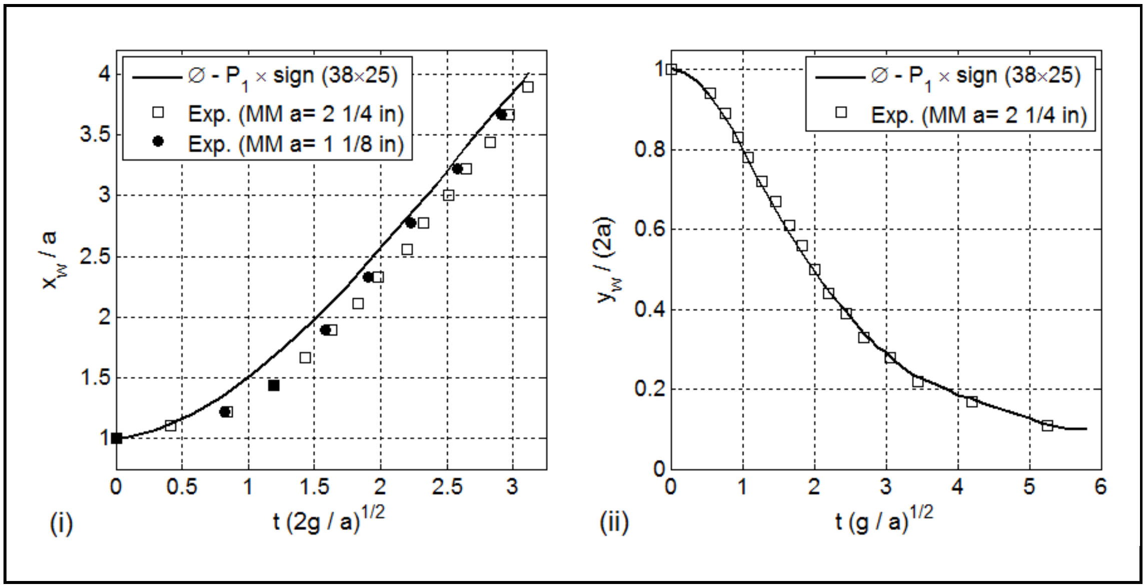

Figure 6.25 Dam break problem: Dimensionless width x_w/a (i) and height $y_w/(2a)$ (ii) as a function of time, comparison with experimental data from (Martin and Moyce 1952)

We observe the good agreement between the numerical results and the experimental data (Martin and Moyce 1952). The observed difference in Figure 6.25(i) (dimensionless width of the water column as a function of time) may be explained by the slip boundary condition assumed at the side walls and the bottom of the numerical test setup. Note also that the experimental data deviate somewhat from each other.

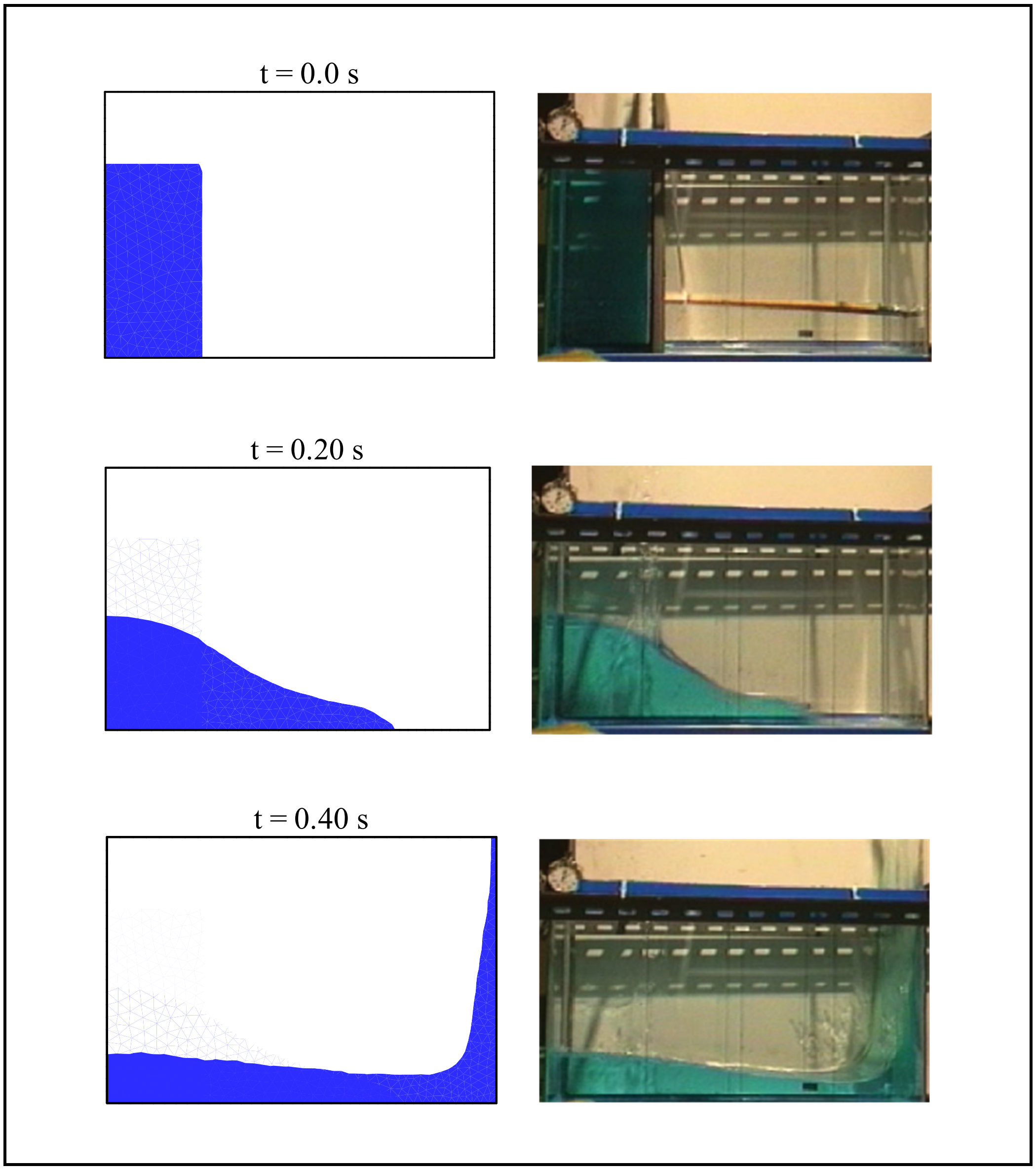

t = 0.0 s

t = 0.20 s

t = 0.40 s

Figure 6.26 Dam break problem: comparison of the numerical and experimental (Koshizuka, Tamako et al. 1995) free surfaces

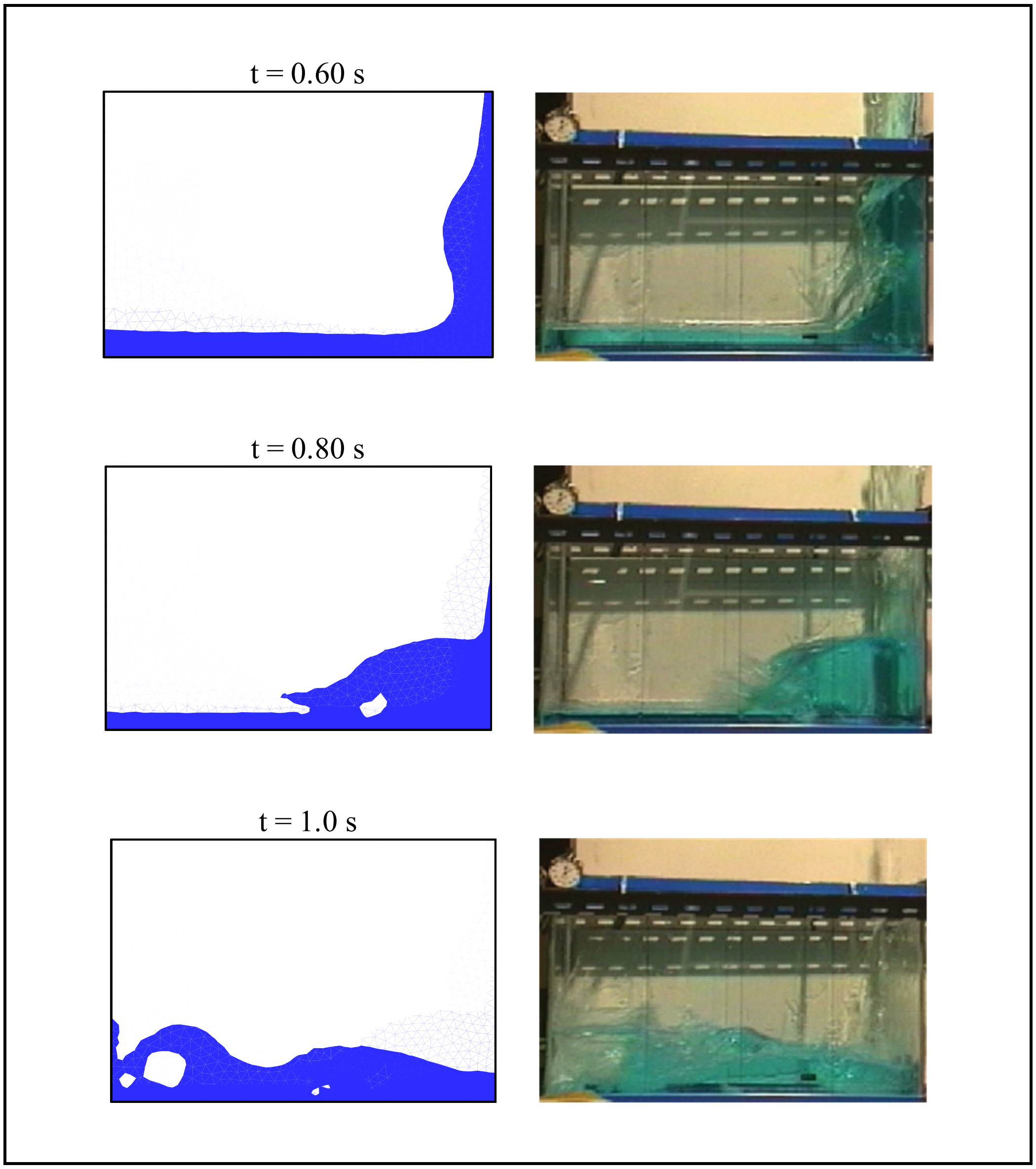

Figure 6.26 Continued

6.2.4 Dam break with an obstacle

A more severe case, which has been considered by Greaves (Greaves 2006), Koshizuka et al. (Koshizuka, Tamako et al. 1995), and Ubbink (Ubbink 1997), amongst others, is when a rectangular obstacle (0.024×0.048 m) is placed on the bottom of a tank (cf. Figure 6.27).

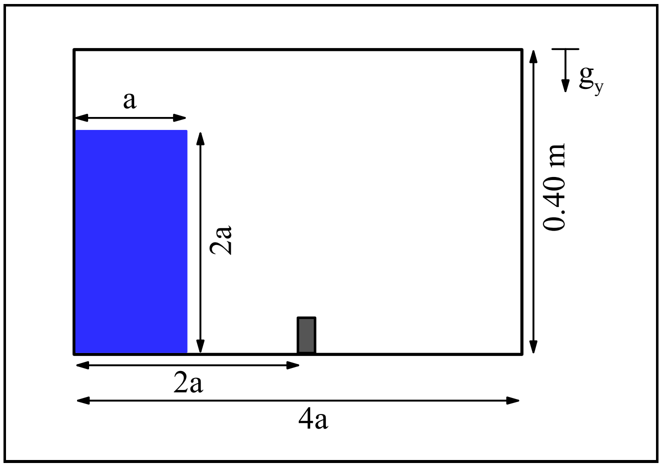

Figure 6.27 Dam break with an obstacle: initial configuration

The domain is discretized with 2684 elements, and the simulation lasts for $t_{end} = 0.50\text{ s}$.

The evolution of the free surface is compared with the snapshots taken by Koshizuka et al. (Koshizuka, Tamako et al. 1995) in Figure 6.28. The agreement between the experimental and numerical results is very good; the simulation accurately captures the instant that the wave hits the opposite wall. However, there are small differences at instant $t = 0.50\text{ s}$, when the interface is highly contorted with considerable spray.

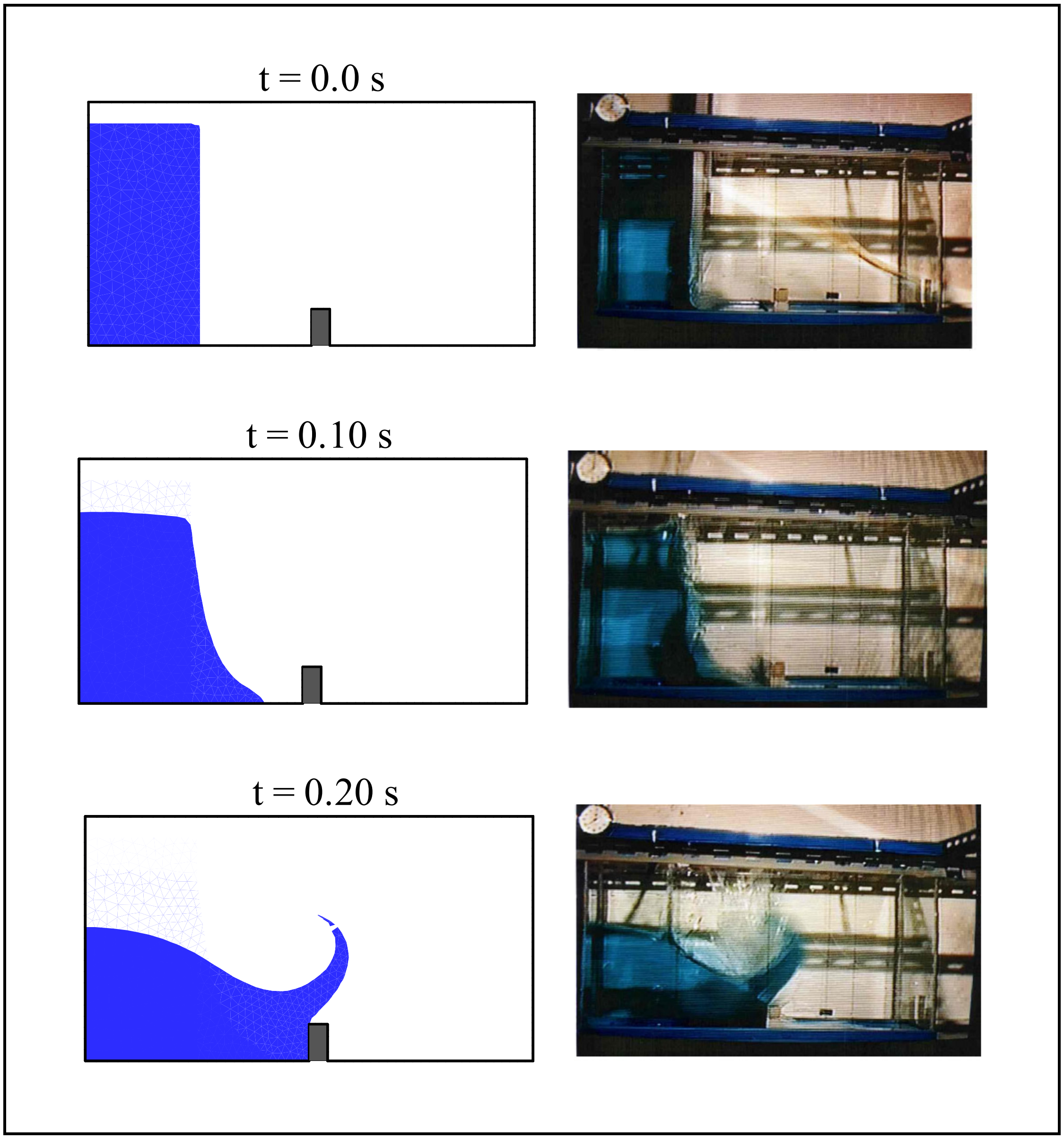

Figure 6.28 Dam break with an obstacle: comparison of the numerical and experimental (Koshizuka, Tamako et al. 1995) free surfaces

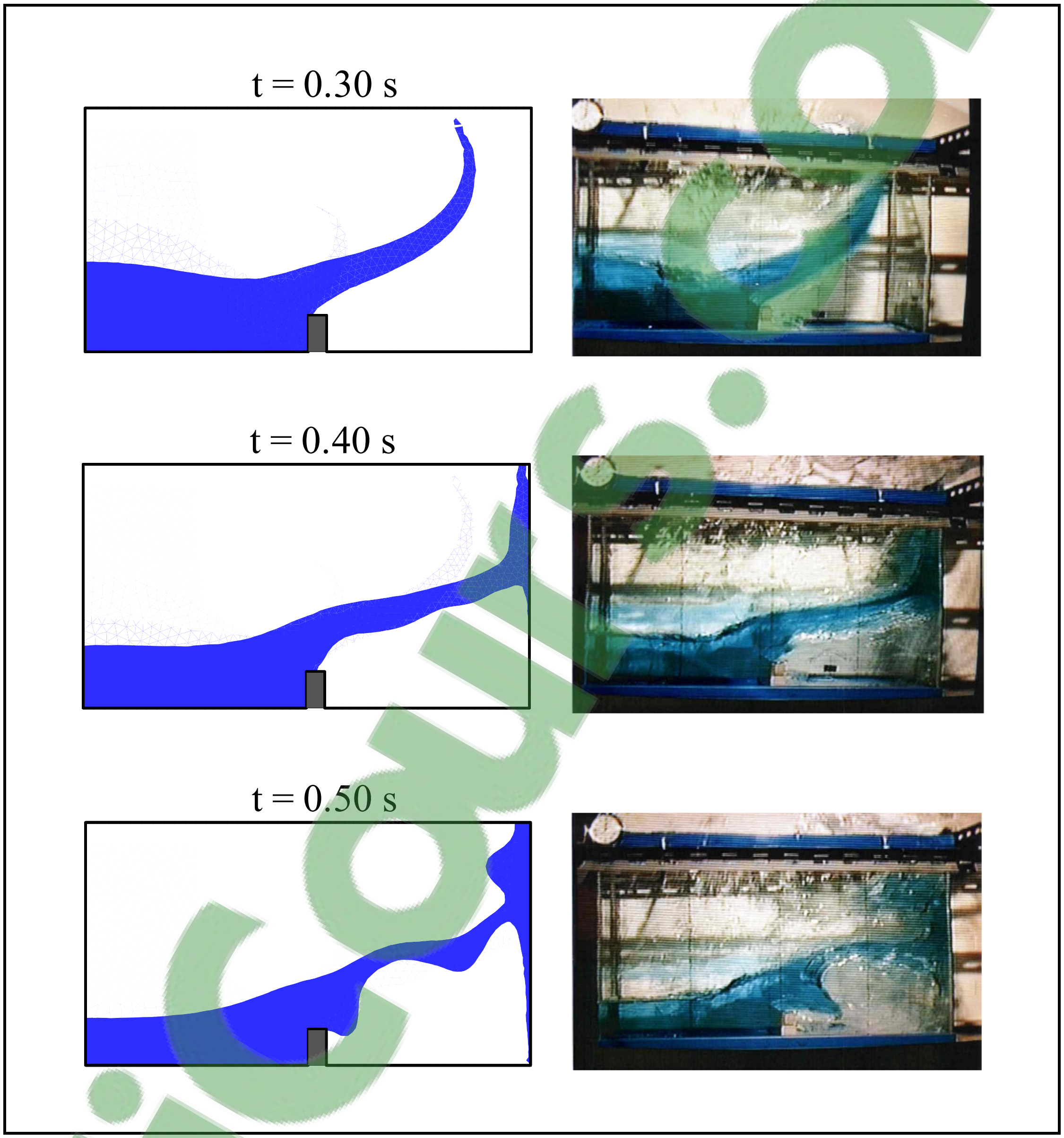

Figure 6.28 Continued

6.2.5 Bubble rising in a container fully filled with water

We consider in this subsection the problem of a bubble rising in water due to buoyancy. Until now, we have only studied test cases with weak discontinuities along the moving interface.

To test the ability of $\emptyset-\mathrm{P}_1\times\mathrm{sign}$ enrichment to address situations where a large surface tension exists, we consider a test case from (Hysing, Turek et al. 2009).

We initially placed a circular bubble of diameter $D_0 = 0.50\ \mathrm{m}$ centered at $(0.50, 0.50)^{\mathrm{T}}\ \mathrm{m}$ in a $1.0\times2.0\ \mathrm{m}$ rectangular domain, see Figure 6.29. Gravitation acts in the vertical y-direction as $\mathbf{g} = (0.0, -0.98)^{\mathrm{T}}\ \mathrm{m/s^2}$. The properties of the fluids are listed in Table 6-3.

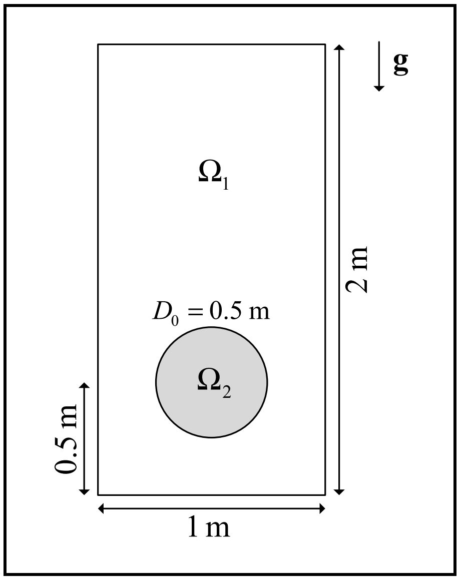

Figure 6.29 Rising bubble: initial configuration

Table 6-3 Physical properties and dimensionless numbers defining test case

$\rho_1\left(\frac{\mathrm{kg}}{\mathrm{m^3}}\right)$	$\rho_2\left(\frac{\mathrm{kg}}{\mathrm{m^3}}\right)$	$\mu_1\left(\frac{\mathrm{kg}}{\mathrm{m\cdot s}}\right)$	$\mu_2\left(\frac{\mathrm{kg}}{\mathrm{m\cdot s}}\right)$	$\gamma\left(\frac{\mathrm{kg}}{\mathrm{s^2}}\right)$	**Re**	**Eo**	ρ_1/ρ_2	μ_1/μ_2
1000	100	10	1	24.5	35	10	10	10

where the Reynolds and Eötvös numbers are defined as

$$\mathrm{Re} = \frac{\rho_2 \sqrt{g D_0}\, D_0}{\mu_2}, \tag{6.22}$$

$$\mathrm{Eo} = \frac{g\, \rho_2\, D_0^2}{\gamma^2} \tag{6.23}$$

Depending on these characteristic numbers, three regimes can be distinguished for the bubble shapes: spherical bubbles ($\mathrm{Re} < 1$ and $\mathrm{Eo} < 1$); ellipsoidal bubbles ($1 < \mathrm{Re} < 100$ and $1 < \mathrm{Eo} < 100$); and cap-like bubbles ($100 < \mathrm{Re} < 500$ and $100 < \mathrm{Eo} < 500$).

In this case test, we consider a nine-node biquadratic quadrilateral element in which the velocity is biquadratic (defined through nine nodes) while the pressure is bilinear (defined through the four corner nodes).

The pressure approximation is sign-enriched (i.e., $\emptyset - \mathrm{Q}_1 \times \mathrm{sign}$). Slip boundary condition was imposed on the vertical walls, no-slip conditions on the horizontal walls, and $p = 0.0\ \mathrm{N/m^2}$ on the upper wall. As an initial condition, the velocity field is set to $\mathbf{0}$. Computations were conducted until $t_{\mathrm{end}} = 3\ \mathrm{s}$ with a time step of $\Delta t = 0.003\ \mathrm{s}$. The reinitialization procedure is performed using a refinement level $\mathrm{n_r} = 5$.

Two methods of calculating the normal vector $\mathbf{n}_{\mathrm{int}}$ are compared:

- method $L2-\mathrm{Q9}$: The normal vector is computed by means of the L2-projection method, as described in section 4.1.1;
- method $Geo-\mathrm{Q9}$: The normal vector is computed by using a piecewise linear interface and a constant refinement level of $\mathrm{n_r} = 5$, as described in section 4.1.2.

To evaluate the behavior of the new method $Geo-\mathrm{Q}9$, we compare results from three successively refined non-uniform meshes, see Figure 6.30.

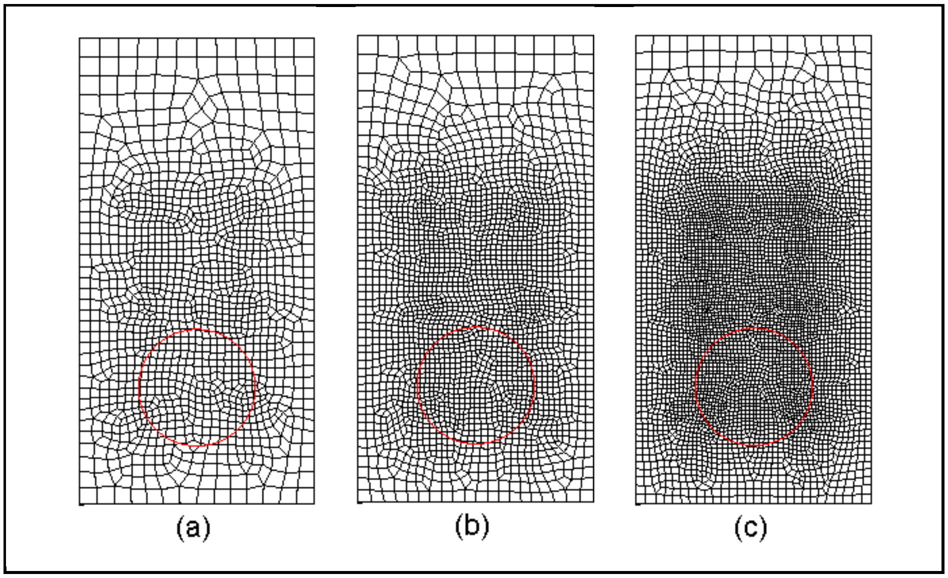

Figure 6.30 Rising bubble: snapshots of the three computational meshes. (a) 1280 elements; (b) 2508 elements; (c) 4781 elements

Figure 6.31 depicts the interface position at different time instances as well as the pressure field. We can clearly observe a jump in the pressure field. The bubble gets deformed while remaining compact. This is due to the low Eo number (high surface tension) and low density and viscosity ratios.

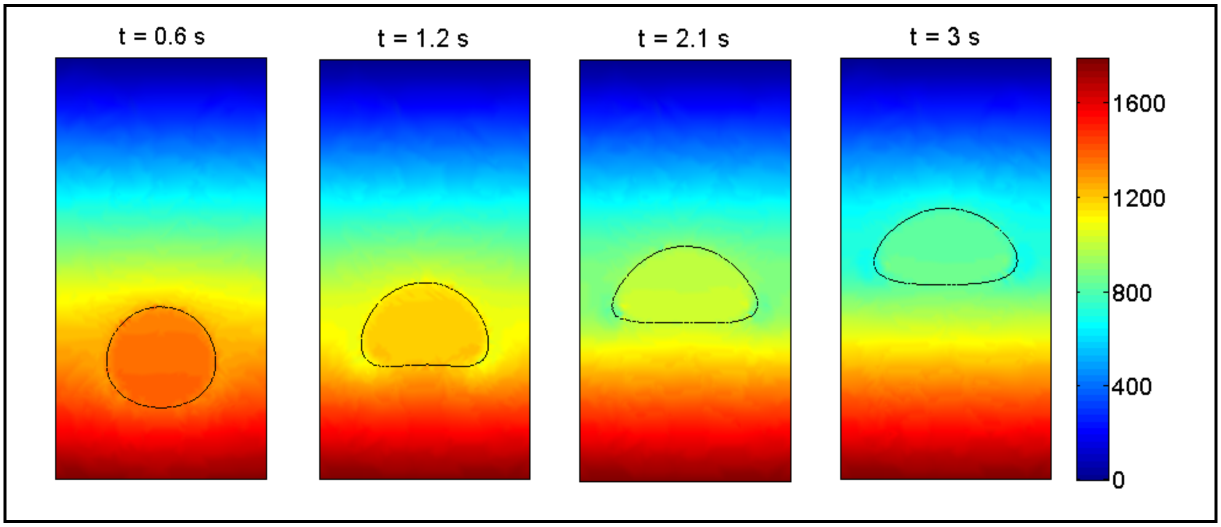

Figure 6.31 Rising bubble: pressure solution in $\mathrm{N/m^2}$ and interface position for various time instances

The following parameters were considered to compare the simulation results with the reference data of Hysing et al. (Hysing, Turek et al. 2009):

- center of mass: can be used to track the translation of a bubble, defined by

$$\mathbf{x}_{\mathrm{G}} = (x_{\mathrm{G}}, y_{\mathrm{G}}) = \frac{\int_{\Omega_2} \mathbf{x}\, \mathrm{d}\Omega}{\int_{\Omega_2} \mathbf{1}\, \mathrm{d}\Omega} \tag{6.24}$$

where Ω_2 denotes the region that the bubble occupies (cf. Figure 6.29).

- rise velocity or terminal velocity: terminal velocity is the constant velocity of a rising bubble when time no longer significantly influences the local velocity:

$$\mathbf{u}_{\mathrm{G}} = (u_{\mathrm{G}}, \upsilon_{\mathrm{G}}) = \frac{\int_{\Omega_2} \mathbf{u}(\mathbf{x},t)\, \mathrm{d}\Omega}{\int_{\Omega_2} \mathbf{1}\, \mathrm{d}\Omega} \tag{6.25}$$

Figure 6.32 illustrates the temporal evolution of the parameters' center of mass position and rising velocity. The velocity increases until a maximum and then decreases to a constant value.

Table 6-4 presents data collected in the simulations and compares them to results observed in simulations by (Hysing, Turek et al. 2009).

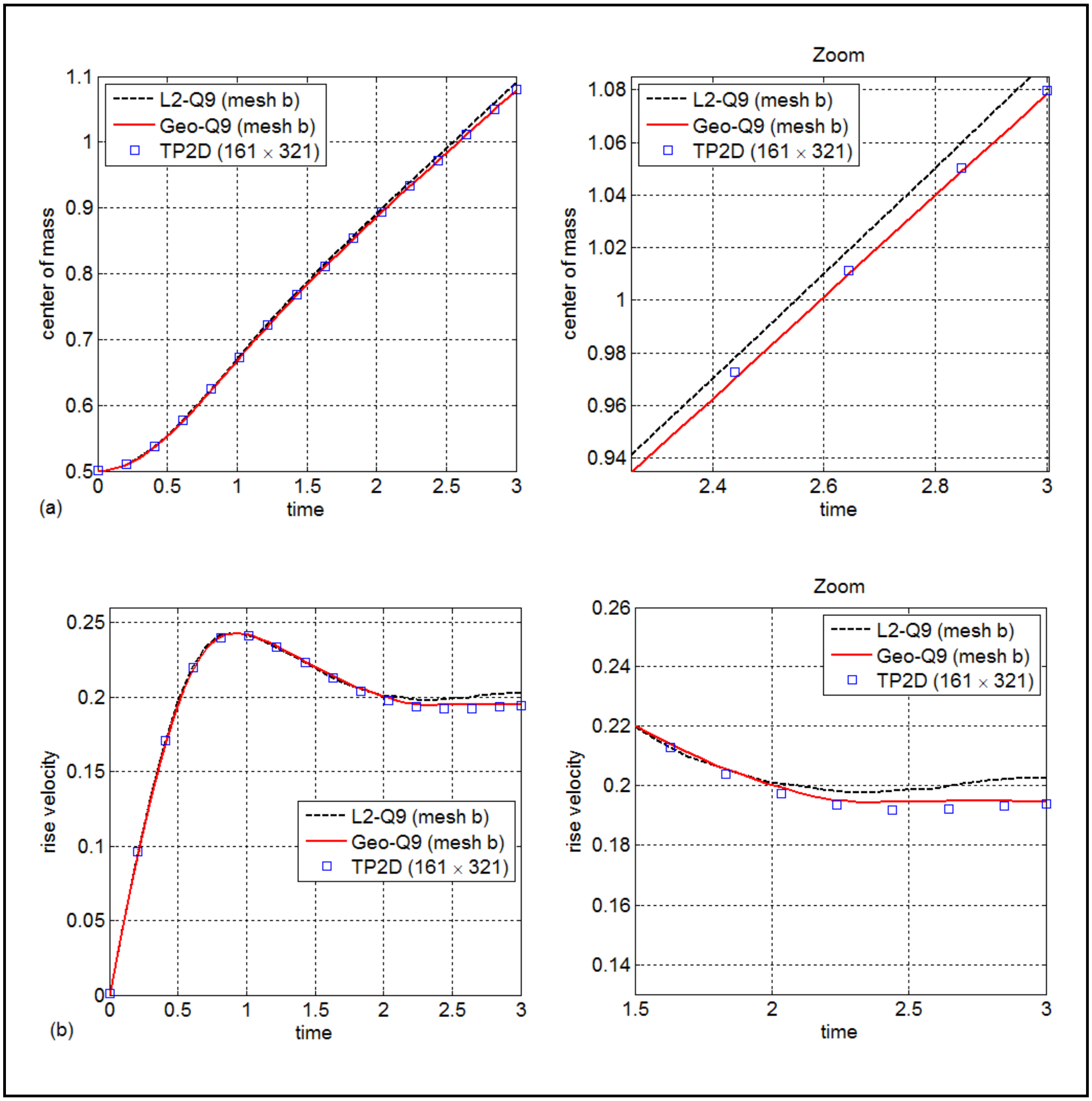

Figure 6.32 Rising bubble: temporal evolution of (a) center of mass position and (b) rising velocity. Comparison of the results with simulation data from (Hysing, Turek et al. 2009)

Table 6-4 Collected data from simulations and reference values observed in simulations by (Hysing, Turek et al. 2009)

	Average ($\mathbf{h}_i^e$)	**0.0363**	**0.0257**	**0.0185**	**Reference values**
Max rise velocity	$L2-\mathrm{Q}9$	0.2315	0.2457	0.2490	0.2417
	$Geo-\mathrm{Q}9$	0.2362	$\boxed{0.2405}$	0.2445	
Time for max velocity	$L2-\mathrm{Q}9$	0.9197	0.9243	0.9283	0.9213
	$Geo-\mathrm{Q}9$	0.9189	$\boxed{0.9217}$	0.9254	
Center of mass at $t=3$ s	$L2-\mathrm{Q}9$	1.0822	1.0863	1.0896	1.0813
	$Geo-\mathrm{Q}9$	1.0688	1.0754	$\boxed{1.0798}$	

We observe that the $Geo-\mathrm{Q}9$ method yields a better accuracy than the $L2-\mathrm{Q}9$ method.

The level set function is reinitialized using the straightforward approach. For details, please refer to section 3.5. Due to the piecewise linear nature of the interpolated interface, kinks exist in the level set function. Therefore, any existing noise in the gradient, i.e., the normal vectors, was further amplified. This is the main reason why the $L2-\mathrm{Q}9$ method fails to accurately compute the curvature.

Figure 6.33 compares the bubble shape at the final time ($t=3\,\mathrm{s}$) with the results from (Hysing, Turek et al. 2009). A similar conclusion can be drawn for the results, i.e., the $Geo-\mathrm{Q}9$ method yields the best accuracy.

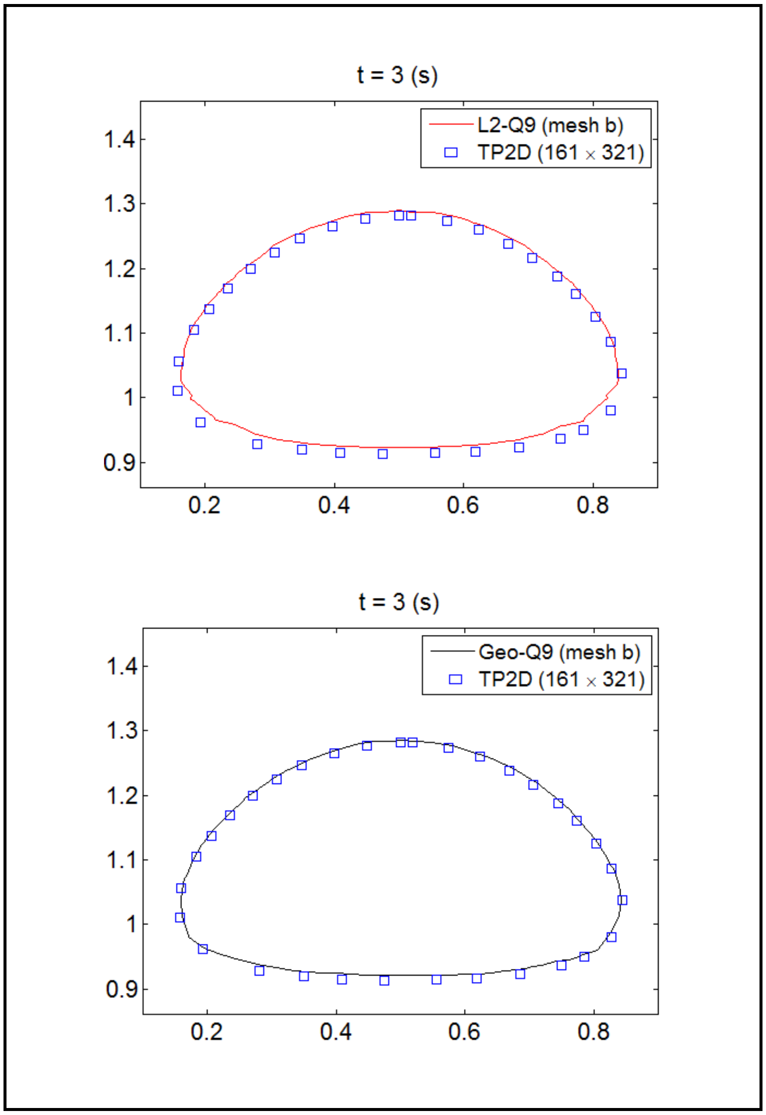

Figure 6.33 Rising bubble: final shape of the bubble at $t = 3$ s and reference solution by Hysing et al. (Hysing, Turek et al. 2009)

Table 6-5 compares the mass errors of the bubble for the two methods of calculating the normal vector using different non-uniform grid resolutions.

Table 6-5 Mass errors for rising bubble at $t = 3$ s

	Average (h_i^e)	**0.0363**	**0.0257**	**0.0185**
Mass error (%)	$L2-\mathrm{Q9}$	5.20	3.16	2.21
	$Geo-\mathrm{Q9}$	2.03	1.26	0.79

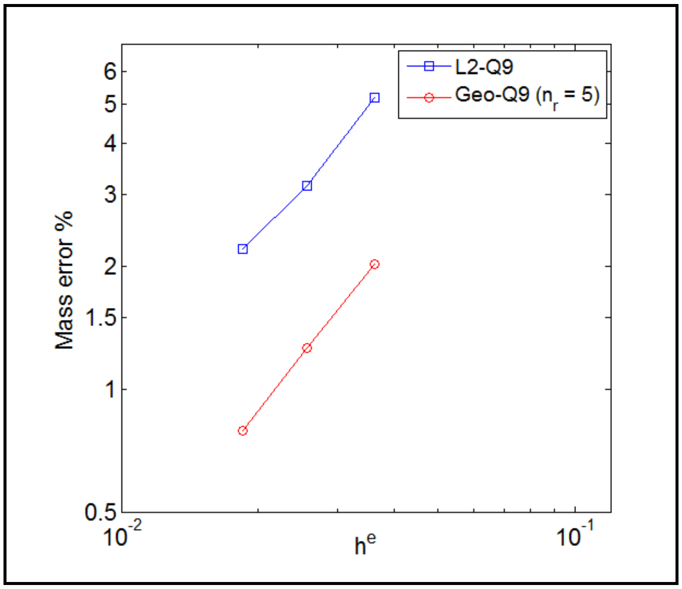

Figure 6.34 Rising bubble: mass errors at $t = 3$ s

Figure 6.34 shows that the $Geo-\mathrm{Q9}$ method leads to a much better mass conservation compared to the $L2-\mathrm{Q9}$ method.

CONCLUSION

In this thesis, the XFEM/level set methods have been studied to solve the incompressible flows of two immiscible fluids. Such a combination of those two numerical methods results in a simple, general, and effective algorithm capable of simulating diverse flow regimes presenting large viscosity and density ratios (up to 1000) and large surface tension. Different enrichment schemes have been investigated for the well-known Taylor-Hood element without any stabilization.

In problems with stationary interfaces, we found that the enrichment of the velocity field offers the potential for significant improvements in the accuracy and convergence rates, in particular when the interpolation of the velocity enrichment ($N_i^{\mathbf{u}*}(\mathbf{x})$) is one order less than that used in the standard FE part ($N_i^{\mathbf{u}}(\mathbf{x})$). Very accurate results and optimal convergence rates have been obtained by means of the sign-enrichment for weak or strong discontinuities in the pressure field. However, the linear dependency is a considerable issue of this enrichment. The accuracy and the stability are significantly affected as shown by our numerical studies.

In problems with moving interfaces, severe instabilities may appear, especially when the velocity is enriched. For free surface flows driven by gravity (surface tension is neglected) and for relatively high Reynolds numbers, pressure enrichment is sufficient to obtain accurate and very stable solutions. The sign-enrichment is superior to Ridge-enrichment, regardless of whether the surface tension dominates.

A novel method of computing the vectors normal to the interface has been proposed. This method computes the normal vectors by employing the successive refinement of the mesh inside the cut elements. The normal vectors thus constructed are perfectly perpendicular to the interpolated interface. Comparisons with analytical solutions and numerical results demonstrate that the method is accurate.

We enumerate the various novel features of the current solver for simulating two-phase incompressible flows.

- the flow solver utilizes a direct solver with a semi-implicit scheme for time discretization. This scheme, leading to a linear system, is: easier to handle in combination with the XFEM, accurate, and computationally less expensive;
- the numerical integration in the XFEM is improved by employing a mesh refinement inside the cut elements;
- high gradients in the velocity field are accounted for by smoothing the viscosity in the vicinity of the interface; and
- the mesh refinement approach allows for a more accurate reinitialization procedure.

It is obvious that only a portion of the wide field of two-phase and free-surface flows was treated in this work. In a future work, the further development of the solver framework aims at:

- improving the performance, the need for a higher-order temporal discretization;
- extending to three-dimensional two-phase flows, using the Taylor-Hood element (P2/P1) and an iterative solver for the linear system;
- parallelization, currently, only 2D two-phase flow problems are treated. However, for complex 3D problems, the parallelization can be exploited by parallelizing the entire solver; and
- enlarging the area of possible applications.

BIBLIOGRAPHY

Arnold, D. N., F. Brezzi, et al. (1984). "A stable finite element for the stokes equations." Calcolo 21(4): 337-344.

Atluri, S. N. and S. Shen (2002). The meshless local Petrov-Galerkin (MLPG) method, Crest.

Ausas, R. F., G. C. Buscaglia, et al. (2012). "A new enrichment space for the treatment of discontinuous pressures in multi-fluid flows." International Journal for Numerical Methods in Fluids 70(7): 829-850.

Babuška, I., G. Caloz, et al. (1994). "Special finite element methods for a class of second order elliptic problems with rough coefficients." SIAM J. Numer. Anal. 31(4): 945-981.

Babuška, I. and J. M. Melenk (1997). "The partition of unity method." International Journal for Numerical Methods in Engineering 40(4): 727-758.

Béchet, E., H. Minnebo, et al. (2005). "Improved implementation and robustness study of the X-FEM for stress analysis around cracks." International Journal for Numerical Methods in Engineering 64(8): 1033-1056.

Bell, J. B., P. Colella, et al. (1989). "A second-order projection method for the incompressible navier-stokes equations." Journal of Computational Physics 85(2): 257-283.

Belytschko, T. and T. Black (1999). "Elastic crack growth in finite elements with minimal remeshing." International Journal for Numerical Methods in Engineering 45(5): 601-620.

Belytschko, T., R. Gracie, et al. (2009). "A review of extended/generalized finite element methods for material modeling." Modelling and Simulation in Materials Science and Engineering 17(4): 043001.

Belytschko, T., Y. Y. Lu, et al. (1994). "Element-free Galerkin methods." International Journal for Numerical Methods in Engineering 37(2): 229-256.

Benzley, S. E. (1974). "Representation of singularities with isoparametric finite elements." International Journal for Numerical Methods in Engineering 8(3): 537-545.

Best, J. P. (1993). "The formation of toroidal bubbles upon the collapse of transient cavities." Journal of Fluid Mechanics 251: 79-107.

Bordas, S., P. V. Nguyen, et al. (2007). "An extended finite element library." International Journal for Numerical Methods in Engineering 71(6): 703-732.

Brackbill, J. U., D. B. Kothe, et al. (1992). "A continuum method for modeling surface tension." J. Comput. Phys. 100(2): 335-354.

Brezzi, F. and M. Fortin (1991). Mixed and hybrid finite element methods, Springer-Verlag New York, Inc.

Carlos, A., K. C. Park, et al. (2001). "Partitioned analysis of coupled mechanical systems." Computer Methods in Applied Mechanics and Engineering 190(24–25): 3247-3270.

Cheng, K. W. and T. P. Fries (2012). "XFEM with hanging nodes for two-phase incompressible flow." Computer Methods in Applied Mechanics and Engineering 245–246(0): 290-312.

Chessa, J. and T. Belytschko (2003). "An enriched finite element method and level sets for axisymmetric two-phase flow with surface tension." International Journal for Numerical Methods in Engineering 58(13): 2041-2064.

Chessa, J. and T. Belytschko (2003). "An Extended Finite Element Method for Two-Phase Fluids." Journal of Applied Mechanics 70(1): 10-17.

Chessa, J. and T. Belytschko (2004). "Arbitrary discontinuities in space–time finite elements by level sets and X-FEM." International Journal for Numerical Methods in Engineering 61(15): 2595-2614.

Chessa, J. and T. Belytschko (2006). "A local space–time discontinuous finite element method." Computer Methods in Applied Mechanics and Engineering 195(13–16): 1325-1343.

Chessa, J., P. Smolinski, et al. (2002). "The extended finite element method (XFEM) for solidification problems." International Journal for Numerical Methods in Engineering 53(8): 1959-1977.

Dolbow, J. and T. Belytschko (1999). "Numerical integration of the Galerkin weak form in meshfree methods." Computational Mechanics 23(3): 219-230.

Dolbow, J., N. Moës, et al. (2000). "Discontinuous enrichment in finite elements with a partition of unity method." Finite Elements in Analysis and Design 36(3–4): 235-260.

Enright, D., R. Fedkiw, et al. (2002). "A Hybrid Particle Level Set Method for Improved Interface Capturing." Journal of Computational Physics 183(1): 83-116.

Esser, P., J. Grande, et al. (2010). "An extended finite element method applied to levitated droplet problems." International Journal for Numerical Methods in Engineering 84(7): 757-773.

Fries, T.-P. and T. Belytschko (2010). "The extended/generalized finite element method: An overview of the method and its applications." International Journal for Numerical Methods in Engineering 84(3): 253-304.

Fries, T.-P. and A. Zilian (2009). "On time integration in the XFEM." International Journal for Numerical Methods in Engineering 79(1): 69-93.

Fries, T. P. (2009). "The intrinsic XFEM for two-fluid flows." International Journal for Numerical Methods in Fluids 60(4): 437-471.

Ganesan, S., G. Matthies, et al. (2007). "On spurious velocities in incompressible flow problems with interfaces." Computer Methods in Applied Mechanics and Engineering 196(7): 1193-1202.

Gingold, R. A. and J. J. Monaghan (1977). "Smoothed particle hydrodynamics: theory and application to non-spherical stars." Monthly Notices of the Royal Astronomical Society 181(3): 375-389.

Gravouil, A., N. Moës, et al. (2002). "Non-planar 3D crack growth by the extended finite element and level sets—Part II: Level set update." International Journal for Numerical Methods in Engineering 53(11): 2569-2586.

Greaves, D. M. (2006). "Simulation of viscous water column collapse using adapting hierarchical grids." International Journal for Numerical Methods in Fluids 50(6): 693-711.

Groß, S. and A. Reusken (2007). "An extended pressure finite element space for two-phase incompressible flows with surface tension." Journal of Computational Physics 224(1): 40-58.

Gross, S. and A. Reusken (2011). Numerical Methods for Two-phase Incompressible Flows, Springer.

Henke, F. (2012). An extended finite element method for turbulent premixed combustion Dissertation, Technische Universität München.

Hirt, C. W. and B. D. Nichols (1981). "Volume of fluid (VOF) method for the dynamics of free boundaries." Journal of Computational Physics 39(1): 201-225.

Huerta, A. and W. K. Liu (1988). "Viscous flow with large free surface motion." Computer Methods in Applied Mechanics and Engineering 69(3): 277-324.

Hughes, T. J. R., G. R. Feijóo, et al. (1998). "The variational multiscale method—a paradigm for computational mechanics." Computer Methods in Applied Mechanics and Engineering 166(1–2): 3-24.

Hysing, S., S. Turek, et al. (2009). "Quantitative benchmark computations of two-dimensional bubble dynamics." International Journal for Numerical Methods in Fluids 60(11): 1259-1288.

Karihaloo, B. L. and Q. Z. Xiao (2003). "Modelling of stationary and growing cracks in FE framework without remeshing: a state-of-the-art review." Computers & Structures 81(3): 119-129.

Karypis, G. and V. Kumar (1998). "A Fast and High Quality Multilevel Scheme for Partitioning Irregular Graphs." SIAM J. Sci. Comput. 20(1): 359-392.

Kass, M., A. Witkin, et al. (1988). "Snakes: Active contour models." International Journal of Computer Vision 1(4): 321-331.

Koshizuka, S., H. Tamako, et al. (1995). "A particle method for incompressible viscous flow with fluid fragmentations." Computational Fluid Dynamics Journal 4(1): 29-46.

Legrain, G., N. Moës, et al. (2008). "Stability of incompressible formulations enriched with X-FEM." Computer Methods in Applied Mechanics and Engineering 197(21–24): 1835-1849.

Liao, J.-H. and Z. Zhuang (2012). "A consistent projection-based SUPG/PSPG XFEM for incompressible two-phase flows." Acta Mechanica Sinica 28(5): 1309-1322.

Marchandise, E., P. Geuzaine, et al. (2007). "A stabilized finite element method using a discontinuous level set approach for the computation of bubble dynamics." Journal of Computational Physics 225(1): 949-974.

Martin, J. C. and W. J. Moyce (1952). "Part IV. An Experimental Study of the Collapse of Liquid Columns on a Rigid Horizontal Plane." Philosophical Transactions of the Royal Society of London. Series A, Mathematical and Physical Sciences 244(882): 312-324.

Melenk, J. M. and I. Babuška (1996). "The partition of unity finite element method: Basic theory and applications." Computer Methods in Applied Mechanics and Engineering 139(1–4): 289-314.

Merriman, B., J. K. Bence, et al. (1994). "Motion of Multiple Junctions: A Level Set Approach." Journal of Computational Physics 112(2): 334-363.

Minev, P. D., T. Chen, et al. (2003). "A finite element technique for multifluid incompressible flow using Eulerian grids." Journal of Computational Physics 187(1): 255-273.

Moës, N., M. Cloirec, et al. (2003). "A computational approach to handle complex microstructure geometries." Computer Methods in Applied Mechanics and Engineering 192(28–30): 3163-3177.

Moës, N., J. Dolbow, et al. (1999). "A finite element method for crack growth without remeshing." International Journal for Numerical Methods in Engineering 46(1): 131-150.

Moës, N., A. Gravouil, et al. (2002). "Non-planar 3D crack growth by the extended finite element and level sets—Part I: Mechanical model." International Journal for Numerical Methods in Engineering 53(11): 2549-2568.

Monaghan, J. J. (1994). "Simulating Free Surface Flows with SPH." Journal of Computational Physics 110(2): 399-406.

Norato, J., R. Haber, et al. (2004). "A geometry projection method for shape optimization." International Journal for Numerical Methods in Engineering 60(14): 2289-2312.

Osher, S. and J. A. Sethian (1988). "Fronts propagating with curvature-dependent speed: Algorithms based on Hamilton-Jacobi formulations." Journal of Computational Physics 79(1): 12-49.

Peng, D., B. Merriman, et al. (1999). "A PDE-Based Fast Local Level Set Method." Journal of Computational Physics 155(2): 410-438.

Pilliod Jr, J. E. and E. G. Puckett (2004). "Second-order accurate volume-of-fluid algorithms for tracking material interfaces." Journal of Computational Physics 199(2): 465-502.

Rasthofer, U., F. Henke, et al. (2011). "An extended residual-based variational multiscale method for two-phase flow including surface tension." Computer Methods in Applied Mechanics and Engineering 200(21–22): 1866-1876.

Sauerland, H. (2013). An XFEM based sharp interface approach for two-phase and free-surface flows Ph.D. thesis, Aachen University.

Sauerland, H. and T.-P. Fries (2011). "The extended finite element method for two-phase and free-surface flows: A systematic study." Journal of Computational Physics 230(9): 3369-3390.

Schönheinz, H. (1975). "G. Strang / G. J. Fix, An Analysis of the Finite Element Method. (Series in Automatic Computation. XIV + 306 S. m. Fig. Englewood Clifs, N. J. 1973. Prentice-Hall, Inc." ZAMM - Journal of Applied Mathematics and Mechanics / Zeitschrift für Angewandte Mathematik und Mechanik 55(11): 696-697.

Schott, B., U. Rasthofer, et al. (2015). "A face-oriented stabilized Nitsche-type extended variational multiscale method for incompressible two-phase flow." International Journal for Numerical Methods in Engineering 104(7): 721-748.

Sethian, J. A. (1999). Level Set Methods and Fast Marching Methods. Cambridge, Cambridge University Press.

Shu, C.-W. and S. Osher (1989). "Efficient implementation of essentially non-oscillatory shock-capturing schemes, II." Journal of Computational Physics 83(1): 32-78.

Smolianski, A. (2001). Numerical Modeling of Two-Fluid Interfacial Flows Dissertation, University of Jyväskylä.

Sousa, F. S., R. F. Ausas, et al. (2012). "Numerical assessment of stability of interface discontinuous finite element pressure spaces." Computer Methods in Applied Mechanics and Engineering 245–246(0): 63-74.

Stolarska, M., D. L. Chopp, et al. (2001). "Modelling crack growth by level sets in the extended finite element method." International Journal for Numerical Methods in Engineering 51(8): 943-960.

Strouboulis, T., I. Babuška, et al. (2000). "The design and analysis of the Generalized Finite Element Method." Computer Methods in Applied Mechanics and Engineering 181(1–3): 43-69.

Strouboulis, T., K. Copps, et al. (2001). "The generalized finite element method." Computer Methods in Applied Mechanics and Engineering 190(32–33): 4081-4193.

Sussman, M., E. Fatemi, et al. (1998). "An improved level set method for incompressible two-phase flows." Computers & Fluids 27(5–6): 663-680.

Sussman, M., P. Smereka, et al. (1994). "A Level Set Approach for Computing Solutions to Incompressible Two-Phase Flow." Journal of Computational Physics 114(1): 146-159.

Tezduyar, T. E., M. Behr, et al. (1992). "A new strategy for finite element computations involving moving boundaries and interfaces—The deforming-spatial-domain/space-time procedure: I. The concept and the preliminary numerical tests." Computer Methods in Applied Mechanics and Engineering 94(3): 339-351.

Tezduyar, T. E., M. Behr, et al. (1992). "A new strategy for finite element computations involving moving boundaries and interfaces—The deforming-spatial-domain/space-time procedure: II. Computation of free-surface flows, two-liquid flows, and flows with drifting cylinders." Computer Methods in Applied Mechanics and Engineering 94(3): 353-371.

Ubbink, O. (1997). Numerical prediction of two fluid systems with sharp interfaces Ph.D. thesis, University of London and Imperial College of Science, Technology & Medicine.

Unverdi, S. O. and G. Tryggvason (1992). "A front-tracking method for viscous, incompressible, multi-fluid flows." Journal of Computational Physics 100(1): 25-37.

Verschueren, M., F. N. Van De Vosse, et al. (2001). "Diffuse-interface modelling of thermocapillary flow instabilities in a Hele-Shaw cell." Journal of Fluid Mechanics 434: 153-166.

Wu, J.-Y. and F.-B. Li (2015). "An improved stable XFEM (Is-XFEM) with a novel enrichment function for the computational modeling of cohesive cracks." Computer Methods in Applied Mechanics and Engineering 295: 77-107.

Zahedi, S., M. Kronbichler, et al. (2012). "Spurious currents in finite element based level set methods for two-phase flow." International Journal for Numerical Methods in Fluids 69(9): 1433-1456.

Zahedi, S. and A.-K. Tornberg (2010). "Delta function approximations in level set methods by distance function extension." Journal of Computational Physics 229(6): 2199-2219.

Zlotnik, S. and P. Díez (2009). "Hierarchical X-FEM for n-phase flow." Computer Methods in Applied Mechanics and Engineering 198(30–32): 2329-2338.